STRUCTURE AND KINEMATICS OF THE STELLAR HALOS AND THICK DISKS OF THE MILKY WAY BASED ON CALIBRATION STARS FROM SDSS DR7

Daniela Carollo[1,2], Timothy C. Beers[3], Masashi Chiba[4], John E. Norris[1], Ken C. Freeman[1], Young Sun Lee[3], Zeljko Ivezic[5], Constance M. Rockosi[6], and Brian Yanny[7]

ABSTRACT

The structure and kinematics of the recognized stellar components of the Milky Way are explored, based on well-determined atmospheric parameters and kinematic quantities for 32360 "calibration stars" from the Sloan Digital Sky Survey (SDSS) and its first extension, (SDSS-II), which included the sub-survey SEGUE: Sloan Extension for Galactic Understanding and Exploration. Full space motions for a sub-sample of 16920 stars, exploring a local volume within 4 kpc of the Sun, are used to derive velocity ellipsoids for the inner- and outer-halo components of the Galaxy, as well as for the canonical thick-disk and proposed metal-weak thick-disk populations. This new sample of calibration stars represents an increase of 60% relative to the numbers used in a previous analysis. We first examine the question of whether the data require the presence of at least a two-component halo in order to account for the rotational behavior of likely halo stars in the local volume, and whether more than two components are needed. We also address the question of whether the proposed metal-weak thick disk is kinematically and chemically distinct from the canonical thick disk, and point out that the Galactocentric rotational velocity inferred for the metal-weak thick disk, as well as its mean metallicity, appear quite similar to the values derived previously for the Monoceros stream, suggesting a possible association between these structures. In addition, we consider the fractions of each component required to understand the nature of the observed kinematic behavior of the stellar populations of the Galaxy as a function of distance from the plane. Scale lengths and scale heights for the thick-disk and metal-weak thick-disk components are determined. Spatial density profiles for the inner- and outer-halo populations are inferred from a Jeans Theorem analysis. The full set of calibration stars (including those outside the local volume) is used to test for the expected changes in the observed stellar metallicity distribution function with distance above the Galactic plane *in-situ*, due to the changing contributions from the underlying stellar populations. The above issues are considered, in concert with theoretical and observational constraints from other Milky-Way-like galaxies, in light of modern cold dark matter galaxy formation models.

Subject headings: Galaxy: Evolution, Galaxy: Formation, Galaxy: Halo, Galaxy: Disks, Galaxy: Kinematics, Galaxy: Structure, Methods: Data Analysis, Stars: Abundances, Surveys

1. INTRODUCTION

The Milky Way is a unique laboratory, as it is the one large galaxy where it is possible to analyze the full space motions and chemical compositions of its stellar populations based on individual stars, and to use this information to disentangle its structural properties in great detail. Knowledge of the full six-dimensional location and velocity phase space and the chemical properties of stellar populations in the Galaxy provides invaluable information, not only on its recognized structures (and sub-structures, such as tidal streams), but by extension, on the nature of its formation and evolution. These concepts are well-understood, and have been widely used in previous studies, from the seminal work of Eggen, Lynden-Bell, & Sandage (1962) and Searle & Zinn (1978), to more recent research based on much larger samples of tracer objects (e.g., globular clusters: Zinn 1993; field stars: Hartwick 1987; Sandage & Fouts 1987; Sommer-Larsen & Zhen 1990; Allen, Schuster, & Poveda 1991; Ryan & Norris 1991; Kinman et al. 1994; Norris 1994; Carney et al. 1996; Chiba & Beers 2000; Ivezić et al. 2008; Xue et al. 2008; Morrison et al. 2009), all working toward drawing a much more detailed picture of our host galaxy.

The primary recognized stellar populations in the solar neighborhood are the thin disk (sometimes separated into the old and young thin disks), the thick disk, and the halo; the properties of these components have been reasonably well-determined by numerous previous authors. However, some issues remain unresolved. Examples include the origin of the thick disk, and the lower metallicity limit of its member stars. While many authors argue that the thick disk is likely to have formed in response to ancient accretion events (e.g., Quinn & Goodman (1986), Freeman (1987); Abadi et al. 2003, and references therein), recent suggestions have been made that some properties of the thick disk could be understood as the result of the radial migration of stars within the disk itself (e.g., Schoenrich & Binney 2009). Furthermore, despite numerous efforts, the issue of whether or not the so-called metal-weak thick disk (MWTD; see Chiba & Beers 2000, and references therein) is a distinct structure from the canonical thick disk has yet to be settled. Details concerning the origin of the

[1] Research School of Astronomy and Astrophysics, Australian National University, Cotter Road, Weston, ACT 2611, Australia; carollo@mso.anu.edu.au;jen@mso.anu.edu.au; kcf@mso.anu.edu.au

[2] INAF-Osservatorio Astronomico di Torino, Italy

[3] Department of Physics & Astronomy and JINA: Joint Institute for Nuclear Astrophysics, Michigan State University, E. Lansing, MI 48824, USA; beers@pa.msu.edu;lee@pa.msu.edu

[4] Astronomical Institute, Tohoku University, Sendai 980-8578, Japan; chiba@astr.tohoku.ac.jp

[5] Department of Astronomy, University of Washington, Box 351580, Seattle, WA 98195, USA; ivezic@astro.washington.edu

[6] Astronomy and Astrophysics Department, University of California, Santa Cruz, CA 95064, USA; crockosi@ucolick.org

[7] Fermi National Accelerator Laboratory, P.O. Box 500, Batavia, IL 60510, USA; yanny@fnal.gov

Galactic halo are of particular interest for understanding the formation and evolution of our Galaxy. Indeed, the halo contains most of the metal-poor stars of the Milky Way, objects that encode the nature of the first stars to form in the Universe, which can be used to constrain models of large galaxy formation and evolution in general.

The Galactic halo has long been considered a single component. However, evidence has accumulated over the past few decades that it may be more complex (Carney 1984; Hartwick (1987); Allen et al. 1991; Preston, Shectman, & Beers 1991; Majewski 1992; Zinn 1993; Kinman et al. 1994; Norris 1994; Carney et al. 1996; Chiba & Beers 2000; Kinman et al. 2007; Lee, Gim, & Casetti-Dinescu 2007; Miceli et al. 2008). Recently, based on an analysis of a large sample of calibration stars from the Sloan Digital Sky Survey (SDSS) DR5 (Adelman-McCarthy et al. 2007), Carollo et al. (2007) argued for the existence of *at least* a two-component halo. In their view the Galactic halo comprises two broadly overlapping structural components, an inner and an outer halo. These components exhibit different spatial density profiles, stellar orbits, and stellar metallicities. It was found that the inner-halo component dominates the population of halo stars found at distances up to 10-15 kpc from the Galactic center, while the outer-halo component dominates in the region beyond 15-20 kpc. The inner halo was shown to comprise a population of stars exhibiting a flattened spatial density distribution, with an inferred axial ratio on the order of ~ 0.6. According to Carollo et al. (2007), inner-halo stars possess generally high orbital eccentricities, and exhibit a small (or zero) net prograde rotation around the center of the Galaxy. The metallicity distribution function (MDF) of the inner halo peaks at [Fe/H] = -1.6, with tails exending to higher and lower metallicities. By comparison, the outer halo comprises stars that exhibit a more spherical spatial density distribution, with an axial ratio ~ 0.9. Outer-halo stars possess a wide range of orbital eccentricities, exhibit a clear retrograde net rotation, and are drawn from an MDF that peaks at [Fe/H] = -2.2, a factor of four lower than that of the inner-halo population.

In this paper we present further details on the structural and kinematic parameters for the inner and outer halos, as well as for the thick disk and MWTD, based on analysis of a large sample of calibration stars from SDSS DR7 (Abazajian et al. 2009). The DR7 sample includes stars obtained during the Sloan Extension for Galactic Understanding and Exploration (SEGUE; see Yanny et al. 2009), one of three sub-surveys obtained during the first extension of SDSS, known as SDSS-II.

This paper is outlined as follows. For the convenience of the reader the basic assumptions of our analytic approach and our main results are briefly summarized in §2. Section 3 describes the calibration stars from SDSS DR7, the methodology used to derive their stellar atmospheric parameter estimates (T_{eff}, log g, [Fe/H]), and the criteria used to identify a local sample for our kinematic analysis. The techniques used to derive estimates of the kinematic and orbital parameters for stars in our sample are described in §4. This section also provides a comparison of the changes in the sampling of the spatial distribution and in the derived local kinematic properties for the calibration-star samples due to the expansion from DR5 to DR7. Section 5 considers the optimal variables for extracting knowledge of the primary stellar-population components revealed in the solar neighborhood, and addresses the question of whether a dual-halo population is in fact required to understand the observed local kinematics of the halo. This section also describes the general properties of the maximum likelihood technique we employ, and its application for decoupling the thick-disk, inner-, and outer-halo components. In this section we also evaluate the fractions of each component as a function of distance from the Galactic plane inferred from the present data, consider whether the MWTD might be an independent component from the thick disk, and derive the rotational lag and dispersion of the MWTD, as well as the range of metallicities covered by the MWTD. Derived velocity ellipsoids for the thick-disk, MWTD, and the halo components are reported in §6. In §7 the scale length and scale height of the thick disk are derived; the MWTD scale length is also constrained. Section 8 derives the inferred spatial density profiles for the two halo components, based on a Jeans Equation analysis. In §9 we consider the observed tilts of the velocity ellipsoids as a function of vertical distance and metallicity. The *in-situ* "as-observed" MDF, based on cuts in distance from the Galactic plane for the full sample of calibration stars, is described in §10. Section 11 presents a summary and discussion of our results.

2. BASIC ASSUMPTIONS AND BRIEF SYNOPSIS OF MAIN RESULTS

In order to carry out our analysis we make the central assumption that the Galaxy comprises a number of principal stellar components that are well-described by Gaussian kinematic distribution functions and individual metallicity distribution functions of (for now) unknown shape. We then model these components using Maximum Likelihood techniques, and compare these models with the observed properties of the SDSS DR7 calibration stars. We make the additional assumption that the number of stellar components should be taken as the minimum necessary to adequately describe the observations, and no additional components are added to the models if they do not result in statistically significant improvements in the ability of our models to fit the data.

With the above set of assumptions, we find: (a) A single-population halo is incompatible with the observed kinematics of local stars with [Fe/H] < -2.0, while a dual (inner/outer) halo model is necessary to describe the observations. (b) The net rotation of the outer halo is slightly more retrograde than previously reported, $\langle V_\phi \rangle = -80 \pm 13$ km s^{-1}. (c) The net rotation of the inner halo is consistent with zero (at the two-sigma level), $\langle V_\phi \rangle = 7 \pm 4$ km s^{-1}. (d) There exists a gradient in the mean rotational velocity of likely inner-halo stars, $\triangle \langle V_\phi \rangle / \triangle |Z| = -28 \pm 9$ km s^{-1} kpc^{-1}, for stars located within 2 kpc of the Galactic plane. (e) The dispersions in the rotational-velocity component for both the inner- and outer-halo populations increase with distance from the plane. This may apply to the MWTD as well. (f) The net rotation of the canonical thick-disk population, for stars close to the plane, is $\langle V_\phi \rangle = 182 \pm 2$ km s^{-1}. (g) The asymmetric drift of the thick disk varies with distance from the plane, as shown by previous work, $\triangle \langle V_\phi \rangle / \triangle |Z| = -36 \pm 1$ km s^{-1} kpc^{-1}. (h) The thick-disk and MWTD systems only contribute to our sample within 5 kpc of the plane, the inner-halo population dominates between 5 and 10 kpc, and the outer-halo population dominates beyond 20 kpc. The inversion point in the dominance of the inner/outer halo is located in the distance range 15-20 kpc. (i) A MWTD, kinematically independent of the canonical thick disk (with net rotation $\langle V_\phi \rangle = 100$-150 km s^{-1}), is required to account for the rotational properties of low-metallicity stars close to the Galactic plane. (j) The metal-

licity range for stars that are likely members of the MWTD is $-1.8 \lesssim$ [Fe/H] $\lesssim -0.8$, possibly up to [Fe/H] ~ -0.7. (k) The derived velocity ellipsoids, (σ_{V_R}, σ_{V_ϕ}, σ_{V_Z}), for the four components we have considered are as follows – Thick Disk $= (53 \pm 2, 51 \pm 1, 35 \pm 1)$ km s^{-1}, MWTD $= (59 \pm 3, 40 \pm 3, 44 \pm 3)$ km s^{-1}, Inner Halo $= (150 \pm 2, 95 \pm 2, 85 \pm 1)$ km s^{-1}, Outer Halo $= (159 \pm 4, 165 \pm 9, 116 \pm 3)$ km s^{-1}. (l) The kinematically derived scale length and scale height for the thick disk are $h_R = 2.20 \pm 0.35$ kpc and $h_Z = 0.51 \pm 0.04$ kpc, respectively. The radial scale length for the MWTD is on the order of $h_R \sim 2$ kpc, while the scale height is 1.36 ± 0.13 kpc. (m) The slopes of the inferred power-law spatial-density profiles for the inner- and outer-halo populations are -3.17 ± 0.20 and -1.79 ± 0.29, respectively. (n) The tilt angle, α, between the long axis of the Schwarzschild velocity ellipsoid and the sun-center line is, in Galactocentric cylindrical coordinates, for stars of relatively high metallicity ($-0.8 <$ [Fe/H] < -0.6), $\alpha = 7°.1 \pm 1°.5$ for $1 < |Z| < 2$ kpc, and $\alpha = 5°.2 \pm 1°.2$ for $2 < |Z| < 4$ kpc, consistent with one another. For stars of intermediate metallicity ($-1.5 <$ [Fe/H] < -0.8), the tilt is $\alpha = 10°.3 \pm 0°.4$ close to the plane, and $\alpha = 15°.1 \pm 0°.3$ farther from the plane, which differ significantly from one another. For stars of lower metallicity ([Fe/H] < -1.5), the tilt is $\alpha = 8°.6 \pm 0°.5$ close to the plane, and $\alpha = 13°.1 \pm 0°.4$ farther from the plane, again significantly different. (o) The "as observed" metallicity distribution function of stars in our sample exhibits clear changes with distance from the Galactic plane, exhibiting the anticipated shift from dominance by thick-disk and MWTD populations, with peaks at [Fe/H] $= -0.6$ and -1.3, respectively, to dominance by the inner-halo ([Fe/H] $= -1.6$) and outer-halo ([Fe/H] $= -2.2$) populations.

3. THE SDSS CALIBRATION-STAR SAMPLE

3.1. *SDSS and SEGUE Data*

SDSS-I was an imaging and spectroscopic survey that began routine operations in April 2000, and continued through June 2005. The SDSS and its extensions used a dedicated 2.5m telescope (Gunn et al. 2006) located at the Apache Point Observatory in New Mexico. The telescope is equipped with an imaging camera and a pair of spectrographs, each of which are capable of simultaneously collecting 320 medium-resolution ($R \sim 2000$) spectra over its seven square degree field of view, so that on the order of 600 individual target spectra and roughly 40 calibration-star and sky spectra are obtained on a given spectroscopic "plug-plate" (York et al. 2000).

The SEGUE sub-survey, carried out as part of SDSS-II, ran from July 2005 to July 2008. SEGUE obtained some 240000 medium-resolution spectra of stars in the Galaxy, selected to explore the nature of stellar populations from 0.5 kpc to 100 kpc (Yanny et al. 2009). In the present paper we make use of the spectroscopy and photometry obtained by SDSS/SEGUE for the small number (16) of calibration stars obtained for each spectroscopic plug-plate, chosen for two primary reasons. The first set of these objects, the spectrophotometric calibration stars, are stars that are selected to approximately remove the distortions of the observed flux of stars and galaxies arising from the wavelength response of the Astrophysical Research Consortium (ARC) 2.5m telescope and the SDSS spectrographs, as well as the distortions imposed on the observed spectra by the Earth's atmosphere. The spectrophotometric calibration stars cover the apparent magnitude range $15.5 < g_0 < 17.0$, and satisfy the color ranges $0.6 < (u-g)_0 <$

1.2 ; $0.0 < (g-r)_0 < 0.6$.[8] The second set of stars, the telluric calibration stars, is used to calibrate and remove night-sky emission and absorption features from SDSS spectra. The telluric calibration stars cover the same color ranges as the spectrophotometric calibration stars, but at fainter apparent magnitudes, in the range $17.0 < g_0 < 18.5$.

The SEGUE Stellar Parameter Pipeline (SSPP) processes the wavelength- and flux-calibrated spectra generated by the standard SDSS spectroscopic reduction pipeline, obtains equivalent widths and/or line indices for about 80 atomic or molecular absorption lines, and estimates the effective temperature, T_{eff}, surface gravity, log g, and metallicity, [Fe/H], for a given star through the application of a number of approaches. A given method is usually optimal over specific ranges of color and signal-to-noise (S/N) ratio. The SSPP employs 8 primary methods for the estimation of T_{eff}, 10 for the estimation of log g, and 12 for the estimation of [Fe/H]. The final estimates of the atmospheric parameters are obtained by robust averages of the methods that are expected to perform well for the color and S/N of the spectrum obtained for each star. The use of multiple methods allows for empirical determinations of the internal errors for each parameter, based on the range of reported values from each method – typical internal errors for stars in the temperature range that applies to the calibration stars are $\sigma_{Teff} \sim 100$ K to ~ 125 K, $\sigma_{logg} \sim 0.25$ dex, and $\sigma_{[Fe/H]} \sim 0.20$ dex. The external errors in these determinations are of similar size. See Lee et al. (2008a,b) and Allende Prieto et al. (2008) for more details.

Over the past several years, large-aperture telescopes have been used to obtain high-resolution spectroscopy for over 300 of the brighter ($14.0 < g_0 < 17.0$) SDSS stars (see Allende Prieto et al. 2008; W. Aoki et al., in preparation; D. Lai et al., in preparation). W. Aoki et al. (in preparation) and D. Lai et al. (in preparation) suggest that the current SSPP is actually somewhat conservative in the assignment of metallicities for stars of the lowest [Fe/H], in the sense that high-resolution estimates of [Fe/H] are on the order of 0.2-0.3 dex lower than those reported by the SSPP. For the purpose of our present analysis, we have used these preliminary results to apply a quadratic correction to the SSPP-derived metallicities, of the form:

$$[\mathrm{Fe/H}]_C = -0.186 + 0.765 * [\mathrm{Fe/H}]_A - 0.068 * [\mathrm{Fe/H}]_A{}^2 \quad (1)$$

where [Fe/H]$_A$ is the adopted metallicity from the SSPP, and [Fe/H]$_C$ is the corrected metallicity. This polynomial has little effect on stars with metallicity greater than about [Fe/H] $= -2.5$, but lowers the estimated metallicities for stars below this abundance by 0.1 to 0.2 dex.

Once estimates of the atmospheric parameters for each of the calibration stars are obtained, one can use the derived surface gravity of each star to infer whether it is a likely dwarf, main-sequence turnoff star, subgiant, or giant. Photometric estimates of the distance to each star (accurate to an estimated 10%-20%) are then obtained by comparison of its observed apparent magnitude (corrected for interstellar absorption) with its expected absolute magnitude based on calibrated open-cluster and globular-cluster sequences, using the techniques described by Beers et al. (2000). See the discussion

---

[8] The subscript 0 in the magnitudes and colors indicates that they are corrected for the effects of interstellar absorption and reddening, following standard procedures, based on the dust map of Schlegel, Finkbeiner, & Davis (1998).

by Ivezić et al. (2008) for a comparison between the Beers et al. (2000) distances with those obtained by use of cluster fiducials in the native SDSS *ugriz* system.

Radial velocities for stars in our sample are derived from matches to an external library of high-resolution spectral templates with accurately known velocities, degraded in resolution to match the SDSS spectra (see Yanny et al. 2009). The typical precision of the resulting radial velocities is on the order of 5-20 km s^{-1} (depending on the S/N of the spectra), based on multiple repeat observations of individual objects with different plug-plates. Zero-point errors are negligible (after correction for a global offset of 7.3 km s^{-1} of unknown origin), and exhibit a dispersion of no more than 2 km s^{-1}, based on a comparison of the subset of stars in our sample with radial velocities obtained from the high-resolution spectra taken for testing and validation of the SSPP (Allende Prieto et al. 2008; Yanny et al 2009).

The full sample considered in the present paper consists of 32360 unique stars with acceptable derived atmospheric parameters. This represents a 60% increase with respect to the starting sample of 20236 calibration stars considered by Carollo et al. (2007). Although there is clearly a bias towards the identification of metal-poor stars arising from the color selections (in particular for the spectrophotometric calibration stars), it should be kept in mind that it is not possible to discriminate the lowest metallicity stars (e.g., those with [Fe/H] < −2.5) from those with [Fe/H] ∼ −2.0, since the effect of declining metallicity on broadband stellar colors is minimal in this regime (see Ivezić et al. 2008). Hence, we expect that the distribution of metallicities for the calibration stars should reflect the true shape of the low-metallicity tail of the MDF for stars outside the disk populations. The same does not apply for stars with [Fe/H] > −2.0; the observed distributions of metallicity mis-represents the true MDFs at these abundances. It is important to note that no selection on the kinematics, e.g., by making use of measured proper motions, is made in the choice of the calibration objects. This enables our kinematic studies to be carried out without the need to apply explicit corrections or modeling of any selection bias for the motions of the stars in the sample.

3.2. *Selection of Local Sample of Stars*

We begin with a total sample of 32360 unique calibration stars with available spectroscopy and average $S/N \geq 10/1$ over the spectral range 3800 Å to 8000 Å. We then consider all stars with effective temperatures in the range 4500 K $\leq$ T$_{eff}$ $\leq$ 7000 K, over which the SSPP is expected to provide the highest accuracy for the derived atmospheric parameters. This reduces the sample to 32329 stars. In addition to this restriction, stars in our primary sample for kinematic analysis must satisfy the following criteria:

- Stars must have derived distances d < 4 kpc from the Sun, in order to restrict the kinematic and orbital analyses to a local volume (where the assumptions going into their calculation are best satisfied). This selection also mitigates against the increase in the errors in the derived transverse velocities, which scale with distance from the Sun (e.g., for a typical star in our sample, at d = 1 kpc, errors of 3.5 mas/yr in proper motions and 15% in distance result in errors in the derived transverse velocities of 22 km s^{-1}; these rise to 37 km s^{-1} and 46 km s^{-1} for stars at d = 2 kpc and 4 kpc, respectively). This cut reduces the numbers of stars to 24824.

- Stars must have a measured radial velocity, accurate to better than 20 km s^{-1} (which eliminates only a handful of stars from consideration), as well as an "acceptable" proper motion available (which means that the star satisfies additional criteria designed to eliminate spurious reported motions; see Munn et al. 2004). Note that all proper motions have been corrected for the systematic error described by Munn et al. (2008). [9] After these cuts are applied, the total numbers of stars remaining is 23643.

- Stars must have a present Galactocentric distance, projected onto the plane, in the range 7 < R < 10 kpc. This restriction also serves to improve the applicability of the simple models for the adopted form of the Galactic potential we apply during the kinematic analysis. This cut reduces the numbers of stars in our local sample to 16920.

Figure 1 compares the (projected) spatial distributions of the SDSS/SEGUE calibration stars used by Carollo et al. (2007), based on DR5 (Adelman-McCarthy et al. 2007), with that of our present analysis, based on DR7 (Abazajian et al. 2009). In addition to the overall increase in the numbers of stars, one can also notice the impact of the SEGUE fields, which included substantial numbers of stars at lower Galactic latitudes. The upper panel of Figure 2 shows the "as-observed" MDF for the DR7 calibration stars in the full sample (black histogram), as well as for stars selected for the local sample, as described above. The MDFs of the two samples are clearly very similar, and comprise stars with metallicities that sample all of the primary stellar components of the Galaxy. The lower panel of Figure 2 shows the distribution of derived surface gravity, log g, versus effective temperature, T$_{eff}$, obtained by the SSPP. Stars in the full sample are indicated by black dots, while those in the local sample are represented by red dots. Note that the full sample contains substantial numbers of objects with gravities consistent with main-sequence turnoff stars, subgiants, and giants, while the local sample primarily comprises main-sequence turnoff stars and dwarfs. We emphasize that both of the panels in Figure 2 are influenced by the selection functions used for targeting of the calibration stars, and should not be taken as representative of the distribution of either [Fe/H] or log g in the explored volume.

4. DERIVATION OF FULL SPACE MOTIONS AND ORBITAL PARAMETERS

Proper motions, used in combination with distance estimates and radial velocities, provide the information required to calculate the full space motions (the components of which are referred to as U,V,W) of our program stars with respect to the Local Standard of Rest (LSR; defined as a frame in which the mean space motions of the stars in the solar neighborhood average to zero) [10]. Corrections for the motion of the Sun with respect to the LSR are applied during the course of the calculation of the full space motions; here we adopt the values

---

[9] We call attention to the extensive testing of the SDSS-recalibrated proper-motion errors carried out by Bond et al. (2009). By comparison with the derived (non-)motions of distant quasars, they demonstrated that systematic errors on proper motions are no more than 1 milli-arcsecond per year (with an rms of 0.6 milli-arcseconds per year).

[10] The velocity component U is taken to be positive in the direction toward the Galactic anticenter, the V component is positive in the direction of Galactic rotation, and the W component is positive toward the North Galactic Pole.

(U,V,W) = (−9,12,7) km s^{-1} (Mihalas & Binney 1981). For the purpose of analysis it is also convenient to obtain the rotational component of a star's motion about the Galactic center in a cylindrical frame; this is denoted as V_ϕ, and is calculated assuming that the LSR is on a circular orbit with a value of 220 km s^{-1} (Kerr & Lynden-Bell 1986). It is worth noting that our assumed values of R$_\odot$ (8.5 kpc) and the circular velocity of the LSR are both consistent with two recent independent determinations of these quantities by Ghez et al. (2008) and Koposov, Rix, & Hogg (2009).

The orbital parameters of the stars, such as the perigalactic distance (the closest approach of an orbit to the Galactic center), r$_{peri}$, and the apogalactic distance (the farthest extent of an orbit from the Galactic center), r$_{apo}$, of each stellar orbit, the orbital eccentricity, e, defined as $e = (r_{apo} − r_{peri})/(r_{apo} + r_{peri})$, as well as Z$_{max}$ (the maximum distance of a stellar orbit above or below the Galactic plane), are derived by adopting an analytic Stäckel-type gravitational potential (which consists of a flattened, oblate disk, and a nearly spherical massive dark-matter halo; see the description given by Chiba & Beers 2000, Appendix A) and integrating their orbital paths based on the starting point obtained from the observations.

We have considered the possible systematic uncertainty in Z$_{max}$ when one adopts a different gravitational potential, such as the model originally constructed by Dejonghe & de Zeeuw (1988), and later elaborated upon by Batsleer & Dejonghe (1994) and Chiba & Beers (2001), which takes a Kuzmin-Kutuzov potential for both a highly flattened disk and a nearly spherical halo. Experiments with our data indicate that, with the adoption of this alternative potential, the systematic change in this orbital parameter is on the order of 10% for Z$_{max} < 50$ kpc. A larger systematic applies when Z$_{max} > 50$ kpc, where this parameter is more sensitive to the potential. However, the range of Z$_{max}$ explored in this paper is always below 50 kpc, even though a handful of stars have larger values. Errors on the derived orbital parameters due to the observational errors have been estimated through a Monte Carlo simulation (100 realizations for each star). Although the sizes of these errors depend on sample selection, for the Stäckel potential used in Chiba & Beers (2000), together with constraints Z$_{max} < 50$ kpc and R$_{apo} < 50$ kpc (apogalactic distance projected onto the Galactic plane), the estimated one-sigma errors are $\sigma_{r_{peri}} = 1.1$ kpc, $\sigma_{r_{apo}} = 2.2$ kpc, $\sigma_{ecc} = 0.12$, and $\sigma_{Z_{max}} = 1.3$ kpc. The errors in these parameters show little dependence on Z$_{max}$ over the range we consider in this analysis.

Figure 3 shows the derived U,V,W velocity components, as a function of metallicity, for both the DR5 and DR7 calibration-star samples. A comparison of the eccentricity versus [Fe/H] diagrams from DR5 and DR7 is shown in Figure 4. As can be appreciated from inspection of these figures, the increased sample of stars in DR7, as well as refinements in the estimates of metallicities made recently in the SSPP, have better delineated stars in the three primary stellar populations represented in the local volume – the thin disk, the thick disk, and the halo. It should be kept in mind that the numbers of stars shown in Figures 3 and 4 *do not reflect the actual relative proportions* of these populations in our sample volume, due to the selection criteria used and the bright limit of $g \sim 14.5$ imposed by the SDSS imaging.

Figure 5 shows the distribution of derived orbital eccentricities for stars covering different regions of metallicity, chosen to isolate the contributions of the various stellar components

we describe in more detail below, for two different intervals on distance |Z| from the Galactic plane. In the upper panels, for stars with $−1.0 < $ [Fe/H] $ < −0.6$, the dominance of the canonical thick disk is clear in both distance intervals. In the second row of panels, for stars in the metallicity region $−1.5 < $ [Fe/H] $ < −1.0$, the feature extending to $e \sim 0.5$ indicates the likely presence of a MWTD population close to the Galactic plane. Farther from the Galactic plane the observed distribution of eccentricity appears more consistent with inner-halo stars, with some residual contribution from the MWTD. The eccentricity distribution for the metal-poor halo stars with $−2.0 < $ [Fe/H] $ < −1.5$, shown in the third row of panels, is close to the linear distribution $f(e) \propto e$ for both intervals on distance from the plane. This form of $f(e)$ is expected for a well-mixed steady-state system of test particles for which the distribution function is a function of the energy only, moving in the potential of a strongly centrally concentrated density distribution (see Binney & Tremaine, 2008, p. 387). We see below, however, that the distribution function for the metal-poor halo stars cannot simply depend on energy only, because the three components of their velocity dispersion are significantly different. In the lower row of panels, for stars with [Fe/H] $ < −2.0$, the distribution of orbital eccentricies appears strikingly different than in the third row of panels. As discussed below, we expect that this distribution reflects the contribution from an outer-halo population with a less prominent fraction of stars on highly eccentric orbits, superposed on the inner-halo population that dominates the third row of panels.

5. EXTRACTING THE MAJOR STELLAR-POPULATION COMPONENTS IN THE SOLAR NEIGHBORHOOD

5.1. *Basic Parameters*

Carollo et al. (2007) explored how to combine the derived kinematic parameters and metallicity estimates for the calibration stars in DR5 to reveal the presence of the primary stellar populations of the Galactic halo. With the much larger sample of calibration stars available from SDSS/SEGUE DR7, we now refine our investigation in order to disentangle the main components in the solar neighborhood and extract their spatial and kinematic parameters. Although the Galactic disk system comprises both a thin disk and a thick disk (and likely MWTD), the thin disk is not well-represented in our present sample due to the color and apparent magnitude selection criteria used for the SDSS calibration stars. Thus, the main populations we expect to contribute to our sample of local stars are the thick disk (and possibly a MWTD), as well as the inner and outer halos.

Given the strong overlap in the spatial and metallicity distributions of the components we consider, it is necessary to define a suitable set of parameters to best identify the presence of each population. Based on our tests of alternatives, the best parameters for this purpose are the distance from the Galactic plane, the rotational velocity of a star in a cylindrical frame with respect to the Galactic center, and the stellar metallicity. As shown in Figure 1, the local sample within 4 kpc of the Sun well-covers the region where the thick-disk (and MWTD) components are expected to be prominently represented. Thus, for exploration of these components we employ |Z|, the present distance of a star above or below the Galactic plane. In contrast, for exploration of the halo components we use Z$_{max}$, which depends on the adopted gravitational potential, as an indicator of their vertical extension, The choice of Z$_{max}$ for the Galactic halo is necessary because of the much

larger spatial extent of its two primary components, relative to that of the thick-disk components. Below we consider possible correlations of Z_{max} with other kinematic or spatial parameters used in this analysis.

Velocity ellipsoids are evaluated in a Galactocentric cylindrical reference frame, (R,ϕ,Z), where R is the distance of the star from the Galactic center, projected onto the Galactic plane. The angular coordinate ϕ is taken to be positive in the direction of Galactic rotation, and Z is the height above or below the Galactic plane. In this system, the mean velocities and their dispersions are denoted by $(\langle V_R \rangle, \sigma_{V_R})$, $(\langle V_\phi \rangle, \sigma_{V_\phi})$, and $(\langle V_Z \rangle, \sigma_{V_Z})$. It is also explicity assumed, for the present analysis, that the velocity ellipsoids of the disk and halo systems are aligned on the coordinate axes. We explicitly test this assumption in §9 below.

The first step is to understand the *global behavior* of the derived kinematic parameters as a function of metallicity and $|Z|$ or Z_{max}. Figure 6 shows the derived velocity distributions for V_R, V_ϕ, and V_Z for different metallicity ranges. As expected, the rotational velocity exhibits rather different behavior as the range in [Fe/H] changes. In the two upper panels of this figure the thick disk is dominant ($V_\phi \sim 200$ km s^{-1}), while in the lower panels, as metallicity decreases, the halo becomes more clearly present ($V_\phi \sim 0$ km s^{-1}). The long tail of the rotational velocity distribution towards retrograde velocities seen in the lower panels arises from stars that likely belong to the outer-halo population. In contrast to this behavior, the distributions of V_R and V_Z remain almost symmetric over all ranges of metallicity, and the mean velocities are always close to zero, as expected. Notice that the dispersions of V_R and V_Z increase as [Fe/H] decreases, reflecting the dominance of the halo components at lower metallicity. This figure suggests that, among these parameters, V_ϕ most clearly distinguishes the influence of the different stellar populations in the Galaxy represented in our local sample.

It is important to check for possible correlations that might exist between Z_{max} and (V_R, V_ϕ, V_Z) before their use in the kinematic analysis of the inner- and outer-halo populations. Figure 7 shows the cylindrical velocity components, as a function of Z_{max}, for the stars in our local sample. The upper panel indicates a correlation between V_R and Z_{max}, in particular for extreme values of V_R. An even stronger correlation is seen in the lower panel of the figure, which represents the vertical velocity component, V_Z. These correlations arise because large values of V_R and V_Z correspond to large orbital energy in the meridional plane, (R,Z), and thus also to large values of Z_{max}. By contrast, the rotational velocity V_ϕ (middle panel) does not exhibit a strong correlation with Z_{max}, other than that expected from the presence of the thick-disk population at high positive rotation velocity and the halo at lower rotational velocity. Note, in the middle panel, the clear excess of stars with retrograde motions for $Z_{max} > 15$ kpc, which we associate with the outer-halo component, as discussed below. We conclude that the Galactocentric rotational velocity, V_ϕ, and the vertical distance, Z_{max} (or $|Z|$), when combined with metallicity, can be used to obtain useful information on the different stellar populations present in the local volume.

5.2. *How Many Components in the Stellar Halo?*

If the halo of the Galaxy is spatially and kinematically complex, as argued by Carollo et al. (2007) and other previous authors, a natural question that arises is just how many components must be invoked to accommodate the available data.

Note that here we are considering the definition of a "component" to mean a *bona-fide* stellar population, in the traditional sense, which is to say that the member stars share a common set of locations, kinematics, compositions (MDFs), and possibly ages (or distributions of ages), indicative of a likely common astrophysical origin. This definition would not extend to include the presence of *individual* substructures, such as debris streams (e.g., Yanny et al. 2003; Belokurov et al. 2006; Grillmair 2006; Bell et al. 2008; Grillmair et al. 2008; Klement et al. 2009; Schlaufman et al. 2009), and other overdensities such as the Virgo Overdensity (An et al. 2009, and references therein). Rather, our analysis seeks to model the kinematics of the halo using a minimum number of components, which themselves may or may not comprise the superposition of numerous individual substructures. The distinction is irrelevant for our approach.

Our most powerful tool for distinguishing various halo components is consideration of the rotational behavior of likely halo stars. A sub-sample of the local calibration stars, satisfying rather strict limits on metallicity, [Fe/H] < -2.0, and orbital distances above the plane, $Z_{max} > 5$ kpc, should be dominated by the halo components, with little or no thick-disk or MWTD contamination. We now consider such a sample for addressing this issue.

The question of how many components may comprise a complex halo can be subtle, since in principle individual components should be free to take on wide ranges of mean rotational velocity and dispersion, and it may or may not be possible to reliably separate them if there exists too large an overlap in their kinematic behaviors. Simple subjective guesses for the likely input parameters needed to carry out mixture-model analyses are not suitable for obtaining statistically sound answers to the question of the need (or not) for multiple components. Fortunately, alternatives exist. Kauffman & Rousseeuw (1990) describe the use of a clustering algorithm "Partitioning Around Medoids" (PAM), and its large-N extension "Clustering LARge Applications" (CLARA). These algorithms seek clusters of objects that have a high degree of similarity, while maximizing the degree of dissimilarity between different clusters. The original data set is initially partitioned into clusters around k so-called "representative objects," referred to as the medoids, then an iterative scheme is applied to locate the medoids that best achieve the similarity/dissimilarity goal. The algorithm employed by PAM/CLARA is similar to the well-known *k-means* clustering algorithm, but it is more robust to outliers, and enjoys the computational advantage that it obtains a unique partitioning of the data without the need for explicit multiple starting points for the proposed clusters.

The quality of the resulting partitions selected by PAM/CLARA can be assessed by inspection of the dimensionless parameter $s(i)$, which takes on values in the range $-1 \leq s(i) \leq +1$. This parameter measures the similarity of a given datum i to its closest represesentative object, relative to its next nearest representative object. If $s(i)$ is close to +1, we can reasonably conclude that the datum is properly assigned. If not, and $s(i)$ takes on values closer to 0 or -1, we can conclude that either it is not clear to which representative object the datum should be assigned ($s(i) \sim 0$) or that it has been misassigned ($s(i) \sim -1$). Once a successful partition of the data has been made, we can inspect the following summary values: (1) $\bar{s}(i)$, the average of $s(i)$ within a given cluster, and (2) $\bar{s}(k)$, the average of $s(i)$ for the entire data set. This last number provides some guidance on what value of k is most

TABLE 1
CLUSTER ANALYSIS RESULTS: PARTITIONING AROUND MEDOIDS

k	Objects	Coordinate (km s^{-1})	IQR (km s^{-1})	$\bar{s}(i)$	$\bar{s}(k)$	$\langle V_\phi \rangle$ (km s^{-1})	σ_{V_ϕ} (km s^{-1})	Fraction	p-value
(1)	(2)	(3)	(4)	(5)	(6)	(7)	(8)	(9)	(10)
1	710	−31	178	⋯	⋯	−71	142	1.00	0.002
2	363	60	40	0.65	0.61	−18	99	0.51	0.350
	347	−142	142	0.57	⋯	−128	159	0.49	⋯
3	310	−23	74	0.66	0.53	−55	94	0.66	0.321
	230	−175	132	0.50	⋯	−277	104	0.17	⋯
	170	135	77	0.43	⋯	75	95	0.17	⋯

NOTE. — The interquartile range (IQR) is a measure of the scale (dispersion) of the data. In the case of a normal distribution the IQR is related to the dispersion by σ = IQR/1.349

appropriate for a given data batch, i.e., the number of clusters is chosen such that $\bar{s}(k)$ is a maximum[11].

Table 1 summarizes the results of the partitioning exercise (using CLARA) for different input numbers of clusters, $1 \leq k \leq 3$. Column (1) lists the numbers of clusters. Column (2) lists the numbers of stars assigned to each cluster. Column (3) lists the coordinate (V_ϕ) for the representative object nearest the center of each proposed cluster. The inter-quartile range (IQR; see definition in Table 1) in V_ϕ covered by the proposed cluster is listed in column (4). The summary statistics $\bar{s}(i)$ and $\bar{s}(k)$ are listed in columns (5) and (6), respectively. Note that the results are ordered in Table 1 from high to low numbers of the proposed objects in each cluster.

As seen in Table 1, the first (non-trivial) split suggested by CLARA ($k = 2$) results in essentially equally populated clusters with positive (60 km s^{-1}) and negative (−142 km s^{-1}) coordinates, albeit with rather different IQRs. Each of the two clusters has moderately high values of $\bar{s}(i)$, and the average over both clusters, $\bar{s}(k)$, indicates a significant split. As one progresses to the case $k = 3$, CLARA splits the negative coordinate cluster into two pieces (at coordinates −23 km s^{-1} and −175 km s^{-1}), and moves the positive cluster to higher velocity (135 km s^{-1}). Note that the significance for two of the individual splits drops to below $\bar{s}(i) = 0.60$, as does the average $\bar{s}(k)$. This provides an indication that there is likely to be no need for three or more components in order to fit a reasonable mixture model to these data.

The partitions suggested by CLARA can be used to guide choices of input parameters for mixture-modeling of the proposed clusters. The R statistical software package (http://www.r-project.org/), and in particular its associated package R-Mix (http://www.math.mcmaster.ca/peter/mix/mix.html) provide convenient tools for simple analyses of mixtures.

Here we take the coordinates of the proposed medoids as input starting points for $\langle V_\phi \rangle$, and σ_{V_ϕ} = IQR/1.349 as estimates of the input starting points for the dispersions of the (assumed Gaussian) individual components. R-Mix quickly converges, and provides the final estimates of the means, dispersions, and fractions listed in columns (7)-(9) of Table 1, respectively. The final column of Table 1 lists the so-called p-value, which represents the probability of obtaining a value

of reduced χ^2 for the fit as large (or larger) by chance. The results of the fits are shown in Figure 8. It is clear, even from casual inspection, that the case of a single cluster ($k = 1$) is a poor description of the data. This impression is confirmed from the p-value of the chi-square statistic for this fit (0.002), which strongly rejects the null hypothesis of a single cluster.

As can be seen, the $k = 2$ component fit appears much improved, and indeed the p-value cannot reject the null hypothesis that two components are sufficient to describe these data. The p-value for the $k = 3$ case is also unable to reject the null hypotheses, but we emphasize that the quality of the initial partitions from CLARA strongly suggest that $k = 2$ is an appropriate choice for the number of components. A likelihood ratio test, which compares the statistical improvement of the fit obtained from $k = 3$ components over that with $k = 2$ components, indicates only minimal improvement is obtained from the four additional degrees of freedom (the two additional means and dispersions, and the two additional mixture fractions). In other words, the value of the maximum likelihood is not increased sufficiently to justify the need for an additional component in the fit. The conclusion of this exercise is that, while larger numbers of halo components beyond two can be *accommodated* by the available kinematical information, they are not *required*, nor do they provide superior fits to the data.

5.3. *The Maximum Likelihood Technique*

For more flexibility in our further analyses of mixture models, and to specify the kinematic parameters of the various components in the local volume, it is convenient to implement a maximum likelihood approach. This has been carried out, making use of the routine AMOEBA (Press et al. 1992) for performing searches for the maximum in the likelihood function, as described below.

Maximum Likelihood (ML) analysis is a well-known general method for statistical estimation. The basic theory of this technique assumes that the data can be described by a probability density function, $f(X; \alpha)$, where X is a variable, and α represents the parameter (or vector of parameters) characterizing the known form of f. The aim of the method is then to estimate α. If X_1, $X_1...X_n$ are the individual data, and assuming that they are independent and drawn from f, then the likelihood function can be written as:

$$L(X_1, X_2, ..., X_n) = f(X_1, X_2, ..., X_n | \alpha)$$

[11] The partitioning experiment described here only considers individual velocity components that have larger dispersions than could be accounted for by expected errors in the derived rotation velocities.

$$= f(X_1|\alpha) f(X_2|\alpha)...f(X_n|\alpha)$$
$$= \prod_{1 \le i \le n} f(X_i|\alpha) \qquad (2)$$

In its classical form, this equation gives the likelihood of obtaining the data, given α (Wall & Jenkins 2003).

The basic parameters we consider in this analysis, V_ϕ and Z_{max}, are used to define a likelihood function such that all the main structural components in the solar neighborhood (with the exception of the thin disk, which contains very few stars in our sample) are included in α.

It has been argued that the thick-disk component may include stars with substantially lower abundance than its peak value (around [Fe/H] = −0.6). Several authors have claimed a low-metallicity tail for the thick disk (the MWTD) extending to stars as metal deficient as [Fe/H] ∼ −1.6, or even lower (Norris, Bessell, & Pickles 1985; Morrison, Flynn, & Freeman 1990; Beers & Sommer-Larson 1995; Layden 1995; Martin & Morrison 1998; Chiba, Yoshii, & Beers 1999; Katz et al. 1999; Chiba & Beers 2000; Beers et al. 2002). The question of the limiting abundance of the MWTD has been considered several times in the past (Rodgers & Roberts 1993; Layden 1995; Beers & Sommer-Larsen 1995; Ryan & Lambert 1995; Twarog & Anthony-Twarog 1996; Chiba & Beers 2000), and in more recent work as well (Reddy & Lambert 2008). In particular, Chiba & Beers (2000) claimed that the MWTD contributes about 30% of the metal-poor stars in the abundance range −1.7 <[Fe/H]≤ −1.0 in the solar neighborhood. Note that, in the majority of these efforts, the kinematics of the MWTD were assumed to be similar (or identical) to those of the canonical thick disk. The small samples of stars available previously for investigation of this question limited the available options.

Ivezić et al. (2008) adopted a different approach, modeling the observed photometric metallicities and rotational velocities of main-sequence turnoff stars from SDSS DR6 (Adelman-McCarthy et al. 2008) as a function of distance from the Galactic plane, for a narrow cone at the North Galactic Pole. The marginal distributions of metallicity and rotation velocities for these data were fit *independent of one another* to non-Gaussian functions for the disk (and single Gaussians in metallicity and rotation velocity for the halo), from which an adequate description of the global behavior of the disk+halo was obtained. We remind the reader that in our approach we seek to model the observed properties of the stars in our local sample by assuming that stars are associated with identifiable individual stellar populations, with differing kinematics and metallicity distributions, that comprise the disk and halo populations.

In the present paper we explore the possibility that the thick-disk system may comprise two separate stellar populations, with independent kinematics, that we associate with the canonical thick-disk and MWTD components. The Galactic halo is assumed to be a two-component structure, comprising the inner and outer halos, as discussed by Carollo et al. (2007). Thus, the general expression for the likelihood function takes the form:

$$\log f = \sum_{i=1}^{n} \log[F_{td} \cdot f_{td}^i + F_{mwtd} \cdot f_{mwtd}^i + F_{in} \cdot f_{in}^i + F_{out} \cdot f_{out}^i] (3)$$

where F_{td}, F_{mwtd}, F_{in}, and F_{out} are the stellar fractions of the thick disk, MWTD, inner halo, and outer halo, respectively.

On the left side of Eqn. 3, the function f depends on the mean velocity, dispersion, and stellar fraction of each component. On the right side of the equation, the functions f^i denote the (Gaussian) velocity distributions adopted to represent each component.

Thus, the likelihood function has twelve output parameters that must be determined (the fractions, and the mean rotation velocities and dispersions of each component). However, the problem can be greatly simplified by working in different ranges of metallicity, combined with different values of Z_{max} (or |Z|), where one component is dominant with respect to the others, and then fitting the distribution of the rotational velocity in each range of metallicity separately. Adopting this approach, we first consider the extremes of the MDF for the local sample ([Fe/H] < −2.0 for the metal-poor sub-sample, and −0.8 < [Fe/H] < −0.6 for the metal-rich sub-sample). The first range is completely dominated by the two overlapping halo components, the inner and outer halo; we expect that many of the stars in this sub-sample belong to the outer halo, which has a peak in its MDF at [Fe/H] ≃ −2.2 (Carollo et al. 2007). The second range contains stars belonging primarily to the thick-disk population, whose MDF has a peak at [Fe/H] = −0.6. The ML analysis proceeds by specifying several input parameters *a-priori*, then holding them fixed during subsequent analysis (e.g., by derivation of the global behavior of V_ϕ at the extremes of the metallicity ranges). A similar approach was adopted by Chiba & Beers (2000) and other previous work.

In §5.4 we first derive the trends of $\langle V_\phi \rangle$ and σ_{V_ϕ} for the low-metallicity sub-sample (the thick disk and MWTD are assumed to not be present in this region of [Fe/H]) as a function of Z_{max}. This analysis fixes the values of the mean rotational velocity and dispersion for the outer-halo population by consideration of the extrema of these trends. Once these values are specified, ML fits are obtained for the mean rotation and dispersion of the inner-halo population.

In §5.5 we examine the trends of $\langle V_\phi \rangle$ and σ_{V_ϕ} for the high-metallicity sub-sample, as a function of |Z|, to derive the mean rotation velocity and dispersion for the thick-disk population. We also derive the gradient in the rotation velocity for the thick disk as a function of |Z|. The ML analysis is then extended to include the full range of metallicity for the local sample, in order to derive the values of the stellar fractions (F_{td}, F_{in}, F_{out}) as a function of Z_{max}.

In §5.6 we consider stars in the intermediate-metallicity sub-sample (−2.0 < [Fe/H] < −0.6), split into three distinct metallicity intervals, to assess the requirement for a MWTD as an independent component. We then employ a mixture-model analysis to test for the presence of a MWTD component in each of these intervals as a function of |Z|. Finally, we explore the metallicity range of the MWTD component.

5.4. *Extracting the Inner/Outer Halo Components in the Low-Metallicity Range*

5.4.1. *Characteristic Properties of the Outer-Halo Component*

Here we examine the properties of the mean Galactocentric rotational velocity, $\langle V_\phi \rangle$, and its dispersion, σ_{V_ϕ}, as a function of the vertical distance, Z_{max}, for stars in the local sample falling into the low-metallicity range ([Fe/H] < −2.0). At high Z_{max} this sample is expected to be dominated by halo stars with large retrograde motions, suggesting membership in the outer-halo population.

Figure 9 shows the result of this exercise. Here, the values

of $\langle V_\phi \rangle$ and σ_{V_ϕ} are evaluated by passing a box of 100 stars, with an overlap of 70 stars per bin, through the data. The blue curves represent the sub-sample of stars in the range of metallicity $-1.5 < [Fe/H] < -1.2$, shown for comparison purposes, while the red curves indicate stars in the low-metallicity sub-sample. In the upper panel, for $Z_{max} < 5$ kpc, the rotational velocities of the intermediate-metallicity stars exhibit a strong gradient, declining from a value of ~ 100 km s^{-1} down to an average velocity of ~ 0 km s^{-1}. This behavior is likely due to the overlap of two stellar populations, the MWTD and the inner halo, which dominates the sample starting from $Z_{max} \sim 5$ kpc. Above this value of Z_{max} the average rotational velocity is ~ 0 km s^{-1}, or slightly prograde, over the range 5 kpc $< Z_{max} < 15$ kpc, then trends toward retrograde values as Z_{max} increases.

The low-metallicity sub-sample exhibits an abrupt change of $\langle V_\phi \rangle$ in the range of Z_{max} between 5 and 10 kpc, which indicates a transition between the inner- and outer-halo populations. The $\langle V_\phi \rangle$ for this sub-sample then slowly trends to a constant value $\langle V_\phi \rangle \sim -100$ km s^{-1} at large Z_{max}, after undergoing a few oscillations that are likely due to correlations between contiguous overlapping bins.

For comparison with previous work we have also considered the rotational behavior of the low-metallicity sub-sample, as a function of $|Z|$, up to $|Z| = 2$ kpc. In this metallicity range we expect that most of the stars are associated with the inner-halo component, with little contamination from the MWTD (which we show below ceases contributing significant numbers of stars below $[Fe/H] \sim -1.8$) or from outer-halo stars due to the proximity to the disk plane. We confirm the existence of a gradient in the mean rotational velocity over this range of $\triangle\langle V_\phi \rangle / \triangle |Z| = -28 \pm 9$ km s^{-1} kpc^{-1}, as also reported in Chiba & Beers (2000) (see discussion in §11.1).

The lower panel of Figure 9 shows the dispersion of the Galactocentric rotational velocity, as a function of Z_{max}, for the two sub-samples. Note that the velocity dispersions discussed here still include the effects of observational errors, and are thus somewhat higher than their "true" values. Below we make use of the "as observed" dispersions for the low-metallicity sub-sample for ML modeling of the observed distribution of V_ϕ.[12]

The velocity dispersion exhibits a mean value around 100 km s^{-1} for $Z_{max} < 5$ kpc for both sub-samples (slightly lower for intermediate-metallicity stars, and slightly higher for low-metallicity stars). At larger values of Z_{max} the dispersion increases for both sub-samples, with intermediate-metallicity stars trending to $\sigma_{V_\phi} \sim 125$ km s^{-1}, and low-metallicity stars trending to $\sigma_{V_\phi} \sim 190$ km s^{-1} for $Z_{max} > 20$ kpc.

Figure 9 clearly indicates that above Z_{max} between 10 and 20 kpc, the low-metallicity sub-sample is dominated by a highly retrograde halo component with a large dispersion (outer halo), while the slightly prograde and lower dispersion component (inner halo) is dominant for $Z_{max} < 10$ kpc. For the purpose of the ML analysis described in the following subsection the input values of the mean rotational velocity and dispersion for the outer-halo component are evaluated

by choosing stars from the low-metallicity sub-sample with $Z_{max} > 15$ kpc (where contamination from the inner-halo population should be minimal). For the outer-halo component this analysis leads to a value for $\langle V_\phi \rangle = -80 \pm 13$ km s^{-1}, slightly more retrograde than that obtained by Carollo et al. (2007) (~ -70 km s^{-1}) from the DR5 sample of local calibration stars. For the dispersion we obtain $\sigma_{V_\phi} = 180 \pm 9$ km s^{-1} (uncorrected for observational errors).

5.4.2. *Maximum Likelihood Results*

We adopt a likelihood function for V_ϕ for the low-metallicity sub-sample, based on a mixture of two Gaussian distributions representing the two halo components, with a normalization forcing their sum to unity ($F_{in} + F_{out} = 1$). The input parameters for the likelihood function are the values of $\langle V_\phi \rangle$ and σ_{V_ϕ} for the outer halo, as obtained in the previous section; the output parameters are the mean rotational velocity and its dispersion for the inner halo and the stellar fractions for the inner- and outer-halo components. The fit is then performed selecting different intervals of the vertical distance, Z_{max}.

As a first application, we have performed a fit for the low-metallicity sub-sample of stars, selected with 1 kpc $< Z_{max} < 10$ kpc, and $Z_{max} > 10$ kpc, respectively.[13] While a contribution from a MWTD population may still be present, the lower limit of Z_{max} for the sub-sample close to the Galactic plane has been chosen to reduce its possible impact.

Figure 10 shows the result of this exercise. The histograms in each panel are the distribution of the observed V_ϕ in the two selected ranges of Z_{max}, while the green (inner halo) and red (outer halo) curves represent the results of the ML analysis for these two components; the blue curves are the mixture models obtained by their sum. Visual inspection suggests that the fits well-represent the observed distribution of the data for both cuts on Z_{max}. It is clear that the inner-halo component dominates the sub-sample of stars at 1 kpc $< Z_{max} < 10$ kpc, while the net-retrograde, high-dispersion outer-halo population dominates for $Z_{max} > 10$ kpc.

Prior experience suggests that visual inspection of multiple-component fits are often insufficient for interpreting results of mixture-model analyses. Thus, we have also evaluated the so-called Double Root Residuals (DRRs) for these fits. The DRR plot is a variation of a hanging histogram, which is just a (non-normalized) difference plot between binned data and a proposed fitting function. One limitation of the hanging histogram is that it gives equal weight to residuals from bins near the extrema of a distribution (which are usually poorly populated) as to residuals near the middle of a distribution (which are usually well-populated, and hence subject to greater $\sqrt{N}/N$ variations). A square-root transformation applied to the residuals provides a desirable variance stabilization. The DRR plot is a refinement to the canonical root-residual plot (Velleman & Hoaglin 1981), which avoids some difficulties with small data sets. The set of DRRs is obtained using:

$$DRR = \sqrt{2 + 4(N_{obs})} - \sqrt{1 + 4(N_{fit})} \quad \text{if } N_{obs} \geq 1 \quad (4)$$

$$= 1 - \sqrt{1 + 4(N_{fit})} \quad\quad\quad \text{if } N_{obs} = 0 \quad (5)$$

---

[12] Below we correct, as appropriate, derived velocity dispersions for the effects of measurement errors following the formalism of Jones & Walker (1988). In order to remove the effects of observational errors, the term $\frac{1}{n}\sum_{i=1}^{n}\xi_i^2$, where ξ_i is the error on measurement, is subtracted from the observed dispersion.

[13] It should be noted that this sample differs from that used in §5.2 above, which was employed to assess the appropriate number of halo components.

In the above, N_{obs} and N_{fit} are the number of observed and predicted stars in each bin, respectively.

There are several advantages of a DRR plot over a simple difference plot for illustrating the residuals. First, it graphically emphasizes *where* in a distribution lack of fit between data and model exists – the square-root transformation puts the residuals throughout the fit on an equal footing. Secondly, if the model is close to an adequate fit to the data, then the DRRs are roughly equivalent to normal deviates. Thus, a DRR with numerical value $> \pm 2$ is significant at the 95% (2σ) level, whereas DRRs less than this value indicate a reasonable agreement between data and model in a given bin. As can be appreciated from inspection of the right-hand panels in Figure 10, the DRRs for the inner/outer halo fits obtained from the ML analysis are acceptable for most bins, with the exception of bins near the high positive and high negative velocity regions for the 1 kpc $< Z_{max} <$ 10 kpc cut. Indeed, the p-value of the reduced χ^2 for this cut strongly rejects the null hypothesis of a good fit ($p = 0.0003$).This suggests that complexity beyond the simple description of an inner-halo population we have adopted may remain to be explored.

By contrast, the DRRs for the $Z_{max} > 10$ kpc cut, and the p-value of the reduced χ^2 for the global fit ($p = 0.950$), both indicate that the proposed fit is acceptable. In this first application the utility of the DRRs becomes clear. Visual inspection of the fit shown in the upper-left panel of Figure 10 might have suggested that the proposed mixture model was adequate (although the chi-square analysis rejected this hypothesis), while the DRRs clearly revealed the location in the distribution where the lack of fit was most obvious. In addition, the possible deviations from the proposed model fit in the lower-left panel of Figure 10 might have suggested lack of fit, but the DRRs indicated that the deviations are in fact not significant (as confirmed by the chi-square analysis). It is quite difficult for the eye to separate out the effects of root-N variations from real deviations for populations of different sizes. Indeed, it is the smaller size of the population for the fit in the lower-left panel, as well as the smaller individual bin populations, which account for the fact that the proposed model cannot be rejected, while it *is* rejected for the larger population shown in the upper-left panel.

To evaluate the mean rotational velocity, its dispersion, and the fractions of stars for the inner-halo components, a second set of Z_{max} cuts was examined. In this case we fit sub-samples of stars selected with different upper limits on Z_{max} (cumulative Z_{max}), and keeping the lower limit set at 1 kpc. The complete set of the derived inner-halo parameters and their 1 σ errors are summarized in Table 2.

Estimates of the errors on the output parameters were obtained following a well-known procedure, based on the assumption that the maximum of the likelihood, L_{max}, is the best estimator for the parameters of the model, and that the logarithm of the likelihood ratio, $-2\ln(\frac{L'}{L_{max}})$, is asymptotically distributed like the χ^2 distribution (e.g., Lupton 1993).

5.5. *Extracting the Thick-Disk Component and the Fractions of Each Galactic Component*

5.5.1. *Characteristic Properties of the Thick-Disk Component*

To extract information on the canonical thick-disk component we select a sub-sample of stars in the metallicity range $-0.8 <$ [Fe/H] < -0.6, and derive its mean rotational velocity and dispersion as a function of vertical distance, $|Z|$, up to 4 kpc from the Galactic plane. It should be kept in mind

TABLE 2
MAXIMUM LIKELIHOOD RESULTS FOR THE
LOW-METALLICITY SUB-SAMPLE – INNER
HALO PARAMETERS

Z_{max} (kpc)	$\langle V_{\phi,in} \rangle$ (km s^{-1})	$\sigma_{V_{\phi,in}}$ (km s^{-1})	F_{in}
1–5	11 ± 4	113 ± 3	1.00 ± 0.01
1–10	7 ± 4	110 ± 3	0.93 ± 0.01
1–15	10 ± 4	106 ± 3	0.83 ± 0.02
1–20	13 ± 4	105 ± 4	0.78 ± 0.02
1–25	20 ± 4	100 ± 3	0.70 ± 0.02
1–30	23 ± 4	97 ± 3	0.66 ± 0.02

NOTE. — The input parameters for the outer halo have been fixed at ($\langle V_{\phi,out} \rangle$, $\sigma_{V_{\phi,out}}$) = (−80, 180) km s^{-1}. The listed dispersions are not corrected for observational errors. The normalization $F_{in} + F_{out} = 1$ is assumed.

that there may remain some contamination from MWTD stars even in this high-metallicity range, which might have an influence on the observed behavior.

Figure 11 shows the result of this exercise. As seen in the upper panel of this figure, for $|Z| < 1$ kpc, the mean rotational velocity is ~ 200 km s^{-1}; as has been previously noted by several authors, it decreases at larger heights above the plane. A least-squares fit to the data yields $\triangle \langle V_\phi \rangle / \triangle |Z| = -36 \pm 1$ km s^{-1} kpc^{-1}. Inspection of the lower panel of Figure 11 shows that, for $|Z| > 2$ kpc, σ_{V_ϕ} increases from the canonical value of around 40-50 km s^{-1} to on the order of 90 km s^{-1}. In the same panel we note the presence of some oscillations that are larger than the errors on the dispersion for each bin of $|Z|$. We suspect that this jagged structure of σ_{V_ϕ} could be due to the presence of substructures, which will be investigated in a future paper. The fiducial parameters we adopt for the thick disk are obtained by selecting the sample at $1 < |Z| < 2$ kpc, in the high-metallicity range mentioned above. This selection is intended to avoid contamination by thin-disk stars (including those with possibly mis-estimated metallicities).

We obtain a mean velocity and dispersion of $\langle V_\phi \rangle = 182 \pm 2$ km s^{-1} and $\sigma_{V_\phi} = 57 \pm 1$ km s^{-1} (uncorrected for the observational errors, which are typically on the order of 5-6 km s^{-1} for large sub-samples, and 10-15 km s^{-1} for smaller sub-samples, respectively).

5.5.2. *Maximum Likelihood Results*

We now evaluate the stellar fractions of the thick-disk, inner-halo, and outer-halo components with the ML analysis, as a function of Z_{max}, including stars over the full metallicity range of our local sample. The analysis was performed by selecting sub-samples of stars located in *strips* of Z_{max} (differential Z_{max}). Recall that previously, for the low-metallicity sub-sample, cuts were selected for different values of the upper limit on Z_{max} (cumulative Z_{max}). The differential distribution is better able to respond to changes in the dominance of the overlapping structures, and thus is suitable for examination of the trend of the stellar fractions as a function of Z_{max}.

The mean rotational velocities and dispersions for each component are fixed to the values obtained above (dispersions uncorrected for the observational errors): ($\langle V_{\phi,td} \rangle$, $\sigma_{V_{\phi,td}}$) = (182, 57) km s^{-1}; ($\langle V_{\phi,in} \rangle$, $\sigma_{V_{\phi,in}}$) = (7, 110) km s^{-1}; ($\langle V_{\phi,out} \rangle$, $\sigma_{V_{\phi,out}}$) = (−80, 180) km s^{-1}. Note that for the inner-halo pa-

rameters we have adopted the values listed in Table 2 for $1 < Z_{max} < 10$ kpc. Values for these three components are taken as input parameters for the ML analysis, while the output parameters are the stellar fractions, F_{td}, F_{in}, and F_{out}, respectively. Note that it is not strictly necessary that we fix the input parameters of the various components; we do this in order to obtain robust estimates of their fractions, which would change if the inputs were allowed to vary.

The likelihood function comprises three components, $F_{td}f_{td}$, $F_{in}f_{in}$ and $F_{out}f_{out}$; as before, the fs are assumed to be Gaussian distributions representing the corresponding V_ϕ components. The likelihood function is normalized to $F_{td} + F_{in} + F_{out} = 1$. The results of the analysis are shown in Figure 12. It is clear from inspection of the left-hand panels of Figure 12 that, for $Z_{max} < 5$ kpc, only two components contribute significantly – the thick disk and the inner halo. At $5 < Z_{max} < 10$ kpc, only the inner-halo component contributes (the green line representing this component exactly overlays the blue mixture-model line). At $10 < Z_{max} < 15$ kpc the outer halo begins to contribute, although the inner halo is still dominant. At $15 < Z_{max} < 20$ kpc, the inner halo and outer halo make comparable contributions. Finally, when $Z_{max} > 20$ kpc, the outer-halo component is completely dominant, with very little contribution from the inner-halo component.

The right-hand panels of Figure 12 are the DRRs of the corresponding fits. The individual bin residuals for the subsets of the data above 15 kpc are consistent with adequate fits (as are the p-values of their reduced χ^2 determined for the global fits), but those for the cuts below 15 kpc exhibit significant deviations that may be of interest. We consider these in turn.

We originally assumed that the extreme negative residual seen for $Z_{max} < 5$ kpc at highly prograde V_ϕ arose primarily from the absence of a thin-disk component in our model. However, additional experiments were performed over the distance range $1 < Z_{max} < 5$ kpc, to explicitly avoid substantial thin-disk contamination; the lack of fit remained.

We also considered a possible difference in the thick-disk fiducial parameters when evaluated using Z_{max} instead of $|Z|$. The estimated values obtained in the range $1 < Z_{max} < 2$ kpc are $\langle V_\phi \rangle = 190 \pm 2$ km s^{-1} and $\sigma_{V_\phi} = 46 \pm 1$ km s^{-1} (not corrected for observational errors). When the ML analysis is performed with these thick-disk parameters, the lack of fit is slightly reduced, but the residuals in the velocity range $0 \lesssim V_\phi \lesssim 150$ km s^{-1} increase. In this velocity range the lack of fit may indicate the presence of a MWTD component. To explore this possibility, a further experiment has been performed, adding a fourth component in the model to fit the sub-sample of stars in the upper panel of Figure 12, using the R-Mix modeling approach. We find that a four-component model provides a better fit (p-value = 0.11) .[14]

With no restrictions on metallicity, there is considerable latitude allowed for the kinematic parameters derived for each component. This is, unfortunately, rather difficult to overcome on the basis of the simple mixture-model analysis we have employed. More detailed modeling, taking metallicity into account, is described below.

This experiment shows that, close to the Galactic plane, the structure of the Galaxy is complex, and a fourth component is required to obtain a better fit. However, for the purpose

[14] With derived velocity dispersions $\sigma_{V_{\phi,I}} = 97 \pm 4$ km s^{-1}, $\sigma_{V_{\phi,II}} = 59 \pm 19$ km s^{-1}, $\sigma_{V_{\phi,III}} = 37 \pm 19$ km s^{-1}, and $\sigma_{V_{\phi,IV}} = 31 \pm 8$ km s^{-1}, and fractions for each component of $F_I = 0.26$, $F_{II} = 0.20$, $F_{III} = 0.30$ and $F_{IV} = 0.24$, respectively.

TABLE 3
STELLAR FRACTIONS FOR THE THICK DISK, INNER HALO, AND OUTER HALO

Z_{max} (kpc)	F_{td}	F_{in}	F_{out}
< 5	0.55 ± 0.03	0.45 ± 0.02	0.00 ± 0.02
5–10	0.00 ± 0.03	1.00 ± 0.02	0.00 ± 0.02
10–15	0.00 ± 0.04	0.80 ± 0.03	0.20 ± 0.02
15–20	0.00 ± 0.05	0.55 ± 0.04	0.45 ± 0.03
> 20	0.00 ± 0.02	0.08 ± 0.01	0.92 ± 0.02

NOTE. — The input parameters for all three components have been fixed at the following values: $(\langle V_{\phi,td} \rangle, \sigma_{V_{\phi,in}}) = (182, 57)$ km s^{-1}; $(\langle V_{\phi,in} \rangle, \sigma_{V_{\phi,in}}) = (7, 110)$ km s^{-1}; $(\langle V_{\phi,out} \rangle, \sigma_{V_{\phi,out}}) = (-80, 180)$ km s^{-1}, respectively. The normalization $F_{td} + F_{in} + F_{out} = 1$ is assumed.

of obtaining the stellar fractions of the inner- and outer-halo components as a function of the vertical distance Z_{max}, which is our primary objective in this section, we have chosen to employ the simpler three-component model, even though the fit is not optimal over all distance cuts. Issues related to the MWTD are discussed in the following sections.

Figure 13 shows the derived fractions of the three components in our basic model, the canonical thick disk, the inner halo, and the outer halo, as a function of Z_{max}, as derived from the ML analysis. The thick disk is denoted by a black dot, and is only present, as expected, in the first bin of vertical distance ($0 < Z_{max} < 5$ kpc). In this range the fraction of the thick-disk and inner-halo (green dots) components are roughly equal. Above $Z_{max} = 5$ kpc, only the inner-halo and outer-halo (red dots) components are present. The inner-halo stellar fraction decreases with increasing Z_{max}, while the outer-halo stellar fraction increases. The *inversion point* in the dominance of the inner/outer halo occurs in the range of Z_{max} between 15 and 20 kpc.

Table 3 reports the values of the stellar fractions for the three components, and their errors, evaluated as before.

5.6. *How Many Components in the Stellar Disk ?*

We now consider the nature of the disk populations, and in particular explore the question of whether an independent MWTD must be present in order to account for the rotational properties of the stars in our local sample close to the Galactic plane. The approach used here is similar to that employed for modeling of the Galactic halo components. We seek to model the kinematics of the thick-disk system using a minimum number of components, assuming as before that the presence (or not) of individual substructures in each component is not relevant for our approach. We also assume that Schwarzschild velocity ellipsoids apply, and that the ellipsoids are aligned to the cylindrical coordinate system we employ.

In an initial set of experiments, we used the ML method to explore stars in an intermediate-metallicity range ($-2.0 <$ [Fe/H] < -0.6) over different intervals in vertical distance from the plane, $|Z|$, but the results were inconclusive. The overlaps in the rotational behavior of the various components present over such a wide metallicity range made it difficult to isolate the kinematic properties of the individual components. Instead, we hope to simplify the problem by dividing our local sample of stars into three primary metallicity

regions, which are intended to include as few populations as possible. These regions are (*i*) $-2.0 <$ [Fe/H] < -1.5, (*ii*) $-1.5 <$ [Fe/H] < -1.0, and (*iii*) $-1.0 <$ [Fe/H] < -0.6. For the purpose of this discussion, we consider the contribution from a given component to be significant if its fraction, as assigned by the mixture-modeling analysis, is $> 10\%$.

We proceed by carrying out objective initial partitions for each metallicity region in two sets of intervals on distance from the plane, $1 < |Z| < 2$ kpc, and $2 < |Z| < 4$ kpc. The lower limit of the first interval is set to 1 kpc to avoid contamination from stars of the thin-disk population, which, although they might not be expected to be present at metallicities [Fe/H] < -0.6, may have had their metallicities slightly mis-estimated by the current SSPP, and entered the sample unintentionally. As previously, we used CLARA to obtain splits of the V_ϕ parameter for cases of $k = 1$, $k = 2$, and $k = 3$ clusters. The initial estimates for $\langle V_\phi \rangle$, and its dispersion, σ_{V_ϕ}, were then used as inputs for the R-Mix routine, which produced final estimates of the best-fit mixture models for each metallicity region and distance interval. Note that for this set of experiments all parameters are allowed to be "free"; we do not hold any of their properties fixed during the modeling procedure.

The results of the above experiment are listed in Table 4 and shown in Figures 14 and 15. Table 4 is divided into two sections corresponding to the intervals on vertical distance; within each section the results for the one-, two-, and three-cluster splits are considered separately. Column (1) of this table lists the metallicity region while column (2) lists the numbers of stars in the cut. Columns (3)-(5) list the resulting $\langle V_\phi \rangle$, its dispersion, σ_{V_ϕ}, and the fractions obtained from the R-Mix analysis for component I, respectively. Columns (6)-(8) list the same quantities, where applicable, for component II. Columns (9)-(11) list the same quantities, where applicable, for component III. The final column lists the p-value for the chi-square of the residuals to the listed fit.

5.6.1. *Close to the Galactic Plane (1 < |Z| < 2 kpc)*

We first consider the behavior for the distance interval close to the Galactic plane.

The p-values for the one-cluster and two-cluster splits clearly indicate that there is no metallicity region over which acceptable mixture models exist. Acceptable fits are only obtained for the three-cluster splits, as indicated by the listed p-values. This is also reflected in the appearance of the components shown in Figure 14, and their associated DRRs. Note that in the case of metallicity region *iii* (the higher metallicity range shown in the lower panel of Figure 14), the DRRs do suggest some lack of fit in the region near 220 km s^{-1}, which might suggest contamination from thin-disk stars. However, recall that our distance interval was set to avoid such a contamination. We return to this point below.

Examination of the mean rotational velocities and dispersions for each of the metallicity regions for the three-cluster split is informative. Notice that for metallicity region *i* (the lowest metallicity considered), the three components are all considered significant (fractions $> 10\%$) contributors, and that their means and dispersions might be plausibly assigned to (I) the outer halo, (II) the inner halo, and (III) the MWTD. There is no component with the properties of the canonical thick disk present in this metallicity region, as expected. Inspection of the upper panel of Figure 14 is also revealing. The "flat-topped" (more properly, platykurtic) appearance of the distribution of V_ϕ seen here is a classic signature of a mixture

of populations. Furthermore, the long tail in V_ϕ extending to large negative velocities requires an additional component in order to obtain an acceptable fit.

For metallicity region *ii* (intermediate-metallicity stars), there are only two significant contributors, components II and III. Examination of their means and dispersions suggest their identification with the inner-halo and MWTD components, respectively. The appearance of the middle panel of Figure 14 supports this interpretation as well. Note that the dominance of components II and III is so great that one might have expected that a two-cluster split would have been acceptable. However, some contamination from likely outer-halo stars at high negative velocities pushes the formal chi-square analysis into the region where the two-cluster hypothesis can be rejected. The derived means and dispersions of the dominant components in either the two-cluster or three-cluster splits are similar, in any case. The component we identify with the inner halo accounts for roughly 60% of the stars, while that identified with the MWTD accounts for roughly 40% of the stars in this metallicity region.

For metallicity region *iii* (the highest metallicity considered), all three components are significant contributors. Inspection of the means and dispersions suggests identification of the individual components with (I) the inner halo, (II) the MWTD, and (III) the canonical thick disk. It is of interest that the component we identify with the MWTD is the dominant contributor in this metallicity region, accounting for roughly 60% of the stars, while the component we identify with the inner halo only contributes 15%, the remaining 25% of the stars being accounted for by the canonical thick disk.

The possible lack of fit at high rotation velocities revealed by the DRRs is not likely to be simply the resulthe 1 kpc from the Galactic plane. As shown below, this component appears even more strongly present farther from the plane.

For all three metallicity regions we conclude that an independent MWTD component, with $\langle V_\phi \rangle$ in the range 100-150 km s^{-1}, and σ_{V_ϕ} in the range 40-50 km s^{-1} ($\sim$ 35-45 km s^{-1}, when corrected for observational errors), is required in order to account for the rotational behavior of the stars in our local sample located relatively close to the Galactic plane.

5.6.2. *Additional Splits of the Nearby Sample on |Z| and R*

At the suggestion of the referee, we have carried out additional checks on the nature of the stellar populations close to the disk plane, and on the robustness of our results. We first split the local sample of stars with $1 < |Z| < 2$ kpc into two pieces: sub-sample A corresponding to stars above the Galactic plane ($1 < Z < 2$ kpc), and sub-sample B corresponding to stars below the plane ($-2 < Z < -1$ kpc). The CLARA analysis with one-, two-, and three-cluster splits, for all three metallicity regions, was carried out within each sub-sample, followed by an R-mix mixture-model analysis using the starting points derived from CLARA. It is worth noting that, due to the much higher sampling frequency of SDSS for stars in the North Galactic Hemispere, the total numbers of stars in each of these splits was typically 80% in sub-sample A, and 20% in sub-sample B.

The results of this exercise are as follows. For sub-sample A (the 5749 stars above the plane), in all metallicity regions, one- and two-cluster splits were strongly rejected (as before), while three-cluster splits produced acceptable fits. As found for the full-sample analysis, the intermediate-metallicity component in the three-cluster split provided evidence for only two significant contributors that we identify as the inner halo

TABLE 4
R-Mix Results for Multiple-Component Fits to the Local Sample

[Fe/H]	N_{Stars}	$\langle V_{\phi,I}\rangle$ (km s^{-1})	$\sigma_{V_{\phi,I}}$ (km s^{-1})	F_I	$\langle V_{\phi,II}\rangle$ (km s^{-1})	$\sigma_{V_{\phi,II}}$ (km s^{-1})	F_{II}	$\langle V_{\phi,III}\rangle$ (km s^{-1})	$\sigma_{V_{\phi,III}}$ (km s^{-1})	F_{III}	p-value
(1)	(2)	(3)	(4)	(5)	(6)	(7)	(8)	(9)	(10)	(11)	(12)
Close to the Galactic Plane (1 < |Z| < 2 kpc)											
Single Component											
−2.0 to −1.5	1851	−10	103	1.00	...	...	...	...	...	...	< 0.001
−1.5 to −1.0	2277	46	104	1.00	...	...	...	...	...	...	< 0.001
−1.0 to −0.6	2217	146	64	1.00	...	...	...	...	...	...	< 0.001
Two Components											
−2.0 to −1.5	1851	−104	136	0.13	4	89	0.86	...	...	...	< 0.01
−1.5 to −1.0	2277	1	96	0.67	135	44	0.33	...	...	...	< 0.001
−1.0 to −0.6	2217	64	77	0.19	165	42	0.81	...	...	...	< 0.001
Three Components											
−2.0 to −1.5	1851	−95	152	0.11	−24	83	0.71	93	48	0.19	0.272
−1.5 to −1.0	2277	−193	142	0.01	−3	88	0.63	135	45	0.36	0.175
−1.0 to −0.6	2217	54	79	0.15	146	40	0.58	198	25	0.27	0.137
Farther from the Galactic Plane (2 < |Z| < 4 kpc)											
Single Component											
−2.0 to −1.5	2115	−30	117	1.00	...	...	...	...	...	...	< 0.001
−1.5 to −1.0	2710	14	104	1.00	...	...	...	...	...	...	< 0.001
−1.0 to −0.6	1963	108	81	1.00	...	...	...	...	...	...	< 0.001
Two Components											
−2.0 to −1.5	2115	−162	156	0.14	−9	93	0.86	...	...	...	0.037
−1.5 to −1.0	2710	−7	98	0.85	133	45	0.15	...	...	...	0.007
−1.0 to −0.6	1963	32	88	0.29	139	52	0.71	...	...	...	0.058
Three Components											
−2.0 to −1.5	2115	−311	200	0.02	−168	95	0.14	0	88	0.84	0.857
−1.5 to −1.0	2710	−121	134	0.03	−8	91	0.80	134	48	0.17	0.816
−1.0 to −0.6	1963	38	88	0.33	133	45	0.60	220	11	0.07	0.096

NOTE. — In the labels: I = Comp. I, II = Comp. II, and III = Comp. III

and the MWTD (a highly retrograde component is represented by a fractional contribution of 0.5%, compared with a fractional contribution of 1% in the full-sample analysis).

For sub-sample B (the 1669 stars below the plane), in all metallicity regions, a one-cluster split was strongly rejected. Two-cluster splits were rejected for metallicity regions *i* and *iii*, but an acceptable fit was found for the intermediate-metallicity stars of region *ii*. The derived parameters for this split are consistent with the association of an inner-halo component ($\langle V_\phi \rangle = -6$ km s^{-1}, $\sigma_{V_\phi} = 104$ km s^{-1}) and a MWTD component ($\langle V_\phi \rangle = 150$ km s^{-1}, $\sigma_{V_\phi} = 45$ km s^{-1}). Once again, as found for the full-sample analysis, the intermediate-metallicity region in the three-cluster split provided evidence for only two significant contributors, identified as the inner halo and MWTD (a highly retrograde component is represented by a fractional contribution of 0.8%). The three-cluster split for the higher-metallicity region, while acceptable, had only two significant contributors, associated with the inner

halo and MWTD (a highly retrograde component contributed a 7% fraction). We conclude that, in spite of the rather large difference in the numbers of stars contained in the two sub-samples, individual analysis of these do not differ significantly from the analysis of the entire sample in this distance cut.

Similar to the above, we then split the local sample of stars with $1 < |Z| < 2$ kpc into two pieces: sub-sample C corresponding to stars located in the inner solar cylinder ($7 < R < 8.5$ kpc), and sub-sample D corresponding to stars located in the outer solar cylinder ($8.5 < R < 10.0$ kpc). The CLARA analysis with one-, two-, and three-cluster split was carried out within each sub-sample, and for all metallicity regions, followed by an R-mix mixture-model analysis using the starting points derived from CLARA. In the case of the splits on R, similar numbers of stars were included in each sub-sample (C: 3287 stars; D: 4129 stars).

The results of this exercise are as follows. For sub-sample

C, in all metallicity regions, one-cluster splits were strongly rejected (as before). Two-cluster splits were rejected for metallicity regions *i* and *ii*, while an acceptable two-cluster split was obtained for the higher-metallicity stars (metallicity region *iii*). The derived parameters for this split are roughly consistent with association of an inner-halo component ($\langle V_\phi \rangle$ = 61 km s^{-1}, σ_{V_ϕ} = 82 km s^{-1}) and a MWTD component ($\langle V_\phi \rangle$ = 154 km s^{-1}, σ_{V_ϕ} = 43 km s^{-1}). Three-cluster splits were found to be acceptable for metallicity regions *i* and *iii*, but were marginally rejected (p = 0.04) in the case of the intermediate-metallicity stars of region *ii*.

For sub-sample D, in all metallicity regions, 1-cluster splits were strongly rejected (as before). Two-cluster splits were rejected for metallicity regions *ii* and *iii*, while an acceptable 2-cluster split was obtained for the lower-metallicity stars in metallicity region *i*. The derived parameters for this split are consistent with the association with an outer-halo component ($\langle V_\phi \rangle$ = −97 km s^{-1}, σ_{V_ϕ} = 166 km s^{-1}) and an inner-halo component ($\langle V_\phi \rangle$ = −5 km s^{-1}, σ_{V_ϕ} = 87 km s^{-1}). Three-cluster splits were found to be acceptable in all three metallicity regions.

We conclude that the results obtained from these additional splits are fully consistent, within the expected variation induced by the different sub-sample sizes, with the previous results obtained of the full local samples in this distance interval.

5.6.3. *Farther from the Galactic Plane (2 < |Z| < 4 kpc)*

In this distance interval we expect that the contribution from the outer-halo component will increase in metallicity region *i*, while in this same region the contribution of the MWTD should be minimal. For metallicity region *ii* we expect that the MWTD, although present, should be of less importance than the contribution from the inner-halo component. For metallicity region *iii* we might expect that, as in the case of the distance interval close to the Galactic plane, the MWTD should dominate over the inner-halo component. As described below, all of these expectations are indeed met.

Inspection of Table 4 indicates that, as before, the p-values for the one-cluster and, to a somewhat lesser extent, the two-cluster splits, indicate that there is no metallicity region over which acceptable mixture-model fits exist. The p-value for the two-cluster split for metallicity region *iii* is marginal (p = 0.058), indicating that a two-cluster split is almost an acceptable fit. If one were to accept this split as reasonable, the mean velocities and dispersions suggest identification of component I with the inner halo, and component II with the MWTD. Statistically acceptable fits are only obtained for the three-cluster splits, as indicated by the listed p-values. This is also reflected in the appearance of the components shown in Figure 15, and their associated DRRs (with the exception of the lower panel for metallicity region *iii*, which suggests an even greater lack of fit for high rotation velocities than for the distance interval close to the plane).

We now examine the three-cluster splits in more detail.

For metallicity region *i* only components II and III are significant contributors. As can be seen in Table 4, the R-Mix procedure splits off a highly retrograde component, which may well be spurious, and in any case is only a minor (2%) contributor.

For metallicity region *ii* we identify component I with the outer halo, component II with the inner halo, and component III with the MWTD. Note, however, that component I again makes only a minor contribution, although its inclusion is apparently necessary to account for the asymmetric lower tail of the rotational velocity distribution.

For metallicity region *iii* we identify component I with the inner halo, and component II with the MWTD. Component III (which is clearly required, as seen from examination of the DRRs in the lower panel of Figure 15) makes only a minor (7%) contribution. This high-velocity feature is of interest, since it is stronger than the similar feature identified in the DRRs of this metallicity region in the distance interval closer to the plane. Further investigation of the nature of the stars in this region is clearly necessary, and is already underway. Stars with "thin-disk-like" metallicities and roughly solar (rather than thick-disk-like) [α-element/Fe] ratios located several kpc above the Galactic plane have been previously reported by Lee & Beers (2009), who speculated that such stars may have been originally formed in the thin disk, but were perturbed to large distances from the plane by past minor mergers. We defer a full discussion to a future paper.

We conclude that an independent MWTD component must exist in the region farther from the Galactic plane as well, in order to accommodate the observed rotational behavior of our local sample of stars. It is interesting to note how dominant the component we associate with the MWTD is (60%), relative to the component we identify with the inner halo (33%), for the metal-rich metallicity region. These roles quickly reverse in the intermediate-metallicity region, with the component associated with the inner halo accounting for 80% of the stars in this sample, and the component identified with the MWTD only 17%.

5.6.4. *The Metallicity Range of the MWTD*

Having established that a kinematically independent MWTD is indeed required in order to understand the rotational behavior of our local sample of stars, we now use a similar approach to the above to determine over what metallicity interval the MWTD is present. Ideally, we would like to have information on the shape of the MDF for this component, but our present data (due to the selection biases involved) is not suitable for such an analysis. We can, however, determine the upper and lower limits of its MDF. We accomplish this by considering metallicity regions *i* and *iii* (the lower- and higher-metallicity regions, respectively) for the distance interval close to the Galactic plane, where the MWTD component is more dominant and less overlapped with the inner-halo component than is the case for the interval farther from the plane.

For metallicity region *i* we repeat the $k = 2$ and $k = 3$ cluster-split experiments, lowering the upper limit on metallicity from [Fe/H] < −1.5, in steps of 0.1 dex, until a three-cluster split is no longer required, and a two-cluster split is adequate. That is, we seek the limiting metallicity where only the inner- and outer-halo components make significant (> 10%) contributions. We find that this occurs for the limit [Fe/H] < −1.8. Similarly, for metallicity region *iii*, we repeat the $k = 2$ and $k = 3$ cluster-split experiments, but this time raising the lower limit on metallicity from [Fe/H] > −1.0, in steps of 0.1 dex, until a three-cluster split is no longer required, and a two-cluster split is adequate. A successful two-cluster split would then only require the presence of an inner-halo and a canonical thick-disk component. We find that a two-cluster split is adequate for [Fe/H] > −0.8, although there is weak evidence for the presence of the MWTD even for −0.7 < [Fe/H] < −0.6.

We conclude from this exercise that the MWTD is a signif-

icant contributor to the numbers of stars in the local volume over the metallicity range $-1.8 < $ [Fe/H] $ < -0.8$, and possibly up to [Fe/H] ~ -0.7.

6. VELOCITY ELLIPSOIDS

We now derive estimates of the velocity ellipsoids for the thick disk, inner halo, and outer halo. A similar derivation has been attempted for the MWTD, as discussed at the end of this section. Note that all values of the velocity dispersions reported in this section are corrected for observational errors.

As already shown in Figure 6, the mean velocity in the (cylindrical coordinate) R and Z directions does not change with metallicity, remaining close to zero over all ranges of [Fe/H] considered. The behavior of the velocity dispersions is quite different, revealing a strong dependence on metallicity, as shown in Figure 16. In this figure the observed velocity dispersions for the V_R and V_Z components are plotted versus [Fe/H], with each bin representing an interval in metallicity of 0.1 dex. The observed trends are certainly related to the differing contributions of the various components in space and metallicity. In both panels the change in the behavior of the velocity dispersion versus metallicity (change in slope, and the increasing values) is particularly clear at $-1.0 < $ [Fe/H] $ < -0.5$, $-2.0 < $ [Fe/H] $ < -1.0$, and [Fe/H] $ < -2.0$. The first metallicity interval is dominated by the thick-disk population, with a mean dispersion of $\sigma_{V_R} \sim 60$ km s^{-1} and $\sigma_{V_Z} \sim 40$ km s^{-1}. In the second metallicity range the sample is dominated by the inner-halo population, with some overlap from the MWTD. Finally, the most metal-deficient stars, which are dominated by members of the outer-halo population, exhibit much higher dispersions. The dependence (or not) of the shape of the halo velocity ellipsoid with metallicity was a matter of considerable discussion in past work (e.g., Norris 1994; Carney et al. 1996; Chiba & Beers 2000). It was understandably difficult to resolve, due to the small numbers of stars in these previous samples. It is now clear that both the radial (σ_{V_R}) and vertical (σ_{V_Z}) velocity dispersions increase at lower abundances. Similar results have been reported by Bond et al. (2009).

For the thick disk, using the same metallicity ranges ($-0.8 < $ [Fe/H] $ < -0.6$) and distance ranges ($1 < |Z| < 2$ kpc) as chosen above for determination of the V_ϕ component, we obtain $\langle V_R \rangle = 2.5 \pm 2$ km s^{-1} and $\langle V_Z \rangle = 0.4 \pm 1$ km s^{-1}, and $\sigma_{V_R} = 53 \pm 1$ km s^{-1} and $\sigma_{V_Z} = 35 \pm 1$ km s^{-1}, for the radial and vertical velocity components, respectively.

To evaluate these quantities for the outer halo, we have explored a finer grid of metallicity for stars in the low-metallicity range ([Fe/H] $ < -2.0$), as shown in Figure 17. In each panel, the points represent the values of the dispersions for a metallicity below [Fe/H]$_{max}$, the maximum metallicity for stars in each sub-sample. As in Figure 16, the dispersions are corrected for the observational errors.

As shown in the upper panel of Figure 17, the dispersion of the V_R component is constant (or slightly increasing) in the range of metallicity $-2.4 < $ [Fe/H]$_{max} < -2.0$, reaching a value of $\sigma_{V_R} \sim 180$ km s^{-1} at the lowest metallicity. Similar behavior can be noticed for the velocity dispersion in the vertical direction. A constant value of about $\sigma_{V_Z} \sim 120$ km s^{-1} is obtained for $-2.4 < $ [Fe/H]$_{max} < -2.0$, falling slightly for the more metal-poor stars (albeit with large error bars). We adopt the mean velocities and dispersions for the outer halo

corresponding to the metallicity upper limit [Fe/H]$_{max} = -2.2$ (i.e., [Fe/H] $ < -2.2$), where contamination from the inner halo should be minimal. These are $\langle V_R \rangle = -8.6 \pm 6.1$ km s^{-1} and $\langle V_Z \rangle = 1.9 \pm 4.4$ km s^{-1}, and $\sigma_{V_R} = 159 \pm 4$ km s^{-1} and $\sigma_{V_Z} = 116 \pm 3$ km s^{-1}, for the radial and vertical components, respectively.

Determination of the velocity ellipsoid for the inner-halo population proved more challenging. A series of experiments in the range of metallicity $-2.0 < $ [Fe/H] $ < -1.5$, where contamination from the outer halo should be minimized, were been carried out to obtain this information from a mixture-model analysis. However, the symmetry of the distribution for both the V_R and V_Z components precluded obtaining accurate estimates. Recall that, due to the existence of clear correlations between Z_{max} and other kinematic parameters, we cannot use Z_{max} in order to reduce the contamination of the inner halo by other components that are present in this metallicity interval (the outer halo and MWTD). When a two-component model is adopted, with the outer-halo parameters fixed, the R-Mix procedure provides estimates, for the radial cmponent, of $\langle V_R \rangle = 3 \pm 17$ km s^{-1}, and $\sigma_{V_R} = 143 \pm 14$ km s^{-1} (p-value $\sim$ 0.07; i.e., marginally adequate). The same experiment for the vertical velocity component does not provide an adequate fit.

Frustrated by the mixture-model approach, we chose to obtain at least an estimated velocity ellipsoid for the inner halo by simply adopting the mean velocities and dispersions of the sub-sample of stars in this same metallicity range, with the knowledge that contamination from other components may still be present. This results in estimates of $\langle V_R \rangle = 3.0 \pm 2.4$ km s^{-1} and $\langle V_Z \rangle = 3.4 \pm 1.4$ km s^{-1}, and $\sigma_{V_R} = 150 \pm 2$ km s^{-1} and $\sigma_{V_Z} = 85 \pm 1$ km s^{-1}, for the means and dispersions of the radial and vertical velocity components, respectively. Note that these estimates agree, within the errors, with the $\langle V_R \rangle$ and σ_{V_R} estimated using the mixture-model analysis above.

Finally, we have attempted to estimate the remaining components of the velocity ellipsoid for the MWTD. Based on the results obtained in §5.6.1, we have selected a sub-sample of stars with $-1.5 < $ [Fe/H] $ < -1.0$ and distance interval $1 < |Z| < 2$ kpc, in which the dominant components are the inner halo and the MWTD (Table 4). When the R-Mix mixture-modeling analysis is employed with the stellar fractions of the two components fixed at the values reported in Table 4, a two-component model provides very good fits, with values $\langle V_R \rangle = -13 \pm 5$ km s^{-1} and $\langle V_Z \rangle = -14 \pm 5$ km s^{-1}, and $\sigma_{V_R} = 64 \pm 4$ km s^{-1} and $\sigma_{V_Z} = 48 \pm 3$ km s^{-1}. When corrected for the observational errors, the dispersions are $\sigma_{V_R} = 59 \pm 4$ km s^{-1} and $\sigma_{V_Z} = 44 \pm 3$ km s^{-1}, respectively. One-component models are strongly rejected, with p-values < 0.001. The two-component fit reveals a slight asymmetry in both of the velocity distributions. This asymmetry may be an indication that the orbits of stars in the MWTD component are non-circular and/or non-coplanar with those of stars in the thin disk. Figure 18 shows the fits obtained and the associated DRRs. Table 5 lists our final determinations of the velocity ellipsoids for the thick disk, MWTD, inner halo, and outer halo.

It should be noted that, in addition to errors in our determination of the parameters of the velocity ellipsoids that arise from observational errors (affecting primarily the derived dispersions, which we attempt to correct for), there remain systematic errors that result from the propagation of errors in the distance estimates and proper-motion measurements. Monte Carlo experiments indicate that such errors are typically on

[!t]

TABLE 5
VELOCITY ELLIPSOIDS

Component	$\langle V_R \rangle$ (km s^{-1})	$\langle V_\phi \rangle$ (km s^{-1})	$\langle V_Z \rangle$ (km s^{-1})	σ_{V_R} (km s^{-1})	σ_{V_ϕ} (km s^{-1})	σ_{V_Z} (km s^{-1})
Thick Disk	3 ± 2	182 ± 2	0 ± 1	53 ± 2	51 ± 1	35 ± 1
MWTD	-13 ± 5	125 ± 4	-14 ± 5	59 ± 3	40 ± 3	44 ± 3
Inner Halo	3 ± 2	7 ± 4	3 ± 1	150 ± 2	95 ± 2	85 ± 1
Outer Halo	-9 ± 6	-80 ± 13	2 ± 4	159 ± 4	165 ± 9	116 ± 3

NOTE. — The reported values of V_ϕ and σ_{V_ϕ} for the MWTD are put in the center of the ranges estimated for this component reported in the text. The derived velocity dispersions of the velocity ellipsoids are corrected for the effects of observational errors, typically on the order of 5-6 km s^{-1} for large sub-samples, and 10-15 km s^{-1} for smaller sub-samples. Note that the errors listed in this table and throughout the text refer to random errors only, and do not take into account the existence of systematic errors, primarily related to uncertainties in the photometric distances, which are expected to be at least on the order of 10% (and in some cases as large as 15-20%).

the order of 5 km s^{-1}. These are not reported as separate components of the errors listed in Table 5.

An additional and much more difficult to quantify error comes from our use of the mixture-modeling approach itself. Finite mixture models, by definition, force the observed distribution of kinematic quantities to be described by the adopted number of components, and normalize the derived model to the sum of these components. If a component is *unrecognized*, and not included in the model, the recognized components are forced to take up its missing "signal", and to adjust their derived parameters accordingly. For instance, if we were not to include the MWTD component, the parameters of the thick disk, inner halo, and outer halo would be altered in an attempt to accommodate the observed data. The same would apply, to an extent, if a superfluous component is included. These problems can be mitigated by statistical tests of the ability of the derived model to fit the observed distribution, but they cannot be entirely eliminated. This is particularly the case when one or more of the components are strongly overlapping in the kinematic quantities being modeled. The best defense against "mixture-model errors" of this sort is the examination of different samples of stars, ideally selected in different ways or over different ranges of distance, such that they sample the underlying components in ways that break possible degeneracies. In future analyses we plan to consider the kinematic properties of F-turnoff stars, G dwarfs, and subdwarf M stars from SDSS/SEGUE, which should provide tests of the necessity (or not) of the presence of our adopted components in the mixture-model analysis.

7. ON THE THICK-DISK SCALE LENGTH AND SCALE HEIGHT

With the velocity-ellipsoid parameters for the canonical thick disk in hand, we can estimate its scale length and scale height by assuming that it is in equilibrium and well-mixed. Chiba & Beers (2000) estimated the scale length of the thick disk from its stellar kinematics, using their Eqn. 1, which assumes that the scale height of the thick disk is constant and that the ratio of σ_{V_R} to σ_{V_Z} is independent of radius. With their adopted values for the velocity dispersions and mean rotational velocity, Chiba & Beers derive a scale length of 4.5 kpc for the thick disk.

In this paper we do not need to make the above assumptions – we have a sufficient number of stars occupying a large enough region of space to measure the gradients in σ_{V_R} and

σ_{V_Z} directly. We assume that the thick disk has an exponential density distribution in R and Z, with scale length h_R and scale height h_Z, respectively. The cross term, $\sigma_{V_{R,Z}}$, of the velocity dispersion is observed to be small for the thick disk. It takes a value of $\sigma_{V_{R,Z}} = 0.096 \pm 0.020$ at $1 < |Z| < 2$ kpc, and $-0.8 <$ [Fe/H] < -0.6 (§9), so we can write the radial and Z-components of the Jeans Equation as

$$\frac{\partial \ln \sigma_{V_R}^2}{\partial R} - \frac{1}{h_R} + \frac{1}{R}\left\{1 - \frac{\sigma_{V_\phi}^2}{\sigma_{V_R}^2} + \frac{V_c^2 - \langle V_\phi \rangle^2}{\sigma_{V_R}^2}\right\} = 0 \qquad (6)$$

$$\frac{\partial \ln \sigma_{V_Z}^2}{\partial Z} - \frac{1}{h_Z} + \frac{K_Z}{\sigma_{V_Z}^2} = 0 \qquad (7)$$

where V_c and K_Z are the circular velocity and vertical acceleration. We measure the radial gradient of σ_{V_R} and the Z-gradient of σ_{V_Z} from our sample, and use the Kuijken & Gilmore (1991) estimate of $K_Z = 2\pi G \times 71\ M_\odot$ pc^{-2} at $|Z| = 1.1$ kpc. We adopt the following parameters for the velocity dispersion and mean motion of the canonical thick disk at the solar radius, and at a Z-height of 1.1 kpc: $(\sigma_{V_R}, \sigma_{V_\phi}, \sigma_{V_Z}) = (53 \pm 2, 51 \pm 1, 35 \pm 1)$ km s^{-1} and $\langle V_\phi \rangle = 182 \pm 2$ km s^{-1}.

Over the interval $6 < R < 12$ kpc and $1 < |Z| < 3$ kpc, respectively, the variations in σ_{V_R} and σ_{V_Z} closely follow a linear behavior, with $\partial \sigma_{V_R}/\partial R = -5.8 \pm 1.3$ km s^{-1} kpc^{-1} and $\partial \sigma_{V_Z}/\partial |Z| = 6.8 \pm 1.7$ km s^{-1} kpc^{-1}, respectively. With these parameters, the scale length for the thick disk is $h_R = 2.20 \pm 0.35$ kpc, and the scale height is $h_Z = 0.51 \pm 0.04$ kpc, where the errors represent the statistical uncertainties only.

The small value of h_R relative to the Chiba & Beers value comes about almost entirely because our mean motion for the thick disk ($\langle V_\phi \rangle = 182$ km s^{-1}) is significantly smaller than their value of 200 km s^{-1}. However, we note that several other authors also find a small value of h_R from independent arguments based on star counts, e.g., Reylé & Robin (2001).

Our value for the scale height of the thick disk is at the lower end of the range of previously reported estimates, so we must look critically at the input data from which h_Z was derived. The parameters which are used in estimating h_Z are K_Z, σ_{V_Z} and its gradient, all evaluated at $|Z| = 1.1$ kpc. The value of K_Z at $|Z| = 1.1$ kpc comes from the Kuijken & Gilmore (1991) sample of K dwarfs, and is consistent with the known density of disk objects. It is also in excellent agreement with the K_Z value independently determined by Holmberg & Flynn

(2000). For determining σ_{V_Z} and its gradient, we chose stars from a narrow range of metallicity, $-0.8 <$ [Fe/H] < -0.6. Although the values of σ_{V_Z} and its gradient are well determined by our data, it is possible that our thick-disk sample at $|Z| = 1.1$ kpc is contaminated by thin-disk stars, which would reduce the apparent value of σ_{V_Z} and lead to an underestimate of h_Z. Contamination by inner-halo stars could also lead to an incorrect estimate of $\partial\sigma_{V_Z}/\partial|Z|$. However, the positive gradient of σ_{V_Z} makes only a relatively minor contribution to the derived value of h_Z. For example, if the thick disk σ_{V_Z} were in fact isothermal, the value of h_Z would increase from 0.51 to only 0.64 kpc.

We note that our kinematic estimate of the scale height of the thick disk is obtained at $|Z| = 1.1$ kpc, while the (usually larger, $h_Z \sim 1$ kpc) estimates come from star counts at $|Z| \sim$ 2 to 4 kpc (eg Gilmore & Reid 1983). Although the thick disk is often represented as vertically exponential, and indeed appears to be exponential at larger $|Z|$, in fact it is unlikely to be strictly exponential. In the general version of the vertical Jeans Equation the $1/h_Z$ term in Eqn 7 is replaced by $\partial ln\nu/\partial Z$, where $\nu(Z)$ is the vertical density distribution. If we adopt the form of $K_Z(Z)$ from Holmberg & Flynn (2000), and we assume that the thick disk is vertically isothermal with a velocity dispersion $\sigma_{V_Z} = 35$ km s^{-1}, then the Jeans Equation can be integrated numerically to derive $\nu(Z)$. Near the Galactic plane, $\nu(Z)$ changes slowly with $|Z|$ and becomes steeper as Z increases. At $|Z| = 1.1$ kpc, the "local scale height" $[-1/(\partial ln\nu/\partial Z)]$ agrees almost exactly with our value of 0.64 kpc, as it must. On the other hand, one could define an effective scale height of the thick disk as the height above the Galactic plane at which $\nu(Z)$ has decreased by a factor e from its value at $Z = 0$. This height is 0.99 ± 0.04 kpc, but it is not directly comparable with the star-count scale heights at larger $|Z|$.

For the MWTD we have only the kinematic parameters given in Table 5, but these are sufficient to place some useful constraints on the radial structure of this component. As we have no information on the radial gradient of the velocity dispersion for this component, we assume that it follows the often-adopted relation $\sigma_{V_R}^2 \propto \exp(-R/h_\sigma)$, where h_σ is a length scale. Then it follows from the radial component of the Jeans Equation that

$$\frac{1}{h_\sigma} + \frac{1}{h_R} = 1.04 \text{ kpc}^{-1} \qquad (8)$$

If the two scale lengths are comparable, as they would be for a disk of uniform scale height and constant anisotropy, then the radial scale length of the MWTD is again short, ~ 2 kpc.

Regarding the scale height for the MWTD, we find at $|Z| = 1.1$ kpc (and adopting the velocity dispersion reported in Table 5, $\sigma_{V_Z} = 44 \pm 3$ km s^{-1}) a value of h$_Z = 1.36 \pm 0.13$ kpc.

8. DENSITY PROFILES FOR THE STELLAR HALO COMPONENTS

Assuming that the Galaxy is in dynamical steady state, the Jeans Equation for a spherically symmetric stellar system, in spherical coordinates (r,θ,ϕ), can be written as (Binney & Tremaine 1988):

$$\frac{d(\rho\langle V_r^2\rangle)}{dr} + \frac{\rho}{r}[2\langle V_r^2\rangle - (\langle V_\theta^2\rangle + \langle V_\phi^2\rangle)] = -\rho\frac{d\Phi}{dr} \qquad (9)$$

where $\langle V_i^2\rangle$ $(i = r, \theta, \phi)$ is related to the velocity dispersion σ_i^2 as:

$$\sigma_i^2 = \langle V_i^2\rangle - \langle V_i\rangle^2. \qquad (10)$$

Based on the well-supported assumption for both the inner and outer halos, $\langle V_r\rangle = 0$, and $\langle V_\theta\rangle = 0$, the above equation can written as:

$$\frac{1}{\rho}\frac{d(\rho\sigma_{V_r}^2)}{dr} + \frac{2}{\rho}\sigma_{V_r}^2[1 - \frac{\sigma_{V_\theta}^2 + \sigma_{V_\phi}^2}{2\sigma_{V_r}^2} - \frac{\langle V_\phi\rangle^2}{2\sigma_{V_r}^2}] = -\frac{d\Phi}{dr} \qquad (11)$$

where σ_{V_r}, σ_{V_θ}, σ_{V_ϕ}, are the velocity dispersions in the directions of (r, θ, ϕ), respectively (in the spherical system V_ϕ and V_θ are taken positive in the direction of Galactic rotation and in the direction away from the North Galactic Pole, respectively).

The anisotropy parameter, β, which describes the degree of anisotropy of the velocity distributions, is defined as $\beta = 1 - (\sigma_{V_t}/\sigma_{V_r})^2$, where σ_{V_r} and σ_{V_t} are the radial and tangential velocity dispersions, respectively. The latter is given by $\sigma_{V_t}^2 = \frac{1}{2}(\sigma_{V_\phi}^2 + \sigma_{V_\theta}^2)$. The values of the anisotropy parameter obtained with our dataset are $\beta_{in} = 0.6$ for the inner halo and $\beta_{out} = 0.2$ for the outer halo. The anisotropy parameters for the inner halo indicate that its velocity ellipsoid is radially elongated, while the outer halo exhibits a less radially-elongated shape for its velocity ellipsoid.

Assuming that the potential of the Galactic halo is approximately spherical and logarithmic, $\Phi(r) = V_c^2 \ln r$, which corresponds to a flat rotation curve of the Galaxy in the solar neighborhood, and assuming also $V_c(r) = V_c = 220$ km s^{-1}, Eqn. 11 can be written as:

$$V_c^2 = -\sigma_{V_r}^2(\frac{dln\rho}{dlnr} + \frac{dln\sigma_{V_r}^2}{dlnr} + 2\beta - \frac{\langle V_\phi\rangle^2}{\sigma_{V_r}^2}) \qquad (12)$$

The density of stars in the Galactic halo components can be approximated by a power-law relation $\rho(r) \propto r^n$ (where n is negative, due to the finite extent of the Galaxy). Making this substitution, the previous equation becomes:

$$V_c^2 = -\sigma_{V_r}^2(n + \frac{dln\sigma_{V_r}^2}{dlnr} + 2\beta - \frac{\langle V_\phi\rangle^2}{\sigma_{V_r}^2}) \qquad (13)$$

Note that the term $\langle V_\phi\rangle^2/\sigma_{V_r}^2$ is negligible for the inner halo ($\langle V_\phi\rangle = 7$ km s^{-1}), while it is *not negligible* for the outer halo ($\langle V_\phi\rangle = -80$ km s^{-1}). The values obtained for this term are, for the inner halo, $\langle V_\phi\rangle^2/\sigma_{V_r}^2 = 2\cdot10^{-3}$, and for the outer halo, $\langle V_\phi\rangle^2/\sigma_{V_r}^2 = 0.25$.

In the solar neighborhood (R = R$_\odot$) we can use the velocity ellipsoids obtained in the cylindrical reference system (σ_{V_R}, σ_{V_ϕ}, σ_{V_Z}) to derive the parameter n from the previous equation for the two halo components. Adopting the values of the velocity ellipsoid reported in Table 5, we find the following power law for the two components:

$$\rho_{in} \sim r^{-3.17\pm0.20} \qquad \rho_{out} \sim r^{-1.79\pm0.29}$$

The above estimate includes the term $dln(\sigma_{V_r}^2)/dlnr$ in Eqn. 13, which takes into account the variation of σ_{V_r} as a function of the radius r. In the solar neighborhood it becomes

$dln(\sigma^2_{V_r})/dlnr \sim dln(\sigma^2_{V_R})/dlnR$. This term has been evaluated by examining σ_{V_r} in 1 kpc intervals, in the range $6 < R <$ 12 kpc, using the low-metallicity sub-sample ([Fe/H] < -2). The minimum and maximum values of the dispersion in the above ranges are $\sigma_{V_R} = 156 \pm 9$ km s^{-1}, and $\sigma_{V_R} = 172 \pm 8$ km s^{-1}, respectively. By taking the logarithm and fitting the corresponding curve, we obtain $dln\sigma^2_{V_R}/dlnr = -0.26$.

Note that if the above term is neglected in Eqn. 13 we obtain:

$$\rho_{in} \sim r^{-3.43 \pm 0.20} \qquad \rho_{out} \sim r^{-2.05 \pm 0.29}$$

Thus, this term has a considerable effect, and needs to be included. Regardless, our analysis points to an outer-halo population with a much shallower spatial density profile than that of the inner-halo population.

9. EVIDENCE FOR TILTS IN THE DERIVED VELOCITY ELLIPSOIDS

The orientation of the velocity ellipsoids is of interest for understanding the equilibrium and assembly of the various Galactic components, and has recently been studied by Siebert et al. (2008), Bienayme et al. (2009), and Smith, Evans, & An (2009), as well as by Bond et al. (2009). We have examined the (R, Z) kinematics of our local sample in order to estimate the tilts of the velocity ellipsoids as a function of the height above the Galactic plane and metallicity.

We note that it is not appropriate to use the maximum vertical height of the orbit, Z_{max}, as a parameter here, because selecting on Z_{max} is equivalent to a selection in the velocity components V_R and V_Z. This makes it difficult to separate the tilt for the inner and outer halos.

Figure 19 shows the velocity distribution in the (V_R, V_Z) plane as a function of the vertical distance, $|Z|$, and metallicity. Close to the Galactic plane (top panels), at $0 < |Z| < 1$ kpc, and at metallicity $-0.8 < $ [Fe/H] < -0.6, the sub-sample contains mostly thick-disk stars, and the inclination of the velocity ellipsoid is small. At higher $|Z|$ values, the inclination slightly increases, possibly due to contamination from the MWTD and the metal-rich part of the inner halo. At intermediate metallicity (middle panels), $-1.5 < $ [Fe/H] < -0.8, the ellipsoid shows a strong inclination, increasing with $|Z|$. We note that this intermediate sample comprises two overlapping components, the MWTD and the inner halo, with contamination from the canonical thick disk and the outer halo. The thick disk and MWTD cannot be easily separated in the V_R and V_Z component, as already discussed in §6. The low-metallicity sample (bottom panel), [Fe/H] < -1.5, which contains mostly halo stars, again exhibits a strong inclination increasing with $|Z|$.

The tilt of the velocity ellipsoid in cylindrical coordinates can be described by the tilt angle and the correlation coefficient, given by:

$$\tan 2\alpha = \frac{2\sigma^2_{V_{R,Z}}}{(\sigma^2_{V_R} - \sigma^2_{V_Z})} \tag{14}$$

$$C[V_R, V_Z] = \frac{\sigma^2_{V_{R,Z}}}{(\sigma^2_{V_R}\sigma^2_{V_Z})^{1/2}} \tag{15}$$

where $\sigma_{V_{R,Z}}$ is the covariance. The values obtained for the tilt angle and the correlation coefficient, in various ranges of the vertical distance and metallicity, are listed in Table 6. The

[!t]

TABLE 6
VELOCITY ELLIPSOIDS: TILT AND CORRELATION

[Fe/H]	Tilt Angle	$C[V_R, V_Z]$
Close to the Galactic Plane ($1 < |Z| < 2$ kpc)		
−0.8 to −0.6	$7°.1 \pm 1°.5$	0.096 ± 0.020
−1.5 to −0.8	$10°.3 \pm 0°.4$	0.224 ± 0.009
< -1.5	$8°.6 \pm 0°.5$	0.151 ± 0.008
Farther from the Galactic Plane ($2 < |Z| < 4$ kpc)		
−0.8 to −0.6	$5°.2 \pm 1°.2$	0.106 ± 0.024
−1.5 to −0.8	$15°.1 \pm 0°.3$	0.367 ± 0.007
< -1.5	$13°.1 \pm 0°.4$	0.248 ± 0.008

errors on α and C are evaluated through a Monte Carlo simulation (10000 realizations for each star), using the velocity errors for individual stars and correcting for the effect of the errors on the diagonal σ terms. We find that the tilt angle is statistically different from zero for all the selected samples, and the principal axes of the velocity ellipsoids point towards a location slightly above the Galactic center. For metal-rich stars close to the Galactic plane we obtain $\alpha = 7°.1 \pm 1°.5$, which is consistent with the inclination found by Siebert et al. 2008 ($7°.3 \pm 1°.8$) for a sample of stars at $|Z| < 1$ kpc. At intermediate metallicity and $1 < |Z| < 2$ kpc, the inclination is $\alpha = 10°.3 \pm 0°.4$; it increases to $15°.1 \pm 0°.3$ farther from the Galactic plane. These intermediate-metallicity samples are dominated by the MWTD and inner halo. Finally, at low metallicity, the sample comes mainly from the overlapping inner-/outer-halo populations, and the inclination of the velocity ellipsoid is $\alpha = 8°.6 \pm 0°.5$ and $13°.1 \pm 0°.4$ at $1 < |Z| < 2$ kpc, and $2 < |Z| < 4$ kpc, respectively.

Having demonstrated that the velocity ellipsoid for the inner halo is pointing close to the Galactic center, we re-evaluated its velocity ellipsoid in spherical coordinates, in order to evaluate whether the inner halo is kinematically close to isotropic in (θ, ϕ). If it were so, then the inner-halo kinematics would be consistent with a system for which the distribution function depends on energy and the *total* angular momentum, which would in turn be an interesting clue to its assembly. The sample was selected in the range of metallicity of $-2.0 <$ [Fe/H] < -1.6 and $2 < |Z| < 4$ kpc, where the dominant component is the inner halo, albeit with contamination from the MWTD and the outer halo. A similar estimate for the outer halo is more uncertain, due to the difficulty in separating the two halo components, as mentioned above. However, we have attempted to select mostly outer-halo stars using the metallicity interval [Fe/H] < -2.4 and $2 < |Z| < 4$ kpc, being aware that the sample remains contaminated by the inner halo. For the inner halo, we find $(\sigma_{V_r}, \sigma_{V_\phi}, \sigma_{V_\theta}) = (160 \pm 3, 102 \pm 2, 83 \pm 2)$ km s^{-1} and for the outer halo $(\sigma_{V_r}, \sigma_{V_\phi}, \sigma_{V_\theta}) = (178 \pm 9, 149 \pm 7, 127 \pm 6)$ km s^{-1} respectively. We conclude that both halo components are significantly anisotropic in (θ, ϕ).

10. THE MDF OF THE FULL SAMPLE AS A FUNCTION OF HEIGHT ABOVE THE GALACTIC PLANE

There is a sufficient number of stars in the DR7 calibration-star sample to construct "as observed" MDFs for the entire sample (regardless of whether the star has an available proper

motion, or is located within the cylinder we have defined above for the local sample of stars), in order to look for confirmation of the expected changes as a function of height above the Galactic plane. The number of stars employed is 30956.

We examine the MDFs for different intervals in |Z|, with cuts chosen to ensure there remain adequate numbers of stars in each interval.

Figure 20 shows the results of this exercise. Examination of the left-hand column of panels in this figure shows how the MDF changes from the upper panel, in which there are obvious contributions from the thick-disk, MWTD, and inner-halo components in the cuts close to plane, to the lower panel, with an MDF dominated primarily by inner-halo stars. In the right-hand column of panels, with distances from the plane greater than 5 kpc, the transition from inner-halo dominance to a much greater contribution from outer-halo stars is obvious. This demonstration is, by design, independent of any errors that might arise from derivation of the kinematic parameters, and provides confirmation of the difference in the chemical properties of the inner- and outer-halo populations originally suggested by Carollo et al. (2007).

Although it might appear possible to attempt mixture-model analysis to obtain MDFs for each of the individual components, we recall that biases in the selection of the stars in the calibration-star sample would confound such an attempt. Other samples of SDSS stars, which are more suitable for such an analysis, are being studied for this purpose, and will be reported on in due course.

11. SUMMARY AND DISCUSSION

We have analyzed the SDSS/SEGUE sample of 32360 unique calibration stars from DR7, amplifying the previous analysis carried out by Carollo et al. (2007) on a smaller sample of similar stars from DR5. A Maximum Likelihood analysis of a local sub-sample of 16920 calibration stars has been developed in order to extract kinematic information for the major Galactic components (thick disk, inner halo, and outer halo), as well as for the elusive metal-weak thick disk (MWTD). We have measured velocity ellipsoids for the thick disk, the MWTD, the inner halo, and the outer halo, demonstrated the need for a MWTD component that is kinematically and chemically independent of the canonical thick disk (and put limits on the metallicity range of the MWTD MDF), obtained estimates of the scale length and scale height of the thick disk and MWTD, and derived the inferred spatial density profiles of the inner/outer halo components by use of the Jeans Equation. We have also presented evidence for tilts in the velocity ellipsoids for stars in our sample as a function of height above the plane, for several ranges in metallicity. Changes in the *in-situ* observed MDF for the full calibration-star sample, as a function of height above the Galactic plane, are consistent with those expected from kinematic analysis of the local sample. Our results are summarized and compared with previous related analyses below, followed by a discussion on their implication for the formation of the Milky Way in the context of other recent results.

11.1. *Summary of Results and Comparison with Previous Work*

We began by comparing the changes in the nature of the calibration-star sample that have occurred in going from the SDSS DR5 to the DR7 data releases. Aside from the 60% increase in the total sample size, the addition of numerous low-latitude observations from SEGUE, and recent improvements

in the SSPP (in particular for the determination of metallicities for metal-rich stars) have enabled much clearer distinctions between the kinematic behavior of the various Galactic components we consider in our analysis.

11.1.1. *Distribution of Orbital Eccentricity*

The distribution of observed orbital eccentricity for our local sample of stars contains interesting information on the presence of various Galactic components as a function of height above the Galactic plane and over a number of cuts in metallicity. We found that, in the metallicity range $-1.0 <$ [Fe/H] < -0.6, the canonical thick disk dominates close to the Galactic plane ($1 < |Z| < 2$ kpc), as well as at $2 < |Z| < 4$ kpc. At intermediate metallicity, $-1.5 <$ [Fe/H] < -1.0, the distribution exhibits an interesting feature extending to $e \sim 0.5$, suggesting a likely MWTD population close to the Galactic plane. At larger distances the distribution appears more consistent with the inner-halo population. In the metallicity range $-2.0 <$ [Fe/H] < -1.5 the distribution assumes the form $f(e) \sim e$, which is associated entirely with the inner-halo population, and consistent with a well-mixed steady-state system of test particles for which the distribution function depends only on energy. In contrast to this behavior, we noted that the distribution of orbital eccentricity for the most metal-poor stars in our local sample ([Fe/H] < -2.0) deviates significantly from linearity. Such a distribution reflects the contribution from an outer-halo population with a smaller fraction of stars on high-eccentricity orbits.

11.1.2. *Identification of Halo Components*

We next explored which quantities can best be used to constrain the mixtures of components present in the local calibration-star sample, concluding that V_ϕ and Z_{max} are superior to available alternatives. [15] The subtle, but important, question of how many components are required to account for the observed kinematics of halo stars in the local sample was then considered. On the basis of an objective clustering approach, applied to the low-metallicity sub-sample of local stars with [Fe/H] < -2.0, we demonstrated that (a) a single-population halo is incompatible with the observed kinematics, that (b) a dual-component halo, comprising populations we associate with the inner and outer halo, is sufficient to accommodate the observed kinematics, and that (c) although additional components (of unspecified physical meaning) can be added, they are not required (and in any case, provide no statistically significant improvement in the kinematic fits). We concluded that a dual-halo model is preferred on the grounds of its simplicity. Previous claims for the existence of a complex (often, dual) halo have been made over the past few decades, but these were based on rather small samples of tracer stars or clusters, such that the statistical significance of the dual signature was difficult to assess (e.g., Norris 1994; Carney et al. 1996). We believe the existence of an inner/outer halo structure is now clearly confirmed.

11.1.3. *Maximum Likelihood Analysis of Halo-Component Kinematics*

---

[15] After the majority of our analysis was completed, we also investigated using the meridional velocity, defined as $V_M = (V_R^2 + V_Z^2)^{1/2}$, as a possible variable for separation of the inner- and outer-halo components. This experiment proved interesting (i.e., a retrograde V_ϕ was found for stars with high V_M). This variable is worthwhile to investigate further, since it does not require adoption of a gravitational potential, as is the case for Z_{max}.

We developed a flexible Maximum Likelihood (ML) approach for further analysis of the kinematics of Galactic components. We then used a low-metallicity sub-sample of local stars in order to obtain estimates of the mean rotational velocity and dispersion of the outer-halo population, obtaining values of $\langle V_\phi \rangle = -80 \pm 13$ km s^{-1}, slightly more retrograde than that obtained by Carollo et al. (2007) (~ -70 km s^{-1}) from the DR5 sample of local calibration stars. For the dispersion, we obtained $\sigma_{V_\phi} = 180 \pm 9$ km s^{-1} ($\sigma_{V_\phi} = 165 \pm 9$ km s^{-1} when corrected for observational errors), a substantially larger value than reported by previous authors who considered only a single-component halo. The ML approach was then used in order to estimate the rotation and dispersion of the inner-halo component, based on an examination of cuts on Z_{max} for the low-metallicity sub-sample. We obtained values for stars with $1 < Z_{max} < 10$ kpc (where the inner-halo component dominates) of $\langle V_\phi \rangle = 7 \pm 4$ km s^{-1}, i.e., an essentially non-rotating inner halo, and $\sigma_{V_\phi} = 110 \pm 3$ km s^{-1} ($\sigma_{V_\phi} = 95 \pm 2$ km s^{-1} when corrected for observational errors). These values do not change substantially when considering cuts on Z_{max} up to 30 kpc from the plane, although the derived fraction of inner-halo stars decreases with distance while the fraction of outer-halo stars increases with distance.

We note that while candidate outer-halo stars with large Z_{max} exhibit a large retrograde mean rotation *in the solar neighborhood*, these stars would have a smaller value of *in-situ* rotational velocity at greater Galactocentric distances. This is because an orbit with large Z_{max} tends to have large R_{apo}, and thus smaller $|V_\phi|$, at large Galactocentric distance, due the conservation of angular momentum. The azimuthal velocity at R_{apo}, $V_{\phi,apo}$ can be simply evaluated as $V_{\phi,apo} = V_\phi \cdot (R/R_{apo})$. Using the sub-sample with [Fe/H] < -2 and $Z_{max} > 10$ kpc, we obtain $\langle V_{\phi,apo} \rangle = -14 \pm 2$ km s^{-1} as the most likely *in-situ* mean rotation of outer-halo stars, given that stars are most probably observed when they are near their apocentric distances. It is worth exploring this small amount of *in-situ* retrograde rotation in numerical simulations of galaxy formation and/or kinematic observations of extragalactic halos, in order to compare with the present results for the Milky Way. We also note that the expected *in-situ* velocity dispersion of an outer-halo population also must decrease with distance, as can be verified by inspection of the Jeans Equation. Indeed, observations of distant samples of stars, which are expected to be dominated by members of the outer-halo population, have been shown by a number of authors to meet this expectation, at least for the radial-velocity component (e.g, Sommer-Larsen et al. 1997; Xue et al. 2008; Brown et al. 2009). It should be kept in mind that Sommer-Larsen et al. (1997) have also pointed out that the *nature* of the orbits of the more distant stars must change from locally radially anisotropic to tangentially anisotropic (with a transition point at around 20 kpc), in order to be consistent with a flat rotation curve. This latter point will prove challenging to verify observationally *in-situ* until high-quality proper motions for more distant stars can be obtained, e.g., with the Gaia mission.

In the analysis of Chiba & Beers (2000), which only considered a single halo component, a slightly more prograde inner halo was obtained (based on stars with [Fe/H] < -2.0), $\langle V_\phi \rangle \sim 30$ km s^{-1}, along with a similar dispersion, $\sigma_{V_\phi} = 106 \pm 9$ km s^{-1}. The existence of a gradient in the mean rotational velocity for the inner-halo component, as claimed previously by Chiba & Beers (2000), is confirmed. We obtained

a value of $\triangle \langle V_\phi \rangle / \triangle |Z| = -28 \pm 9$ km s^{-1} kpc^{-1}, for stars located within 2 kpc of the Galactic plane. This gradient is substantially lower than the value reported by Chiba & Beers ($\triangle \langle V_\phi \rangle / \triangle |Z| = -52 \pm 6$ km s^{-1} kpc^{-1}). Note that the gradient reported by Chiba & Beers is based on a sample of stars primarily located within 1 kpc of the plane; beyond 1 kpc, their three bins are consistent with zero net rotation. Thus, the apparent difference in the gradient of the inner-halo population obtained with our present sample of local calibration stars may be related to the subtantially larger number of stars included with $1 < |Z| < 2$ kpc, lowering the derived gradient. In any case, such a gradient may represent the signature of a dissipatively-formed flattened inner halo. Clearly, in many respects our inner-halo population is essentially kinematically identical to "the halo" population studied by Chiba & Beers (2000), and many others.

11.1.4. *Maximum Likelihood Analysis of Thick-Disk-Component Kinematics*

The mean rotational velocity and dispersion of the thick disk were then considered, based on inspection of a metal-rich ($-0.8 < $ [Fe/H] < -0.6) sub-sample of stars close to the Galactic plane. We obtained values of $\langle V_\phi \rangle = 182 \pm 2$ km s^{-1} and $\sigma_{V_\phi} = 57 \pm 1$ km s^{-1} ($\sigma_{V_\phi} = 51 \pm 1$ km s^{-1} when corrected for observational errors) for stars in the range $1 < |Z| < 2$ kpc, where the thick disk is expected to dominate, and contamination from thin-disk stars should be negligible. The gradient in asymmetric drift of the thick-disk component as a function of height above the plane, noted by previous authors, is very clear in our data as well; we derived $\triangle \langle V_\phi \rangle / \triangle |Z| = -36 \pm 1$ km s^{-1} kpc^{-1}, in excellent agreement with the rotational velocity gradients for disk stars obtained by Chiba & Beers (2000), Girard et al. (2006), Sheffield et al. (2007), and Ivezić et al. (2008). The disperson of this population also increases with distance, although it is not clear how much this might be influenced by overlap with metal-rich stars from the inner-halo component. Several authors have argued that this gradient in the asymmetric drift of the thick disk is consistent with heating of an early disk by satellite merger(s) (Quinn, Hernquist, & Fullagar 1993; Mihos et al. 1995; Robin et al. 1996; Walker, Mihos, & Hernquist 1996; Velázquez & White 1999; Aguerri, Balcells, & Peletier 2001; Chen et al. 2001; Hayashi & Chiba 2006).

11.1.5. *Fractions of Galactic Components From the ML Analyses*

The ML approach was then applied to the full range of metallicities in our sample of local calibration stars, in order to determine the fractional contribution of the three primary components in our model as a function of Z_{max} (fixing as inputs the values of mean rotational velocities and dispersions derived previously for each component). This exercise indicated that, within 5 kpc from the plane, the thick-disk and inner-halo components contribute roughly equally. Beyond 5 kpc the thick-disk component is absent, as expected. The inner-halo population dominates between 5 and 10 kpc. Beyond 10 kpc the outer halo increases in importance, is present in equal proportion to the inner halo between 15 and 20 kpc, and dominates beyond 20 kpc. The inversion point in the dominance of the inner/outer halo is located in the range Z_{max} = 15-20 kpc.

11.1.6. *Tests for an Independent MWTD Component*

We then used our extensive local dataset to examine the question of whether an independent MWTD component is required in order to account for the rotational properties of stars close to the Galactic plane. We selected sub-samples of stars in three metallicity regions, (*i*) $-2.0 <$ [Fe/H] < -1.5, (*ii*) $-1.5 <$ [Fe/H] < -1.0, and (*iii*) $-1.0 <$ [Fe/H] < -0.6, and two intervals of distance from the plane, $1 < |Z| < 2$ kpc, and $2 < |Z| < 4$ kpc. The clustering analysis approach was applied to each sub-sample, and used to demonstrate that, in the region closer to the Galactic plane, an independent MWTD component with $\langle V_\phi \rangle$ = 100-150 km s^{-1} and σ_{V_ϕ} = 40-50 km s^{-1} (35-45, km s^{-1}, when corrected for the observational errors), is required in order to account for the rotational behavior of the stars in our local sample. Similarly, an independent MWTD component must also exist in the interval farther from the Galactic plane, in order to accommodate the observed rotational behavior of the local sample of stars in that region of |Z|. It is interesting to note that the contribution of the MWTD component dominates over that of the inner-halo component for stars in the most metal-rich metallicity interval considered, not only close to the Galactic plane, but in the more distant interval as well. A population of rapidly rotating stars was identified in the metal-rich sub-sample, in both the nearby and more distant interval, which is deserving of further study.

Although superposition of the inner-halo and thick-disk MDFs and selection biases in the sample of local calibration stars preclude a determination of the MDF for the MWTD based on these data, we were able to demonstrate that the metallicity range covered by the MWTD is $-1.8 <$ [Fe/H] < -0.8 ($\langle$[Fe/H]$\rangle \sim -1.3$), and possibly up to [Fe/H] ~ -0.7.

The net rotational lag for the stars we identify with the MWTD ($\langle V_{lag} \rangle \sim 95$ km s^{-1}) is quite different with respect to the canonical thick-disk lag (~ 20 km s^{-1}: Chiba & Beers 2000; 51 km s^{-1}: Soubiran, Bienaymé, & Siebert 2003; ~ 38 km s^{-1}: this paper). The results obtained with the mixture-modeling analysis suggest that, if the MWTD is considered an independent stellar component of the Galaxy, its most likely mean rotational velocity and dispersion are $\langle V_\phi \rangle \sim 100$-150 km s^{-1} ($\langle V_{lag} \rangle \sim 70 - 120$ km s^{-1}), and $\sigma_{V_\phi} \sim 40$-50 km s^{-1} (σ_{V_ϕ} = 35-45 km s^{-1} when corrected for observational errors). It may be of interest that the value for the MWTD lag obtained from our analysis is in good agreement with that derived for the putative population of satellite debris found by Gilmore, Wyse, & Norris (2002), who obtained a lag in the mean azimuthal streaming motion of ~ 100 km s^{-1} behind the Sun. Note that the reported Gilmore et al. dispersion, on the order of 70 km s^{-1}, is slightly higher than ours, but this might be readily explained by contamination from inner-halo stars. These authors argued that such parameters might well be associated with stellar debris from a past merger event.

Of even greater interest is the possible connection between the MWTD stellar component and the Monoceros stream. Indeed, as reported by Yanny et al. (2003), the systemic Galactocentric rotational velocity of the stream is $\sim 110 \pm 25$ km s-1, which is in very good agreement with the mean value of V$_\phi$ derived for the MWTD component ($\sim 125 \pm 4$ km s-1). In addition, the estimated mean value of the Monoceros stream metallicity is [Fe/H] = -1.3 (Wilhelm et al. 2005), in agreement with the mean value of metallicity of

the MWTD reported above.[16] The similarity in rotational velocity and metallicity between the MWTD and the Monoceros stream requires further investigation, and will be carried out in the near future. Our analysis also indicated that the kinematic properties of the MWTD may change with height above the plane, as was already demonstrated for the thick-disk component, but superposition with inner-halo stars confounded a definitive determination. In any event, the preponderance of evidence suggests that the MWTD population may indeed be a kinematically and chemically distinct population from the canonical thick-disk population. We plan to address this issue in more detail in future investigations, through the use of stellar samples that are more suitable for analysis of the complexity of the thick-disk structure.

11.1.7. *Velocity Ellipsoids*

We next derived estimates of the velocity ellipsoids for the thick disk, inner halo, and outer halo; an approximate ellipsoid for the MWTD was also derived.

In the case of the thick-disk and outer-halo components, we examined the same sub-samples of stars used for determination of the rotational properties of these components. The inner-halo velocity ellipsoid component in the rotational direction was obtained from the ML analysis by holding the values of the rotational velocities and dispersions fixed for the thick-disk and outer-halo components. In the radial and vertical directions (where the strong overlap with multiple additional components complicates a mixture-model analysis), the velocities and dispersions were obtained adopting the mean velocity and dispersion of a sub-sample of stars in a more restricted range of metallicity ($-2.0 <$ [Fe/H] < -1.5), where the inner halo is expected to be dominant.

Our derived ellipsoid for the rapidly rotating canonical thick disk is (σ_{V_R}, σ_{V_ϕ}, σ_{V_Z}) = (53 ± 2, 51 ± 1, 35 ± 1) km s^{-1}, after correction of the derived dispersions for measurement errors. These values closely match the thick-disk velocity ellipsoid obtained by Chiba & Beers (2000). For the outer halo, which exhibits a large net retrograde rotation, we obtained (σ_{V_R}, σ_{V_ϕ}, σ_{V_Z}) = (159 ± 4, 165 ± 9, 116 ± 3) km s^{-1}, corrected for measurement errors. These values are consistent with a more tangentially anisotropic velocity ellipsoid, which was previously advocated by Sommer-Larsen et al. (1997), from an analysis of radial velocities of distant horizontal-branch stars.

The inner halo is essentially non-rotating, with a derived mean value of $\langle V_\phi \rangle = 7 \pm 4$ km s^{-1}, and a velocity ellipsoid (σ_{V_R}, σ_{V_ϕ}, σ_{V_Z}) = (150 ± 2, 95 ± 2, 85 ± 1) km s^{-1}, corrected for measurement errors. Although our zero mean rotational velocity differs from that reported by Chiba & Beers (2000), $\langle V_\phi \rangle \sim 30$-50 km s^{-1}, our velocity ellipsoid values are consistent, within the reported errors, with the Chiba & Beers determinations of a radially anisotropic ellipsoid, (σ_{V_R}, σ_{V_ϕ}, σ_{V_Z}) = (141 ± 11, 106 ± 9, 94 ± 8) km s^{-1}). This agreement obtains even though the Chiba & Beers analysis adopted a one-component halo, from which we conclude that their sample (and others) did not include significant numbers of outer-halo stars.

Our results can also be compared with the recent analysis of SDSS subdwarfs by Smith et al. (2009). These authors

---

[16] Note, however, that the mean photometric metallicity estimate of the Monoceros stream reported by Ivezić et al. (2008) is somewhat higher, [Fe/H] = -0.95)

obtained full space motions for a local sample of some 1800 subdwarfs selected on the basis of a reduced proper motion diagram, and used the same spectroscopic determinations of stellar atmospheric parameters as the present work. Note that for the purpose of their analysis they considered the halo as a single entity. They concur with our determination that the inner halo exhibits essentially no net rotation (they obtained $\langle V_\phi \rangle = 1 \pm 2$ km s^{-1}), but reported a slightly different derived velocity ellipsoid. Their values $(\sigma_{V_R}, \sigma_{V_\phi}, \sigma_{V_Z}) = (137 \pm 2, 81 \pm 1, 89 \pm 1)$ km s^{-1}, agree with our determination for the vertical component of the inner halo ellipsoid, but are 15-20 km s^{-1} lower than our determinations for the radial and azimuthal components. Similarly, the values for the (single-component) halo velocity ellipsoid obtained by Bond et al. (2009), from an analysis of the space motions for some 100000 main-sequence stars from SDSS/SEGUE with available spectroscopy, $(\sigma_{V_R}, \sigma_{V_\phi}, \sigma_{V_Z}) = (135 \pm 5, 85 \pm 5, 85 \pm 5)$ km s^{-1}, although in agreement with the Smith et al. ellipsoid, also differ from our results for the radial and azimuthal components.

We suspect that the resolution of these differences may be the presence of a significant MWTD component. The lower velocity dispersion of such a component, if unrecognized, may have an impact on the derived halo velocity ellipsoids. In this regard, it may be of significance that Smith et al. noted that their observed distribution of V_ϕ exhibited a significant asymmetry; their attempted decomposition of the distribution with a two-component model yielded estimates for the dispersions of 47 and 99 km s^{-1}, values reminiscent of what we would associate with the MWTD and inner-halo populations, respectively (although the mean rotational velocity they obtained for the component with a MWTD-like dispersion was only 17 km s^{-1}). They also pointed out that the asymmetry of their V_ϕ distribution increased for stars with [Fe/H] > -1.5, consistent with this interpretation.

We have attempted to estimate the other two components (the radial and vertical components) of the velocity ellipsoid for the MWTD. Application of a mixture-model analysis, for the range of metallicity $-1.5 <$ [Fe/H] < -1.0 and distance interval $1 < |Z| < 2$ kpc, indicates slightly negative velocities in the radial and vertical directions, $\langle V_R \rangle = -13 \pm 5$ km s^{-1}, and $\langle V_Z \rangle = -14 \pm 5$ km s^{-1}, respectively. When combined with the previously estimated value for the rotational velocity dispersion of the MWTD, the velocity ellipsoid for the MWTD is $(\sigma_{V_R}, \sigma_{V_\phi}, \sigma_{V_Z}) = (59 \pm 5, 40 \pm 3, 44 \pm 2$ km s$^{-1})$. Note that, for the rotational direction, we have adopted a value for the dispersion midway between the extremes obtained from the mixture-model analysis of different metallicity regions and distance intervals. The velocity asymmetries in the radial and vertical directions could indicate that stars in the MWTD component may not be on circular orbits nor have orbits that are co-planar with the orbits of stars associated with the thin-disk component. This could be another sign that the MWTD might be associated with stars from the Monoceros stream, as mentioned above.

We also demonstrated that all three components of the velocity dispersions increase with decreasing metallicity, in a manner suggesting discontinuous transitions from the thick disk to the MWTD, and from the inner to the outer halo. This is a fundamental new result (also reported by Bond et al. 2009), which can be used to place constraints on possible formation scenarios for the stellar components of the Milky Way by comparison with new-generation numerical simulations.

11.1.8. *Thick-Disk System Scale Lengths and Heights*

Our extensive data set for the disk systems has also been used to obtain kinematic estimates of the thick-disk scale length and scale height. In our form of the Jeans Equation, separated into radial and vertical components, we have included the gradients in σ_{V_R} and σ_{V_Z}, which are directly measured from the data. We found that the vertical acceleration, K_Z, obtained by Kuijken & Gilmore (1991) is in optimal agreement with the value independently determined by Holmberg & Flynn (2000). Adopting the dispersion for the thick disk reported in Table 5, a mean rotational velocity, $\langle V_\phi \rangle = 182$ km s^{-1}, and K_Z at 1.1 kpc, we found a scale length, $h_R = 2.20 \pm 0.35$ kpc, and a scale height, $h_Z = 0.51 \pm 0.04$ kpc. The smaller value of our scale length with respect to that of Chiba & Beers (2000) (4.5 kpc) results from our mean rotational velocity of the thick disk, which is significantly smaller than theirs. However, our estimate of h_R is in agreement with that of others, based on star counts (Reylé & Robin 2001).

A large range of thick-disk scale heights has been reported in the literature – from 0.6 kpc to 1 kpc (Gilmore & Wyse 1985; Kuijken & Gilmore 1989; Robin et al. 1996; Norris 1996; Ng et al. 1997; Buser et al. 1999; Chen et al. 2001; Kerber et al. 2001; Ojha 2001; Reylé & Robin 2001; Du et al. 2003; Larsen & Humphreys 2003; Du et al. 2006), and from 1.1 kpc to 1.6 kpc (Gilmore & Reid 1983; Robin & Crezé 1986; Spagna et al. 1996; Buser et al. 1998). Our kinematic evaluation of h_Z falls at the lower end of these estimates. A possible explanation might be the derived velocity dispersion in the vertical direction for the thick disk (35 km s^{-1}), which could be reduced by the presence of thin-disk stars in the selected sub-sample. The gradient of σ_{V_Z} does not contribute significantly in the Jeans Equation; even when an isothermal thick disk is considered ($\partial \sigma_{V_Z}/\partial |Z| = 0$), we obtain $h_Z = 0.64$ kpc. Note that our estimate of the scale height is made at $|Z| = 1.1$ kpc, while the "usually larger" estimates come from star counts at $|Z| \sim 2$ to 4 kpc (see references above). In these works, the thick disk appears as vertically exponential at larger $|Z|$, but in fact, it is unlikely to be strictly exponential. If we consider the general version of the Jeans Equation, and perform a numerical integration under the assumption that the thick disk is vertically isothermal, with a velocity dispersion of $\sigma_{V_Z} = 35$ km s^{-1}, we find that at $|Z| = 1.1$ kpc, the "local scale height" is in perfect agreement with our value of 0.64 kpc. On the other hand, if we define an effective scale height of the thick disk as the height above the Galactic plane at which the density decreases by a factor e from its value at $|Z| = 0$, we find that this height is 0.99 ± 0.04 kpc, which is not directly comparable with the star count scale heights at larger $|Z|$.

In the case of the MWTD, we have only the kinematic parameters listed in Table 5 (i.e., no directly measured gradients could be obtained), which can be used to derive important constraints on the radial structure of this component. Indeed, using the radial component of the Jeans Equation, and assuming that $\sigma_{V_R}^2 \propto exp(-R/h_\sigma)$, where h_σ is a scale length, we find that the MWTD scale length is again short, ~ 2 kpc. This result comes from the assumption that the MWTD presents a uniform scale height and constant anisotropy. The scale height has been derived adopting the same value of the vertical acceleration reported above, and under the same assump-

tions. We obtained $h_Z = 1.36 \pm 0.13$ kpc, in agreement with the larger values of the scale height estimation of the canonical thick disk.

11.1.9. *Inferred Density Profiles of the Inner-and Outer-Halo Components*

The kinematics for our local sample of calibration stars were used to infer density profiles for the inner-halo and outer-halo components. We obtained $\rho_{in} \sim r^{-3.17 \pm 0.20}$ for the inner halo, consistent with the derived density profile of "the halo" found by many previous authors (e.g., Harris 1976; Zinn 1985; Hartwick 1987; Carney, Latham, & Laird 1990; Preston at al. 1991; Chiba & Beers 2000). In contrast, the density profile obtained for the outer halo, $\rho_{out} \sim r^{-1.79 \pm 0.29}$, is substantially shallower than that of the inner halo, as expected from the higher values of the velocity dispersions for this component. It is thus of interest to note that Ivezić et al. (2000), based on a sample of RR Lyraes located between 10 and 50 kpc from the Galactic center selected from SDSS commisioning data, obtained a slope of -2.7 ± 0.2. From the QUEST RR Lyrae Data (which cover basically the same distance range as the Ivezić et al. sample), Vivas & Zinn (2006) obtained values for the derived slope between -2.5 ± 0.1 and -3.1 ± 0.1, depending on the adopted level of flattening and local density. Our low value of the slope for the outer-halo component is reminiscent to that obtained by Miceli et al. (2008) for Oosterhoff Type II RR Lyraes (-2.88 ± 0.11; the value for Oosterhoff Type I class is even smaller, -2.26 ± 0.07). Note that both of these values assumed a spherical halo, and included stars only up to about 30 kpc away. When a flattened halo is considered, the Miceli et al. slope changes from -2.43 ± 0.06 (all RR Lyrae types, spherical halo) to -3.15 ± 0.07. Sesar et al. (2009) report a dramatic "steepening" of the halo density profile beyond 30 kpc, based on an analysis of RR Lyraes and main-sequence stars from the SDSS equatorial stripe, in the sense that the numbers of stars at large Galactocentric distances is much lower than would be expected from extrapolation of the (single halo component) density profile they adopt to describe the density profile within 30 kpc. Alternatively, this result could be interpreted as arising from the changeover from inner-halo to outer-halo dominance in the star counts, with the outer-halo contributing substantially fewer stars beyond 30 kpc (we roughly estimate that the local relative normalization of outer-halo to inner-halo spatial density laws is about 10%). Thus, although differences in the precise values of the slopes obtained from different data sets and different analysis approaches remain, it appears that the inner/outer halo model very naturally accounts for observed changes in the density profile of halo tracers with distance reported by a number of previous groups.

11.1.10. *Derived Tilts of the Velocity Ellipsoids*

The kinematic parameters derived for stars in our local sample have been used to examine tilts of the velocity ellipsoids, as a function of height above the Galactic plane, over several intervals in metallicity.

Misalignment of the velocity ellipsoids with the adopted cylindrical coordinate system has been found for all the selected sub-samples. At high metallicity the tilt angle is $7°.1 \pm 1°.5$, when $1 < |Z| < 2$ kpc, and $5°.5 \pm 1°.2$ at $2 < |Z| < 4$ kpc. A similar value was reported by Siebert et al. (2008) for a sample of RAVE-survey stars at $|Z| < 1$ kpc ($7°.3 \pm 1°.8$). At intermediate metallicity the tilt angle is $10°.3 \pm 0°.4$, and

$15°.1 \pm 0°.3$, while for low-metallicity stars we found $8°.6 \pm 0°.5$, and $13°.1 \pm 0°.4$, at $1 < |Z| < 2$ kpc and $< |Z| < 4$ kpc, respectively. The velocity ellipsoids point close to the Galactic center, as can be inferred from Figure 19. Bond et al. (2009) also report similar tilts of the velocity ellipsoid for low-metallicity stars. The existence of these tilts indicates that motions of stars in our local sample are aligned with respect to a spherical, rather than cylindrical, coordinate system.

We considered the possibility that the inner halo and/or outer halo might exhibit kinematics close to isotropic in (θ, ϕ), which would be consistent with a system for which the distribution function depends on the energy and the total angular momentum. For a sample of stars with $-2.0 < $ [Fe/H] -1.6, and located at $2 < |Z| < 4$ kpc, where the dominant component is expected to be the inner halo, we find $(\sigma_{V_r}, \sigma_{V_\phi}, \sigma_{V_\theta}) = (160 \pm 3, 102 \pm 2, 83 \pm 2)$ km s^{-1}. These values are somewhat higher than those recently obtained by Smith et al. 2009 $(142, 81, 77)$ km s^{-1}, and Bond et al. (2009) $(141, 85, 75)$ km s^{-1}. In the case of the outer halo, a similar estimate is more uncertain, due to the difficulty in separating the two halo components in V_ϕ and V_Z. Nevertheless, an attempt was made, employing the interval of metallicity [Fe/H] < -2.4 and $2 < |Z| < 4$ kpc, which should emphasize outer-halo stars. We obtained $(\sigma_{V_r}, \sigma_{V_\phi}, \sigma_{V_\theta}) = (178 \pm 9, 149 \pm 7, 127 \pm 6)$. The conclusion of this exercise is that both the inner and outer halo are significantly anisotropic in (θ, ϕ).

11.1.11. *Variation of the Observed Metallicity Distribution Function with Distance from the Galactic Plane*

Finally, we examined the "as observed" MDF using the full sample of calibration stars, to look for confirmation of the expected changes as a function of the height above the plane (Fig. 20). We constructed MDFs at different intervals of $|Z|$, close to the Galactic plane ($0 < |Z| < 5$ kpc), and farther from the Galactic plane ($5 < |Z| < 9$ kpc, and $|Z| > 9$ kpc). In the first case, the MDF exhibits a transition from a thick-disk and MWTD-dominated population to an inner-halo dominated population, while in the second case, there is clear evidence for a transition from inner-halo to outer-halo dominance.

11.1.12. *Comparison with the Results of Bond et al. (2009)*

The recent analysis conducted by Bond et al. (2009) considered the kinematics of a larger sample of SDSS stars than the present investigation, based on both photometric and spectroscopic metallicity estimates. Although the analysis techniques and the adopted models differ somewhat from those used herein, the basic conclusions of these two studies are very similar. We point out that the Bond et al. approach was not able to effectively split an assumed single-halo population into inner- and outer-halo components, since the metallicities of outer-halo stars are lower than can be usefully assigned abundances from photometric techniques. Nevertheless, one can see the presence of stars with retrograde velocities in the lower-right panel of Figure 6 of Bond et al. (stars selected with $|Z|$ in the range 5-7 kpc) as an "excess" population relative to their assumed single-halo population (note that in Bond et al., the rotational velocities are assigned an opposite sign than in the present work; we are referring to stars in their figure with $V_\phi > 250$ km s^{-1}). Similarly, again from inspection of the same panel in their Figure 6, essentially all of their data points with positive (meaning retrograde) rotational velocities fall *under* their single-Gaussian fit, while those with negative

(meaning prograde) velocities in the range $-150 < V_\phi < 0$ km s^{-1} fall *above* their single-Gaussian fit. This apparent lack of fit is almost certainly due to the lack of an inner/outer split in their model of the halo population. Nevertheless, due to the relatively small number of outer halo stars at the distance limit of their sample (7 kpc), the derived kinematics of their "halo population" are quite similar to our inner-halo population.

The results of these two studies for the thick-disk populations, although approached in a different way, are also compatible. In the Bond et al. approach, the disk stars in their sample were modeled with a non-Gaussian distribution for the rotational velocities, incorporating a component with a fixed lag in velocity relative to what we would consider the canonical thick disk. We would identify this lower rotational velocity component with the MWTD of our analysis. It is interesting that they found that this model was able to accommodate the observed behavior of their sample smoothly with increasing height above the Galactic plane. Clearly, there remains more to be learned from future analysis of these data.

11.2. *Discussion*

The structural and kinematic parameters obtained in this paper provide valuable information for understanding the formation of the stellar halos and thick disks of the Milky Way. We have confirmed that the inner- and the outer-halo components exhibit different kinematic properties and inferred spatial distributions, and (from the previous analysis of the DR5 sample of calibration stars by Carollo et al. 2007, and confirmed by our *in-situ* analysis of the the full calibration-star sample) that their metallicity distribution functions differ significantly as well. We have also confirmed the presence of a significant vertical gradient in $\langle V_\phi \rangle$ as a function of $|Z|$ at low abundances, which suggests that the inner-halo component was most likely formed by dissipational processes.

A number of recent theoretical and observational efforts provide supporting evidence for the existence of an inner/outer halo dichotomy in the Milky Way, and in other similar galaxies. We consider these in turn.

11.2.1. *The Halos: Evidence from Theoretical Modeling*

De Lucia & Helmi (2008) have adapted a high-resolution simulation of a Milky Way-like halo, combined with a semi-analytic approach, to explore the formation of the Galaxy. They found *no evidence* for a "continuous" metallicity gradient for halo stars, but rather, evidence for a strong concentration of higher-metallicity halo stars toward the Galactic center, and the presence of lower-metallicity stars at distances beyond 20 kpc from the Galactic center. The results of this simulation bear a strong resemblance to the properties of the dominant inner halo we find within 10-15 kpc from Sun, as well as with its rather steep inferred density profile, and an outer halo that dominates beyond 15-20 kpc, with a much shallower inferred density profile.

In a recent paper, Zolotov et al. (2009) have investigated the formation of the stellar halos in simulated disk galaxies, using high-resolution SPH + N-Body simulations. They found that the inner regions (r < 20 kpc) contain both accreted and *in-situ* stellar populations (the latter includes stars formed in the main halo). Contrasting with this, the outer regions of the simulated halos were assembled through pure accretion and the disruption of satellites.

Other recent supporting evidence is found in a simulation by Salvadori et al (2009). These authors studied the age and metallicity distribution function of metal-poor stars in the Milky Way halo, as a function of Galactocentric radius, from a study combining N-body simulations and semi-analytical methods. They found that the stellar distributions, within 50 kpc from the center of their simulated galaxy, follow a power-law in radius, r^n, where $n \sim -3.2$ for stars with $-2 \leq [\text{Fe/H}] \leq -1$, and $n \sim -2.2$ for stars with $[\text{Fe/H}] \leq -2$. In this context, the relative contribution of stars with $[\text{Fe/H}] \leq -2$ strongly increases with r (16% within $7 < r < 20$ kpc, up to $> 40\%$ for $r > 20$ kpc). Note that our spatial-density power laws for the inner and outer halo are in reasonable agreement, within the errors, with the values found by Salvadori et al (2009).

Cooper et al. (2009) have also conducted simulations of the formation of stellar halos within the ΛCDM paradigm, offering a number of improvements over previous efforts. Their results, which cover a range of possible halo formation histories, produce predicted metallicity shifts at various radii, several of which are reminiscent of what we have found in our own analysis of the Milky Way's halo system. It is notable that, in all cases, the lowest metallicity stars in their simulations are accreted (or stripped) from the very sort of ultra-faint dwarf galaxies that Carollo et al. (2007) suggested may be related to the origin of the outer-halo population.

11.2.2. *The Halos: Evidence from Observations of Other Galaxies*

For at least a decade, the mystery of the relatively "metal-rich" halo of M 31 has presented a challenge to our understanding of its formation history. Photometric and spectroscopic observations by Kalirai et al. (2006b), and more recently by Koch et al. (2008a), have demonstrated that a metal-poor halo of M 31 does exist, but is located beyond 40 kpc from its center (substantially different than observed for the Milky Way, where the outer halo becomes dominant beyond 20 kpc). Their description of a dual-halo model for the Andromeda Galaxy parallels what we observe for the Milky Way, albeit on different length scales.

Recent observations of the Milky Way analogue NGC 891 have provided additional information on the structure and the stellar populations for this relatively massive spiral galaxy in the NGC 1023 group (Ibata, Mouhcine, & Rejkuba 2009; Rejkuba, Houhcine, & Ibata 2009). Analysis of their data revealed the presence of a thick-disk structure with vertical scale height $h_Z = 1.4$ kpc, and scale length $h_R = 4.8$ kpc, somewhat larger than values that have been inferred for the Milky Way. The MDF of the thick-disk structure exhibits a peak at $[\text{Fe/H}] \sim -0.9$ (as compared to $[\text{Fe/H}] \sim -0.6$ for the canonical thick disk of the Milky Way) that does not change significantly in the vertical and radial directions. When they considered the MDF for stars in regions resembling the solar cylinder we have examined in the present paper (distance along the major axis ~ 8 kpc, vertical distance intervals of ~ 3-4 kpc and 5-7 kpc), they detected a substantial population of intermediate-metallicity stars, with $[\text{Fe/H}] \sim -1.0$. By way of contrast, at these same vertical distances the MDF of the Milky Way is dominated by the inner halo ($[\text{Fe/H}] \sim -1.6$; Ivezić et al. 2008; this paper). The intermediate-metallicity population in the solar cylinder of NGC 891 might be associated with a component similar to the Milky Way's MWTD, but are present at larger distances from the plane in this galaxy than in the Milky Way. The difference between the verticle extension and MDF of the disk populations between NGC 891 and the Milky Way may simply reflect different (stochastic) formation histories for the two galaxies.

The stellar halo of NGC 891 exhibits a shallow metallicity gradient, with average metallicity decreasing from [Fe/H] = −1.15 to −1.27 from the inner regions to the outskirts. A similar trend was also found in the inner halo of M 31 (20 kpc from the nucleus; Durrell, Harris, & Pritchet 2001), and in the halo of NGC 5128, which is the nearest giant elliptical galaxy (Rejkuba et al. 2005). In subsequent work, metal-poor halos were detected for these galaxies, at distances larger than $12r_{eff}$ from the center (Chapman et al. 2006; Kalirai et al. 2006a; Harris et al. 2007). However, in NGC 891, at the same radius, a metal-poor halo has not (yet) been detected. In this regard we note that in the right-hand panel of Figure 18 in Rejkuba et al. (2009) there is a clear transition of the MDF, from intermediate ([Fe/H] $\sim$ −1.0) metallicity to a lower ([Fe/H] $\sim$ −1.5) metallicity, which suggests the presence of a metal-poor population like that in the inner halo of the Milky Way. We suspect that when additional photometry at larger distances is carried out for NGC 891 its MDF will reveal metal-poor halo population(s) similar to those of the Milky Way.

Recent spectroscopic studies of the metallicities and other elemental abundances in the ultra-faint dSph galaxies (Kirby et al. 2008; Koch et al. 2008b; Norris et al. 2008; Frebel et al. 2009) have clearly demonstrated that the frequently cited result (e.g., Helmi et al 2006) that "the progenitors of nearby dSph's appear to have been different from the building blocks of the Milky Way," while true for the more luminous members of the dSph population, does not necessarily pertain to its fainter systems. While we refer the reader to the reviews of Koch (2009) and Tolstoy, Hill, & Tosi (2009) for more thorough discussions, we note here two relevant points. First, it has been shown that the metallicities of stars in even the more luminous dSphs (e.g., Sculptor; Battaglia et al. 2008) are spatially stratified, with the more metal-poor objects being found preferentially in their outer regions. These metal-poor stars are clearly the most likely to be stripped from their parents during tidal interactions, with the halo(s) of the Milky Way as the obvious recipients. Secondly, the works cited above establish that extremely metal-poor stars ([Fe/H] < −3.0) exist in the ultra-faint systems, and for [Fe/H] < −1.6, one finds [α/Fe] $\sim$ 0.3–0.5, similar to Galactic halo values. It is not difficult to imagine a substantial population of low-luminosity dwarfs, most of which have already been completely dissolved, accounting for the entire population of stars in the presently observed outer-halo component of the Milky Way. We look forward to further guidance for this idea to be obtained by additional high-resolution spectroscopic observations of stars in the low-luminosity dwarfs, as well as detailed elemental abundance determinations for stars with kinematics that suggest membership in the outer-halo population (e.g., Ishigaki et al. 2009; Roederer 2009; Zhang et al. 2009; Roederer et al., in preparation).

11.2.3. *The Thick Disk: Evidence from Theoretical Modeling*

Simulations that attempt to account for the formation of the thick-disk component have suggested that the asymmetric drift we find for this structure can be naturally accommodated. According to the simulations of Abadi et al. (2003), it may also be consistent with the expected behavior if the thick disk is comprised solely of debris from merging satellites. The formation of a MWTD component may be the result of a stochastic event, such as assimilation of the debris from a moderately metal-poor, low-mass satellite.

Modern cosmogonies predict the formation of the thick disk

by predominantly dissipationless processes. In this context, thick-disk stars were vertically heated from a pre-existent thin disk during a significant minor merger or perturbation by a cold dark matter sub-halo (Kazantzidis et al. 2009), or directly deposited at large scale heights as tidally stripped debris during the accretion of smaller satellite galaxies (e.g., Statler 1988; Abadi et al. 2003; Yoachim & Dalcanton 2008). Villalobos & Helmi (2008) have investigated in detail the heating process by a minor merger. They found that the trend of the ratio $\sigma_{V_Z}/\sigma_{V_R}$ with radius in the final disks is a good discriminant of the initial inclination of the merging satellite. For the Milky Way, the observed $\sigma_{V_Z}/\sigma_{V_R}$ is $\sim$ 0.6 (Chiba & Beers 2000; this paper), which suggest that the thick disk of the Galaxy could have been produced by a merger of intermediate inclination. The values found for the MWTD velocity ellipsoid provide a ratio $\sigma_{V_Z}/\sigma_{V_R} \sim$ 0.7, which could be explained through a merger of different inclination.

Hayashi & Chiba (2006) have shown that disk thickening, quantified by the change of its scale height (or the square of its vertical velocity dispersion), strongly depends on the individual mass of an interacting sub-halo. In this scenario of hierarchical formation, the MWTD could be formed through the early merger (at least with respect to the merger responsible for the formation of the canonical thick disk) of a satellite with a less massive, younger pre-existing disk. Note, however, that the existence of stars with disk kinematics and older than the last major merger event is difficult to accommodate in the ΛCDM scenario (Abadi et al. 2003). The results of the simulations of Abadi et al. suggest that the tidal debris from satellites can contribute not only to the Galactic halo, but also to the disk system. The contribution to the halo or to the disk depends on the orbit of the merging satellite, and on the degree to which dynamical friction circularized the orbits before disruption (Statler 1988). An accreted satellite that contributes significantly to the thick disk must be disrupted on an orbital plane very close to that of the disk, and be massive enough to survive the disruption until its orbit is circularized within the disk. In this scenario, the predicted location of the disrupted satellites responsible for the formation of the thick disk and MWTD is within the thick-disk system itself. We have noted in §11.1 that some properties of the Monoceros stream (rotational velocity and metallicity) are in good agreement with those of the MWTD. *The Monoceros stream could be part of the disrupted satellite that was also responsible for the formation of the thick-disk system.*

11.2.4. *The Metal-Weak Thick Disk: Additional Evidence Needed from Observations*

We have attempted to constrain the properties of the MWTD as an independent kinematic component from the canonical thick disk. It was found that its velocity lag is $\sim$ 60 km s^{-1} lower than the canonical thick disk; its velocity ellipsoid appears similar to that of the thick disk (although its vertical velocity dispersion, and hence its inferred scale height, appear somewhat larger). These values are, of course, still uncertain due to the significant kinematic and spatial overlap of the MWTD with the thick-disk and inner-halo components. Additional study (informed by more-detailed abundance analyses of likely MWTD stars) must be given to this problem before its final resolution can be obtained. Other sub-samples of stars from SDSS/SEGUE, beyond the calibration stars discussed in our study, as well as stars from other surveys such as RAVE, will help shed light on the nature of the Galactic components we have described. It is evident that the final ob-

servational picture has yet to be drawn; nuances continue to be revealed as our database of information expands. Witness the "highly flattened" inner-halo component suggested by Morrison et al. (2009) that comprises stars with intermediate low metallicities, and is confined to a region close to the Galactic plane, but (in contrast to the MWTD) is not supported by rotation.

Facilities: SDSS.

REFERENCES

Abadi, M.G., Navarro, J.F., Steinmetz, M., & Eke, V.R. 2003, ApJ, 597, 21
Abazajian, K., et al. 2009, ApJS, 182, 543
Adelman-McCarthy, J.K., et al. 2007, ApJS, 172, 634
Adelman-McCarthy, J.K., et al. 2008, ApJS, 175, 297
Aguerri, J.A.L., Balcells, M., & Peletier, R.F. 2001, A&A, 367, 428
Allen, C., Schuster, W.J., & Poveda, A. 1991, A&A, 244, 280
Allende Prieto, C., et al., 2008, AJ, 136, 2070
An, D., et al. 2009, ApJ, 707, L64
Batsleer, P., & Dejonghe. H., 1994, A&A, 287, 43
Battaglia, G., Helmi, A., Tolstoy, E., Irwin, M., Hill, V., & Jablonka, P. 2008, ApJ, 681, L13
Beers, T.C., & Sommer-Larsen, J. 1995, ApJS, 96, 175
Beers, T.C., et al. 2000, AJ, 119, 2866
Beers, T.C., et al. 2002, AJ, 124, 931
Bell, E.F., et al. 2008, ApJ, 680, 295
Belokurov, V., et al. 2006, ApJ, 642, L137
Bienayme, O. et al. 2009, A&A, 500, 801
Binney, J. & Tremaine, S., 1988, Galactic Dynamics (Princeton: Princeton Univ. Press)
Binney, J. & Tremaine, S., 2008, Galactic Dynamics 2nd edition (Princeton: Princeton Univ. Press)
Bond, N.A., et al. 2009, arXiv:0909.0013
Brown, W.R., Geller, M.J., Kenyon, S.J., & Diaferio, A. 2009, AJ, 139, 59
Buser, R., et al. 1998, A&A, 331, 934
Buser, R., Rong, J. & Karaali, S. 1999, A&A, 348, 98
Carney, B.W. 1984, PASP, 96, 841
Carney, B.W., Latham, D.W., & Laird, J.B. 1990, AJ, 99, 572
Carney, B.W., Laird, J.B., Latham, D.W., & Aguilar, L.A. 1996, AJ, 112, 668
Carollo, D., et al. 2007, Nature, 450, 1020
Chapman, S.C., et al. 2006, ApJ, 653, 255
Chen, B., et al. 2001, ApJ, 553, 184
Chiba, M., & Beers, T.C. 2000, AJ, 119, 2843
Chiba, M., & Beers, T. C., 2001, ApJ, 549, 325
Chiba, M., Yoshii, Y., & Beers, T.C. 1999, in The Third Stromlo Symposium: The Galactic Halo, ASP Conf. Ser. 165, eds. B.K. Gibson, T.S. Axelrod, & M.E. Putman, (San Francisco: ASP), p. 269
Cooper, A.P., et al., 2009, arXiv:0910.3211
Dejonghe, H., & de Zeeuw, P. T., 1988, ApJ, 333, 90
De Lucia, G. & Helmi, A., 2008, ApJ, 391, 14
Du et al. 2003, A&A, 407, 541
Du et al. 2006, MNRAS, 372, 1304
Durrell, P.R., Harris, W.E., & Pritchet, C.J. 2001, AJ, 121, 2557
Eggen, O.J., Lynden-Bell, D., & Sandage, A. R. 1962, ApJ, 136, 748
Frebel, A., Simon, J.D., Geha, M., & Willman, B. 2009, ApJ, 708, 560
Freeman, K.C. 1987, ARA&A, 25, 603
Ghez, A.M., et al., 2008, ApJ, 689, 1044
Gilmore, G., & Reid, N. 1983, MNRAS, 202, 1025
Gilmore, G. & Wyse, R.F.G. 1985, AJ, 90, 2015
Gilmore, G., Wyse, R.F.G., & Norris, J.E. 2002, ApJ, 574, 39
Girard, T. M., Korchagin, V.I., Casetti-Dinescu, D.I., van Altena, W.F., Lopez, C.E., & Monet, D.G. 2006, AJ, 132, 1768
Grillmair, C.J., 2006, ApJ, 651L, 29
Grillmair, C.J., Carlin, J.L., & Majewski, S.R. 2008, ApJ, 689, L117
Gunn, J.E., et al., 2006, AJ, 131, 2332
Harris, W.E. 1976, AJ, 81, 1095
Harris, W.E., Harris, G.L.H., Layden, A.C., & Wehner, E.M.H. 2007, ApJ, 666, 903
Hartwick, F.D.A. 1987, in The Galaxy, NATO ESI Ser. 207, eds. G. Gilmore & B. Carswell, (Dordrecht: Reidel), p. 281
Hayashi, H., & Chiba, M., 2006, PASJ, 58, 835
Helmi, A., et al., 2006, ApJ, 651, L121
Holmberg, J. & Flynn, C. 2000, MNRAS, 313, 209
Ibata, R., Mouhcine, M., & Rejkuba, M. 2009, MNRAS, 395, 126
Ishigaki, M., Chiba, M., & Aoki, W. 2009, PASJ, in press (arXiv:0912.0329)
Ivezić, Ž., et al. 2000, AJ, 120, 963
Ivezić, Ž., et al. 2008, ApJ, 684, 287
Jones, B.F., & Walker M.F. 1988, AJ, 95, 1775
Kalirai, J.S., et al. 2006a, ApJ, 641, 268
Kalirai, J.S., et al. 2006b, ApJ, 648, 389
Katz, D., et al. 1999, Ap&SS, 265, 221
Kaufman, L., & Roesseeuw, P.J. 1990, Finding Groups in Data. An Introduction to Cluster Analysis, (New York: Wiley)
Kazantzidis, S., Zentner, A.R., Kravtsov, A.V., Bullock, J.S., & Debattista, V.P. 2009, ApJ, 700, 1896
Kerber, L.O., et al. 2001, A&A, 345, 424
Kerr, F.J., & Lynden-Bell, D. 1986, MNRAS, 221, 1023
Kinman, T.D., Suntzeff, N.B., & Kraft, R.P. 1994, AJ, 108, 1722
Kinman, T.D., Cacciari, C., Bragaglia, A., Buzzoni, A., & Spagna, A. 2007, MNRAS, 371, 1381
Kirby, E., et al. 2008, AJ, 685, L43
Klement, R., et al. 2009, ApJ, 698, 865
Koch, A. 2009, Rev. Mod. Astron., 21, 9
Koch, A., et al., 2008a, ApJ, 689, 958
Koch, A., et al., 2008b, ApJ, 688, L13
Koposov, S.E., Rix, H.-W., & Hogg, D.W. 2009, ApJ, submitted (arXiv:0907.1085)
Kuijken, K. & Gilmore, G. 1989, MNRAS, 239, 605
Kuijken, K. & Gilmore, G. 1991, ApJ, 367, L9
Larsen, J.A. & Humphreys, R.M 2003, AJ, 125, 1958
Layden, A.C. 1995, AJ, 110, 2288
Lee, Y.S., & Beers, T.C. (2009), BAAS, 41, 227
Lee, Y.S., et al. 2008a, AJ, 136, 2022

Lee, Y.S., et al., 2008b, AJ, 136, 2050
Lee, Y.W., Gim, H.B., & Casetti-Dinescu, D.I. 2007, AJ, 661, L49
Lupton, R.L., 1993, Statistics in Theory and Practice (Princeton: Princeton Univ. Press)
Majewski, S.R., 1992, ApJS, 78, 87
Martin, J.C., & Morrison, H.L. 1998, AJ, 116, 1724
Miceli, A., et al. 2008, ApJ, 678, 865
Mihalas, D., & Binney, J. 1981, Galactic Astronomy (San Francisco: Freeman)
Mihos, J.C., Walker, I.R., Hernquist, L., Mendes de Oliveira, C., & Bolte, M. 1995, ApJ, L87
Morrison, H.L., Flynn, C., & Freeman, K.C. 1990, AJ, 100, 1191
Morrison, H.L., et al. 2009, ApJ, 694, 130
Munn, J.A., et al. 2004, AJ, 127, 3034
Munn, J.A., et al. 2008, AJ, 136, 895
Ng, Y.K., et al. 1997, A&A, 324, 65
Norris, J., Bessell, M.S., & Pickles, A.J. 1985, ApJS, 58, 463
Norris, J.E. 1994, ApJ, 431, 635
Norris, J.E. 1996, in Formation of the Galactic Halo, Inside and Out, ASP Conf. Ser. 92, eds. M. Morrison & A. Sarajedini, (San Francisco: ASP), p. 14
Norris, J.E., et al. 2008, ApJ, 689, L113
Ojha, K. K., 2001, MNRAS, 322, 426
Press, W.G., Flannery, B.P., Teukolsky, S.A., & Vetterling, W.T. 1992, Numerical Recipes in C: The Art of Scientific Computing (Second Edition), (Cambridge: Cambridge Univ. Press)
Preston, G.W., Shectman, S.A., & Beers, T.C. 1991, ApJ, 375, 121
Quinn, P.J. & Goodman, J. 1986, ApJ, 309, 472
Quinn, P.J., Hernquist, L., & Fullagar, D.P. 1993, ApJ, 403, 74
Reddy, B.E., & Lambert, D.L. 2008, MNRAS, 391, 95
Rejkuba, M., Greggio, L., Harris, W.E., Harris, G.L.H., & Peng, E.W. 2005, ApJ631, 262
Rejkuba, M., Mouhcine, M., & Ibata, R. 2009, MNRAS, 396, 1231
Reylé, C., & Robin, A.C. 2001, A&A, 373, 886
Robin, A. & Creze, M. 1986, A&A, 64, 53
Robin, A.C., Haywood, M., Creze, M., Ojha, D.K., & Bienayme, O. 1996, A&A, 305, 125
Rodgers, A.W., & Roberts, W.H. 1993, AJ, 106, 6
Roederer, I. 2009, AJ, 137, 272
Ryan, S.G., & Norris, J.E. 1991, AJ, 101, 1835
Ryan, S.G., & Lambert, D.L. 1995, AJ, 109, 2068
Salvadori, S., Ferrara, A., Schneider, R., Scannnapieco, E., & Kawata, D. 2009, MNRAS, 401, L5

Sandage, A., & Fouts, G. 1987, AJ, 93, 74
Schlaufman, K.C., et al. 2009, ApJ, 703, 2177
Schlegel, D.J, Finkbeiner, D.P., & Davis, M. 1998, ApJ, 500, 525
Schoenrich, R. & Binney, J. 2009, MNRAS, 396, 203
Searle, L. & Zinn, R. 1978, ApJ, 225, 357
Sesar, B., et al. 2009, ApJ, 708, 717
Sheffield A.A., et al., 2007, in IAU Symposium: A giant Step: from Milli- to Micro-arcsecond Astrometry, IAU Conf. Ser. 248, eds. W.J. Jin, I. Platais, & M.A. Perryman, (Cambridge: ASP), p. 506
Siebert, A., et al. 2008, MNRAS, 391, 793
Smith, M.C., et al. 2009, MNRAS, 399, 1223
Sommer-Larsen, J., & Zhen, C. 1990, MNRAS, 242, 10
Sommer-Larsen, J., Beers, T.C., Flynn, C., Wilhelm, R., & Christensen, P.-R. 1997, ApJ, 481, 775
Soubiran, C., Bienayme, O., & Siebert, A. 2003, A&A, 398, 141
Spagna, A. et al. 1996, A&A, 311, 758
Statler, T.S. 1988, ApJ, 331, 71
Tolstoy, E., Hill, V., & Tosi, M. 2009, ARAA, 47, 371
Twarog, B.A., & Anthony-Twarog, B.J. 1996, AJ, 111, 220
Velázquez, H. & White, S.D.M. 1999, MNRAS, 304, 254
Velleman, P., F. & Hoaglin, D.C., 1981, Application, Basics, and Computing of Exploratory Data Analysis (Boston: Duxbury Press)
Villalobos, A., & Hemli, A., 2008, MNRAS, 391, 1806
Vivas, A.K. & Zinn, R. 2006, AJ, 132, 714
Walker, I.R., Mihos, J.C., & Hernquist, L. 1996, ApJ, 460, 121
Wall, J.,V. & Jenkins, C., R., 2003, Practical Statistics for Astronomers (Cambridge: Cambridge Univ. Press)
Wilhelm, R. et al. 2005, in Cosmic Abundances as Records of Stellar Evolution and Nucleosynthesis, ASP Conf. Ser. 336, eds. T.G. Barnes & F.N. Bash, (San Francisco: ASP), p. 371
Xue, X.X. et al. 2008, ApJ, 684, 1143
Yanny, B., et al. 2003, ApJ, 588, 824
Yanny, B., et al. 2009, AJ, 137, 4377
Yoachim, P., & Dalcanton, J.J. 2008, ApJ, 682, 1004
York, D.G., et al., 2000, AJ, 120, 1579
Zhang, L., et al. 2009, ApJ, 706, 1095
Zinn, R. 1985, ApJ, 293, 424
Zinn, R. 1993, in The Globular Clusters - Galaxy Connection, ASP Conf. Ser. 48, eds. G.H. Smith, & J.P. Brodie, (San Francisco: ASP), 38
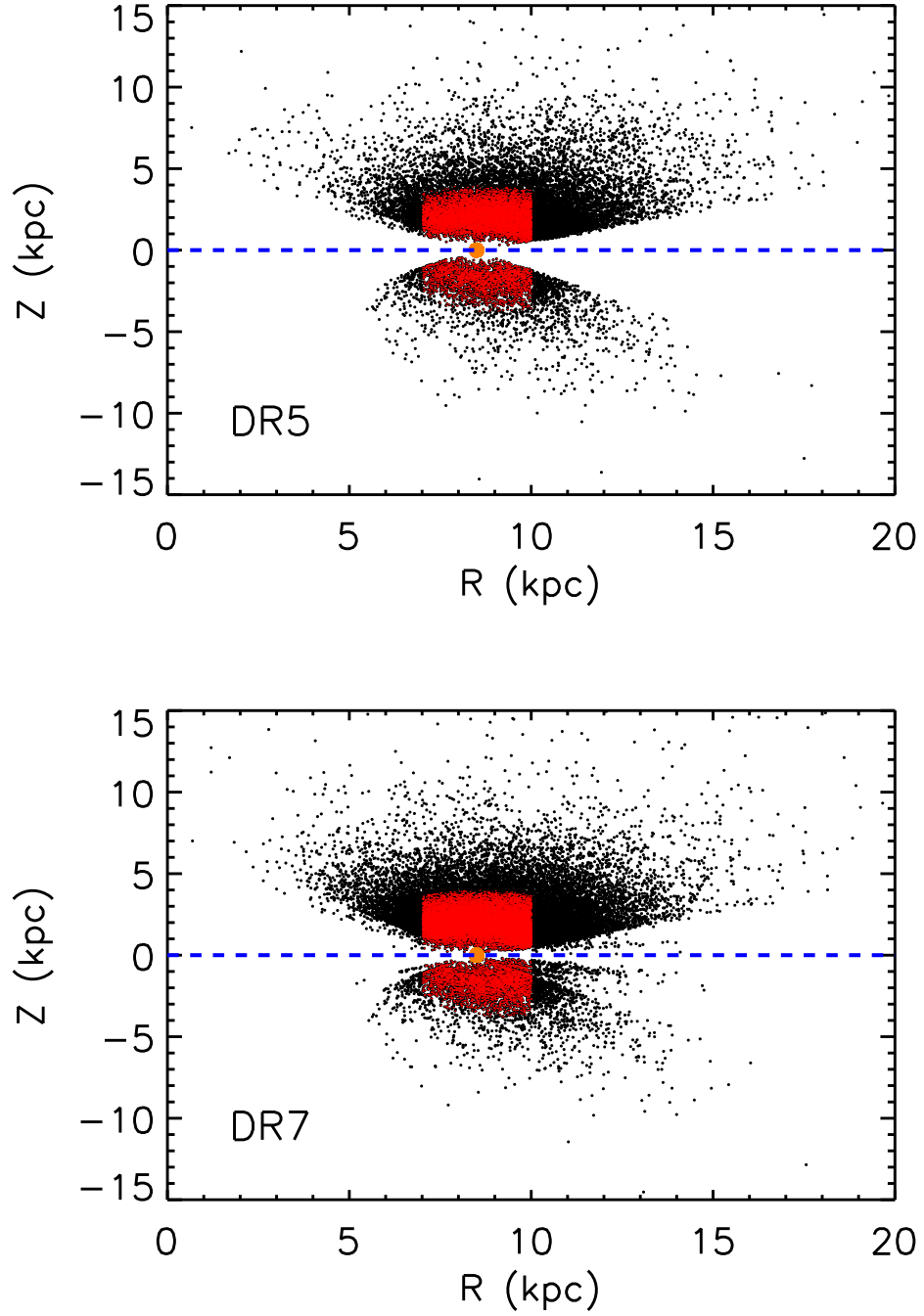Zolotov, A., et al. 2009, ApJ, 702, 1058

Fig. 1.— Spatial distribution in the Z-R plane of the 20236 SDSS DR5 (upper panel), and 32360 SDSS/SEGUE DR7 (lower panel) calibration stars. The black points represent the full sample, while the red points indicate the stars that satisfy our criteria for a local sample. The dashed blue line represents the Galactic plane, and the filled orange dot is the position of the Sun (at Z = 0 kpc; R = 8.5 kpc). In both panels, the wedge shape of the selection area is the result of the limits of the SDSS footprint in Galactic latitude. The overall increase in the numbers of calibration stars between DR5 and DR7 is clear, in particular for regions closer to the Galactic plane, due to the lower Galactic-latitude fields explored by SEGUE.
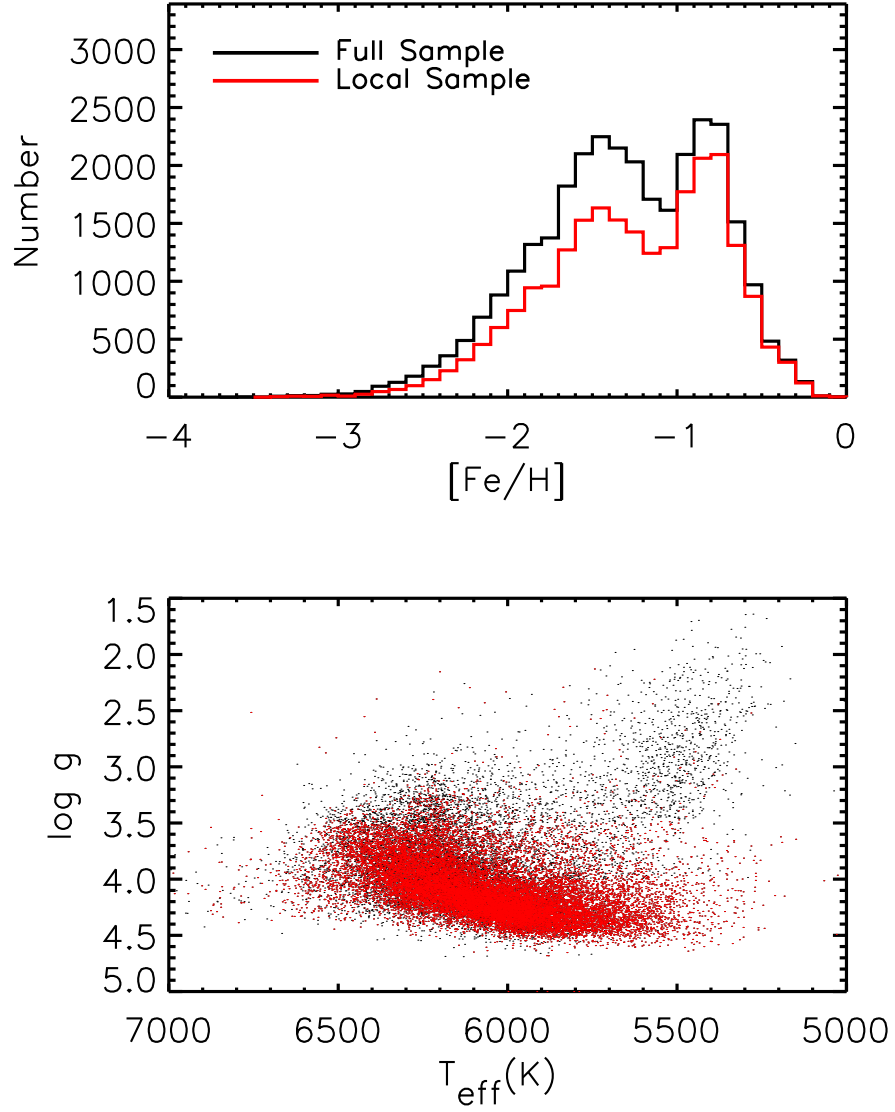
FIG. 2.— Upper panel: Metallicity Distribution Function (MDF), *as observed*, for the full sample of calibration stars (black histogram), and for the stars satisfying our criteria for the local sample (red histogram). Lower panel: Distribution of surface gravity, log g, versus effective temperature, T_{eff}, for the full sample (black dots) and local sample (red dots). Note that the full sample contains substantial numbers of main-sequence turnoff stars, subgiants, and giants, while the local sample primarily comprises main-sequence turnoff stars and dwarfs.
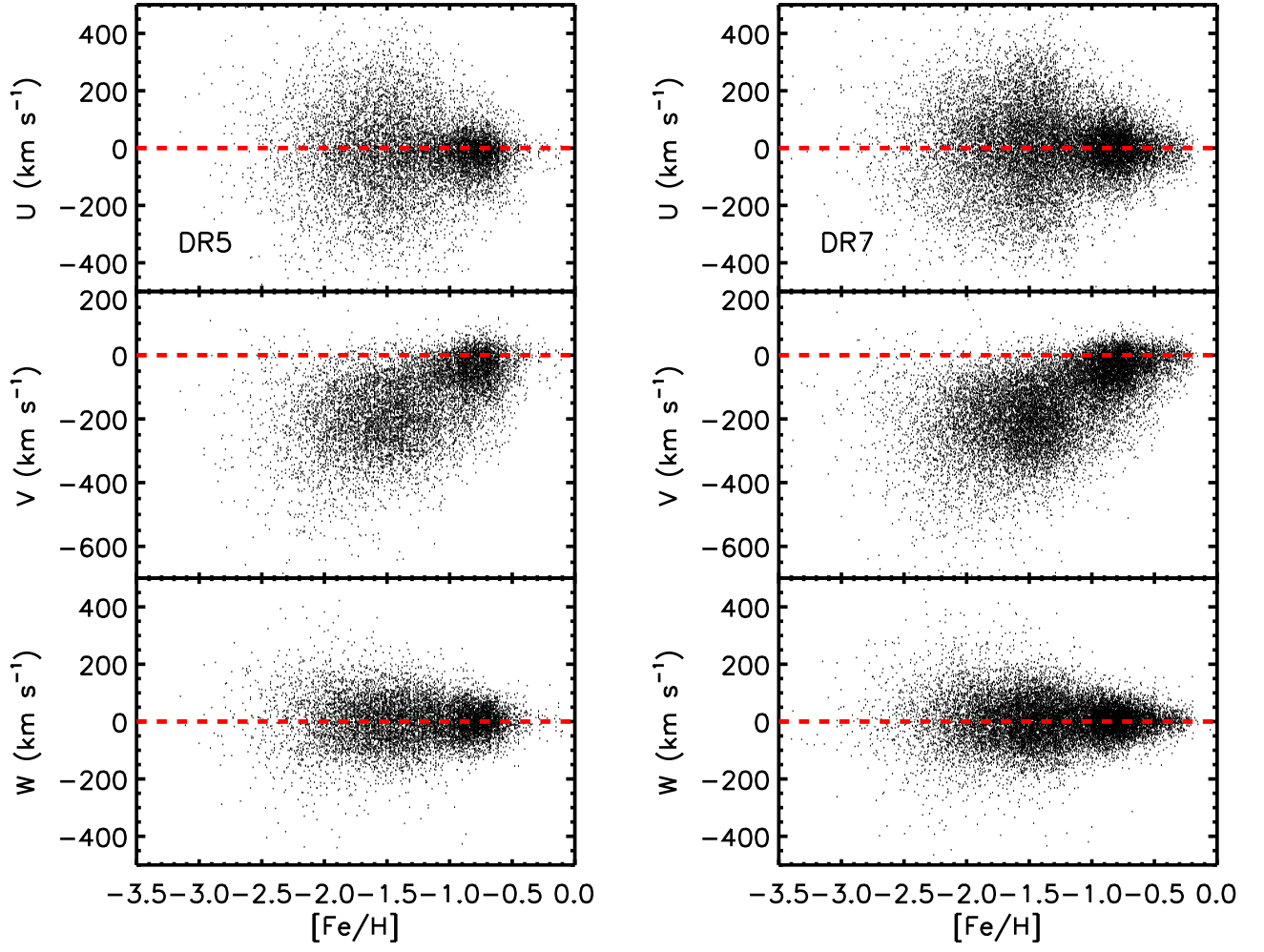
FIG. 3.— Distribution of the velocity components (U,V,W) versus [Fe/H] for the SDSS DR5 (left-hand panels) and the SDSS/SEGUE DR7 (right-hand panels) calibration stars. In both sets of panels only the local sample has been considered, comprising totals of 10120 and 16920 stars, respectively. The red dashed line is the adopted LSR for stars in the solar neighborhood. Note how the primary components of the stellar populations represented in the local volume, the thin disk, the thick disk, and the halo, are more clearly discerned in the DR7 sample. This is primarily due to refinements in the stellar parameter estimates obtained by the SSPP.
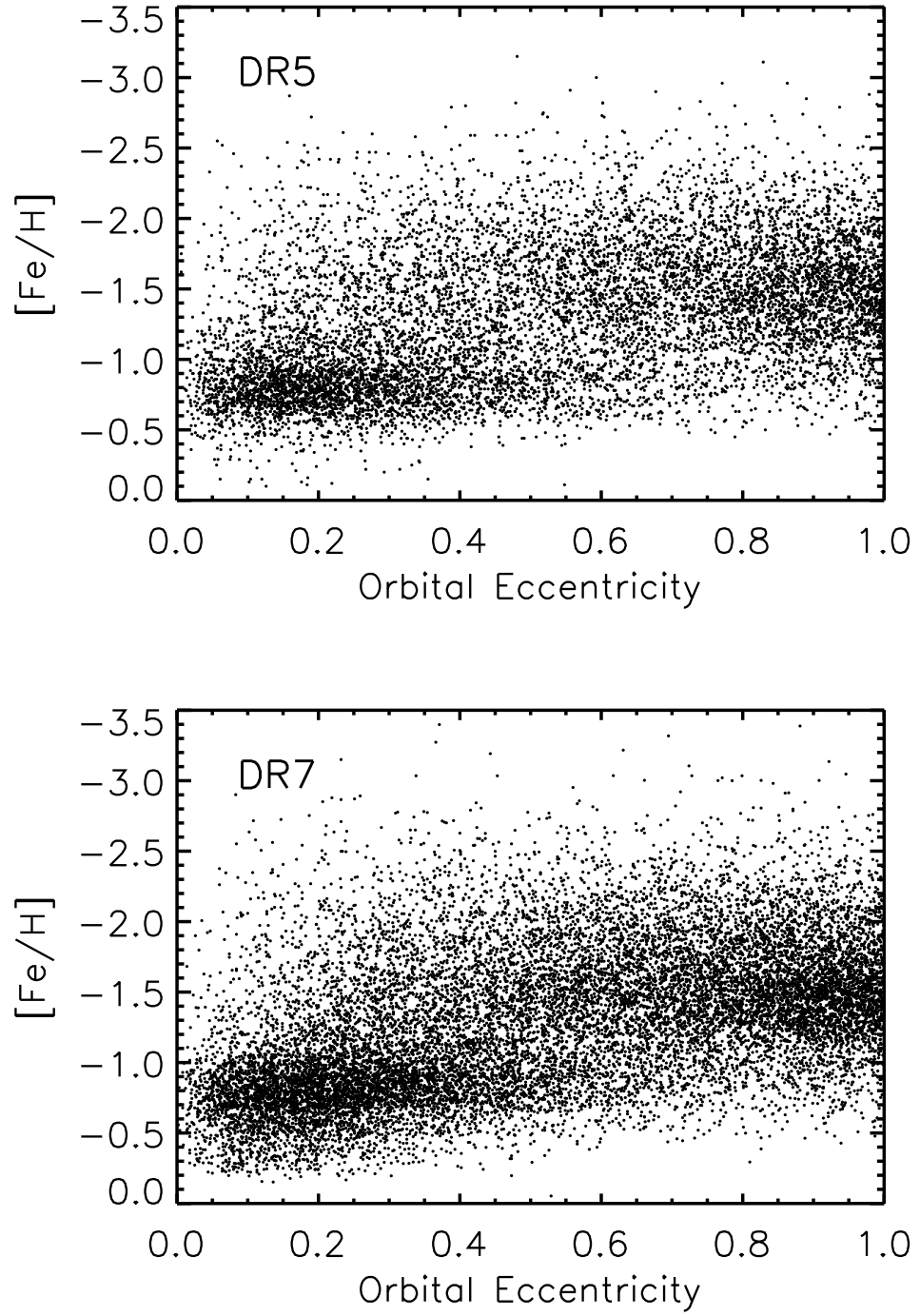
FIG. 4.— [Fe/H] versus orbital eccentricity for the SDSS DR5 (upper panel) and the SDSS/SEGUE DR7 (lower panel) calibration stars in the local volume. Note the far greater numbers of stars from DR7, as compared to DR5, in addition to the more densely populated disk-like regions for the DR7 data, due to the addition of the SEGUE fields.
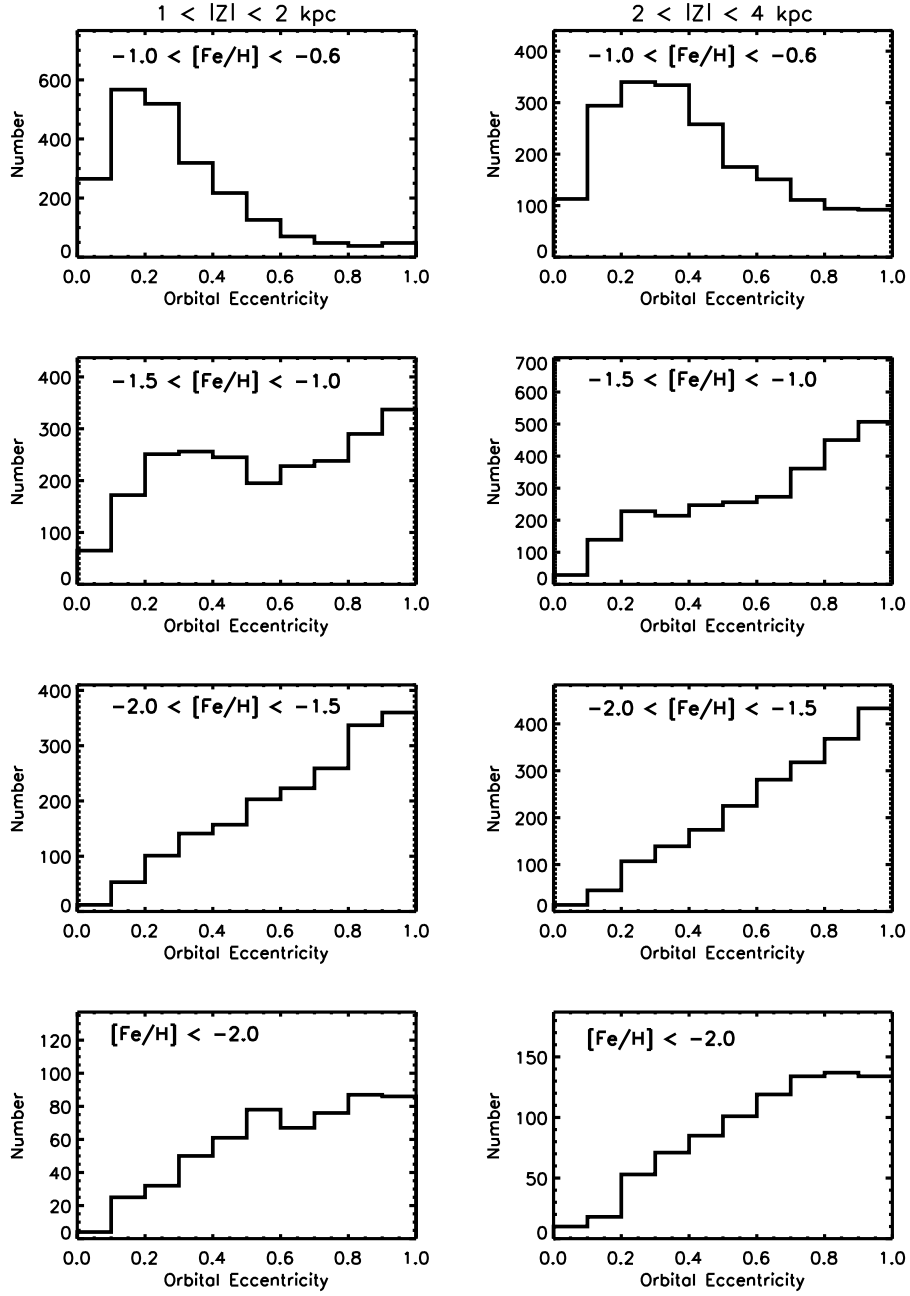
FIG. 5.— Distribution of the derived orbital eccentricity for sub-samples of stars selected in different metallicity ranges, for two different intervals on vertical distance |Z|, close to (1 < |Z| < 2 kpc; left-hand column of panels) the Galactic plane, and farther from (2 < |Z| < 4 kpc; right-hand column of panels) the Galactic plane.
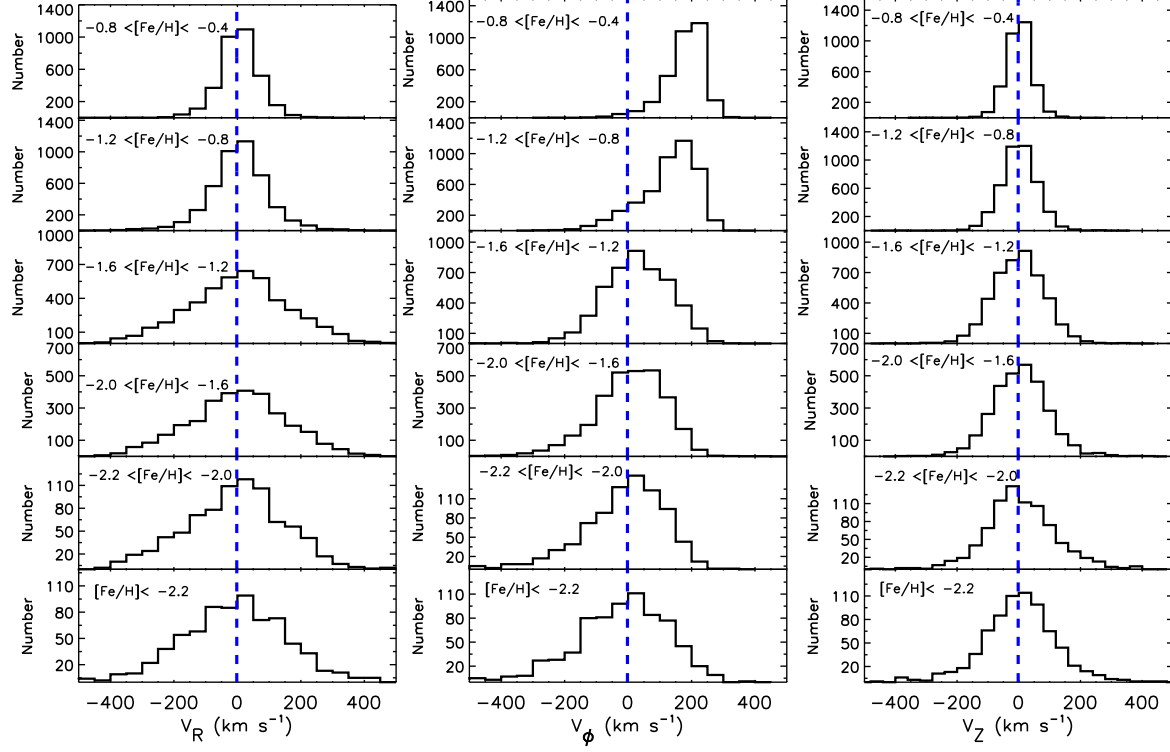
FIG. 6.— Distribution of the derived velocity components in a cylindrical Galactocentric frame, (V_R,V_ϕ,V_Z), for different ranges of [Fe/H]. The blue dashed line is a reference line at zero for each component.
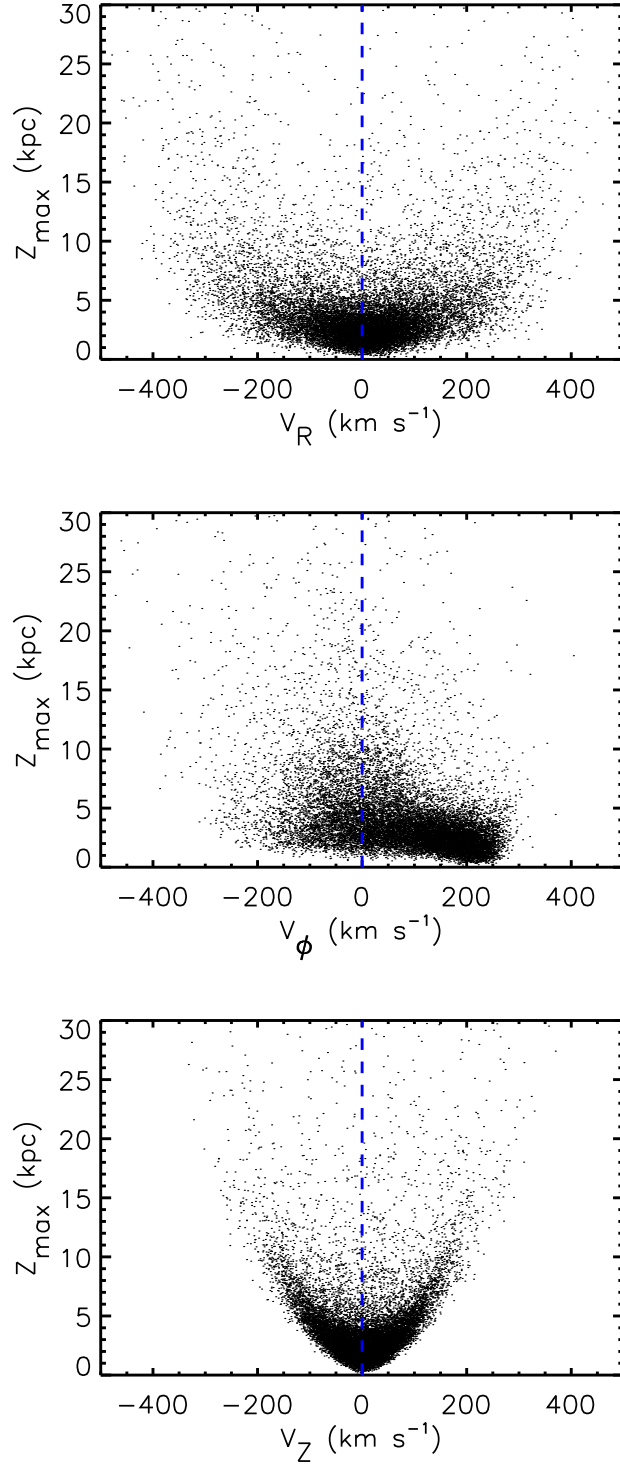
FIG. 7.— The relation between Z_{max} and the cylindrical velocity components (V_R,V_ϕ,V_Z) for the calibration stars in the local sample. Note the strong correlation between Z_{max} and the radial velocity component shown in the upper panel, V_R, as well as with the vertical velocity component shown in the lower panel, V_Z. The middle panel exhibits no strong correlation between Z_{max} and the rotational velocity component, V_ϕ, other than that expected from the presence of the thick-disk and halo populations. The blue dashed line is a reference line at zero for each component. Note, in the middle panel, the clear excess of stars with retrograde motions for $Z_{max} > 15$ kpc, which we associate with the outer-halo component.
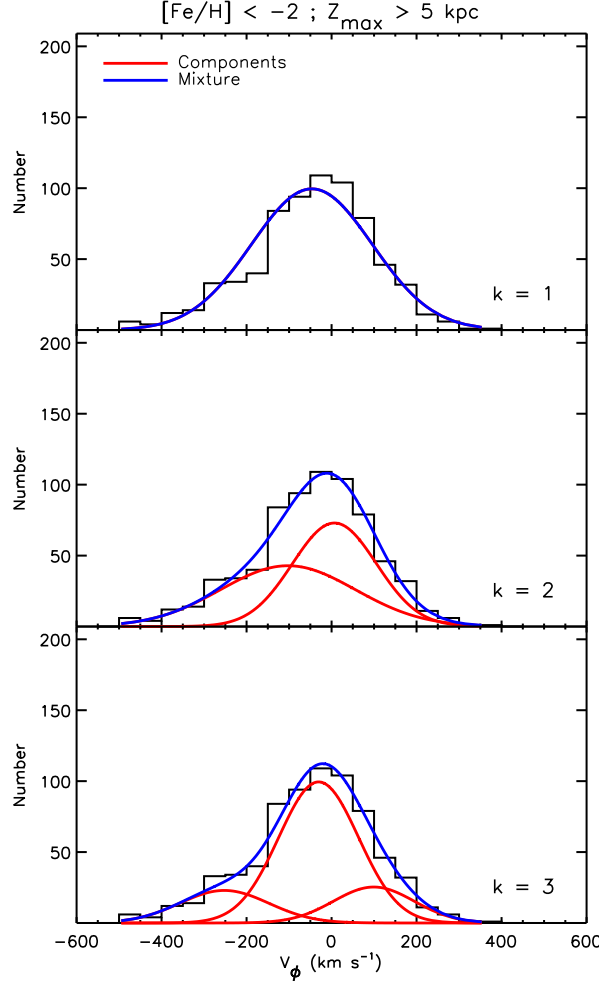
FIG. 8.— R-Mix results for the low-metallicity ([Fe/H] < −2.0) sub-sample of local calibration stars at large distances from the plane, Z_{max} > 5 kpc, using as input guesses the medoids and dispersions obtained with the clustering analysis (shown in Table 1). The top panel represents the fit for the case $k = 1$ (one component), while the second and third panels show the fit for two and three components, respectively. The blue lines in each panel denote the proposed mixture model for the distribution of observed rotational velocities, while the red lines are the individual Gaussian distributions included in the model. As discussed in the text, the one-component fit is strongly rejected, while both the two- and three-component fits provide adequate descriptions of the data.

Carollo et al.
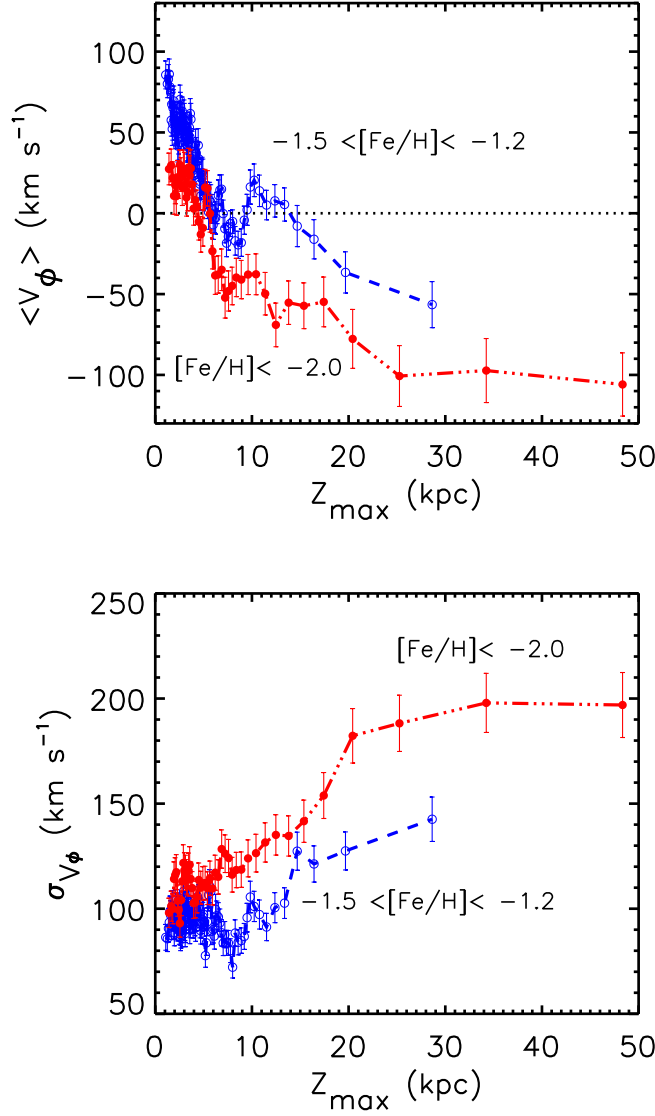
FIG. 9.— Mean Galactocentric rotational velocity (upper panel), and its dispersion (lower panel), as a function of Z_{max}, for intermediate-metallicity stars ($-1.5 <$ [Fe/H] < -1.2; blue curves) and low-metallicity stars ([Fe/H] < -2.0; red curves). The values of these quantities are obtained by passing a box of 100 stars, with an overlap of 70 stars per bin, through the data. The horizontal dotted line in the top panel indicates a zero (non-rotating) velocity. The values of the dispersion are not corrected for observational errors.
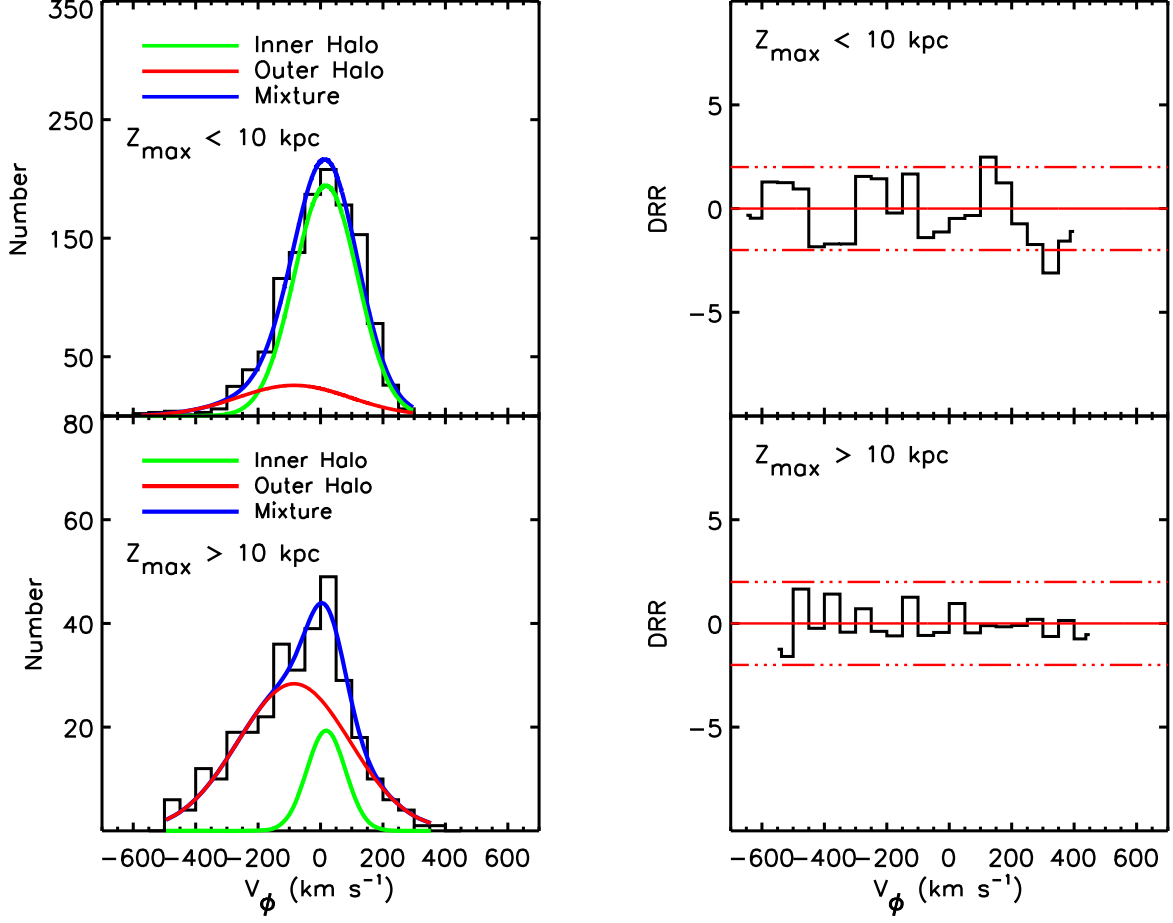
FIG. 10.— Rotational properties for the low-metallicity sub-sample ([Fe/H] < -2.0) of stars in the local calibration-star sample, divided into stars with Z_{max} above or below 10 kpc from the Galactic plane. The histograms in the left-hand panels illustrate the observed distribution of V_ϕ, while the green (inner halo), and the red (outer halo) curves represent the results of the ML analysis. The blue curves are the proposed mixture model for the distribution of the rotational velocities for this sub-sample. The right-hand panels are the Double Root Residual (DRRs) for these fits (see text for description). The dot-dashed lines at ± 2 indicate an approximate 95% significance level.
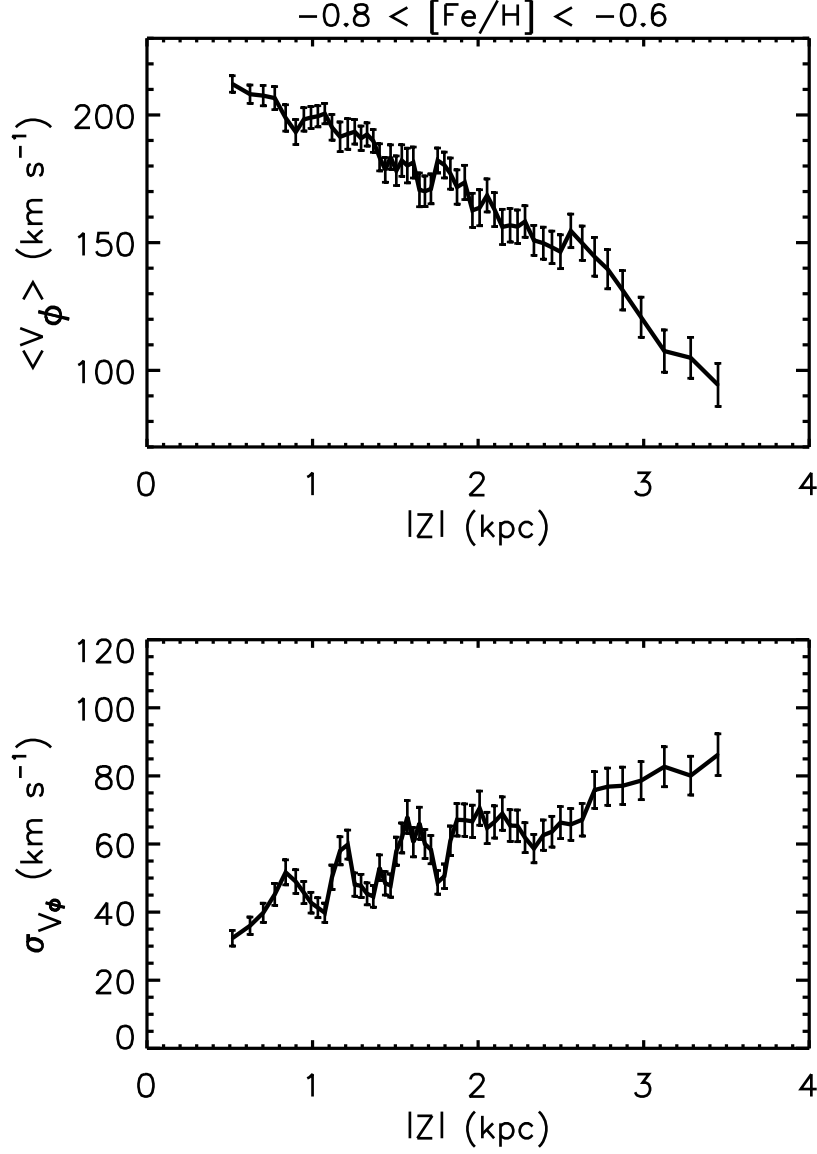
Fig. 11.— Mean rotational velocity (upper panel) and dispersion (lower panel), as a function of the vertical distance |Z|, for the high-metallicity sub-sample (−0.8 < [Fe/H] < −0.6) of stars in the local calibration-star sample. The values of these quantities are obtained by passing a box of 100 stars, with an overlap of 70 stars per bin, through the data. The values of the dispersions are not corrected for observational errors.
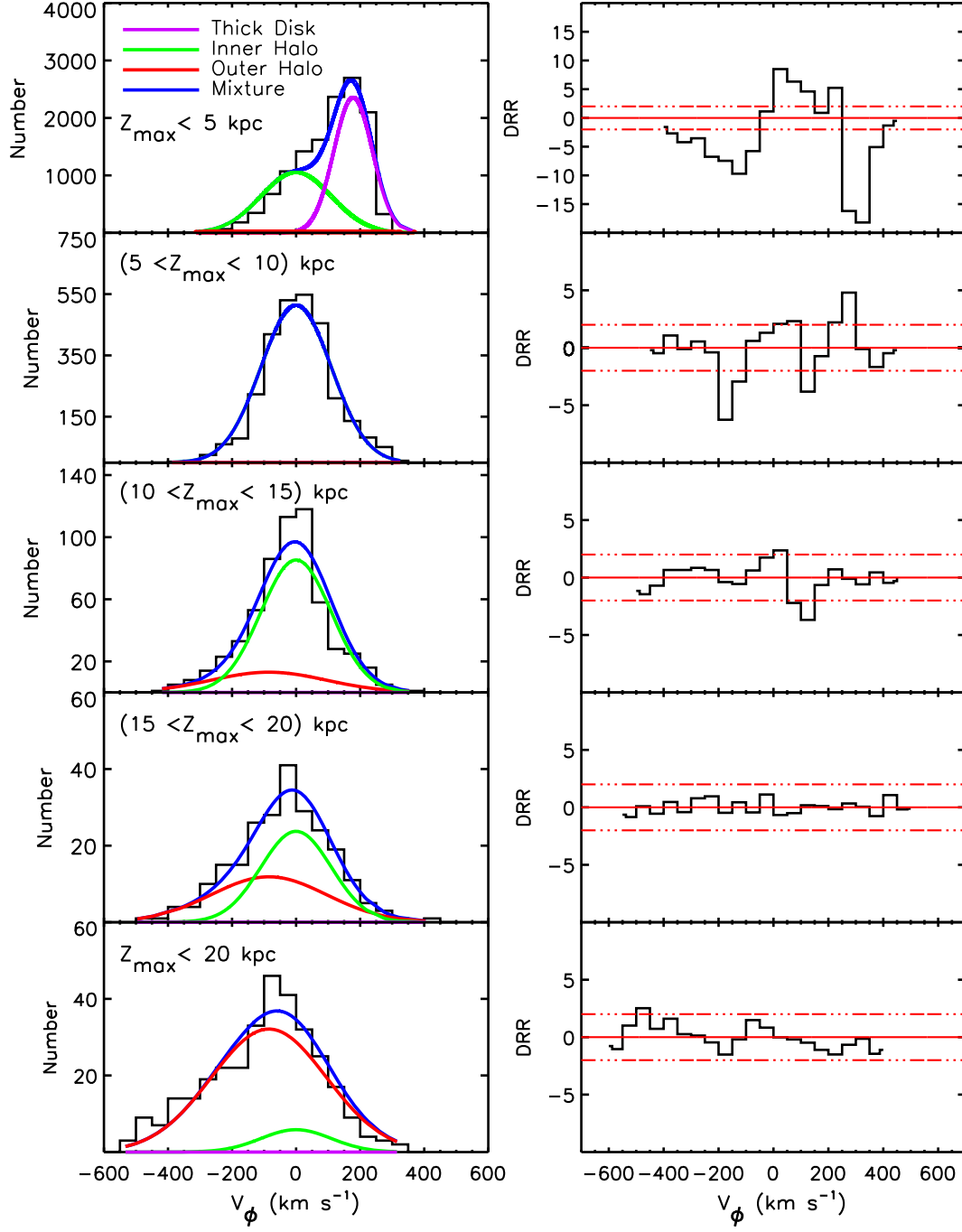
FIG. 12.— Rotational properties for the full metallicity range of stars in the local calibration-star sample. The histograms represent the observed distribution of V_ϕ, while the purple (thick disk), green (inner halo), and red (outer halo) curves represent the results of the ML analysis. The blue curves are the proposed mixture model for the distribution of the rotational velocities for this sample. Each panel corresponds to different cuts selected in intervals of Z_{max}, as indicated. The right-hand panels are the Double Root Residuals (DRRs) for these fits (see text for description). The dot-dashed lines at ± 2 indicate an approximate 95% significance level.

Carollo et al.
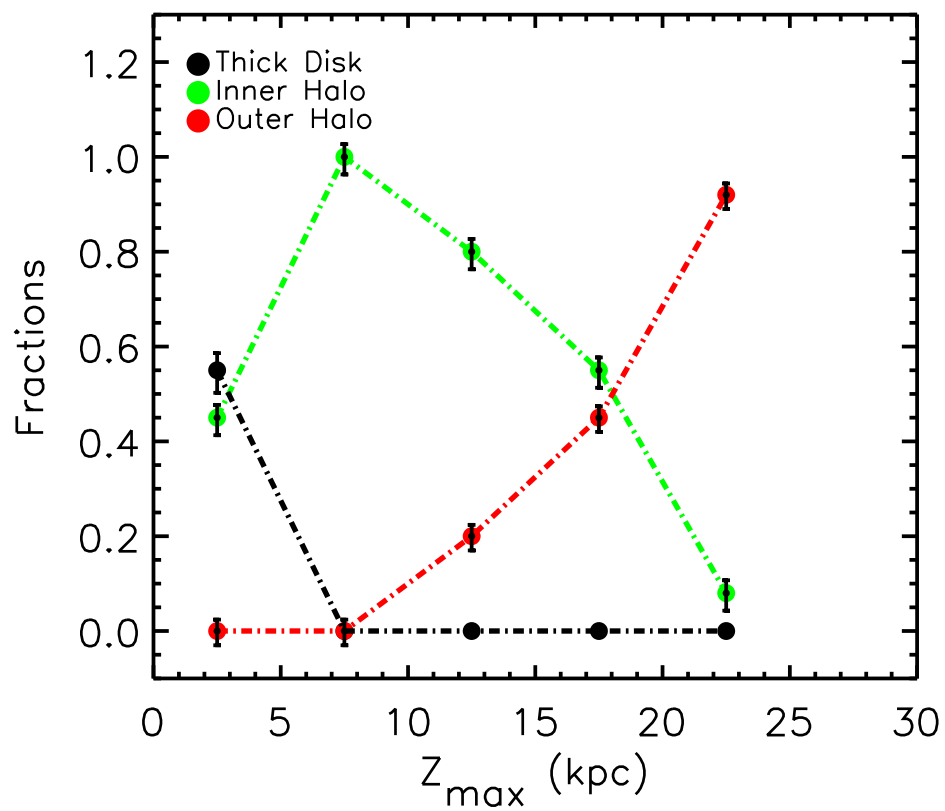
FIG. 13.— Derived stellar fractions, as a function of Z_{max}, for the thick disk (black dots), inner-halo (green dots), and outer-halo (red dots) components. These fractions are evaluated with the ML analysis applied to the full metallicity sample, with the input kinematic parameters for each component held fixed.
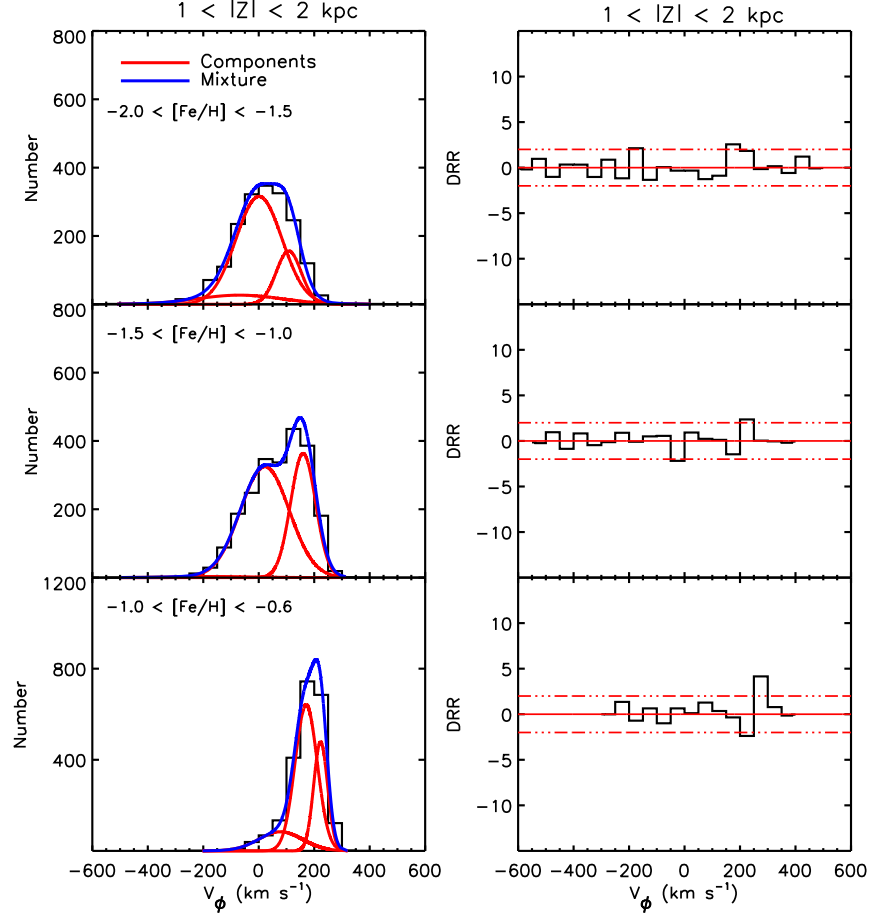
FIG. 14.— R-Mix results for three sub-samples of local calibration stars covering the range of metallicity $-2.0 <$ [Fe/H] < -1.5 (upper panel), $-1.5 <$ [Fe/H] < -1.0 (middle panel), and $-1.0 <$ [Fe/H] < -0.6 (lower panel), located close to the Galactic plane ($1 < |Z| < 2$ kpc). The input guesses are the medoids obtained with the CLARA clustering analysis. The histograms represent the observed distribution of V_ϕ, the blue lines in each panel denote the proposed mixture model for the distribution of observed rotational velocities, and the red lines are the individual Gaussian distributions included in the model. The right-hand panels are the Double Root Residuals (DRRs) for these fits (see text for description). The dot-dashed lines at ± 2 indicate an approximate 95% significance level. The apparent lack of fit for high velocity stars shown in the lower panel DRR plot is discussed in the text.
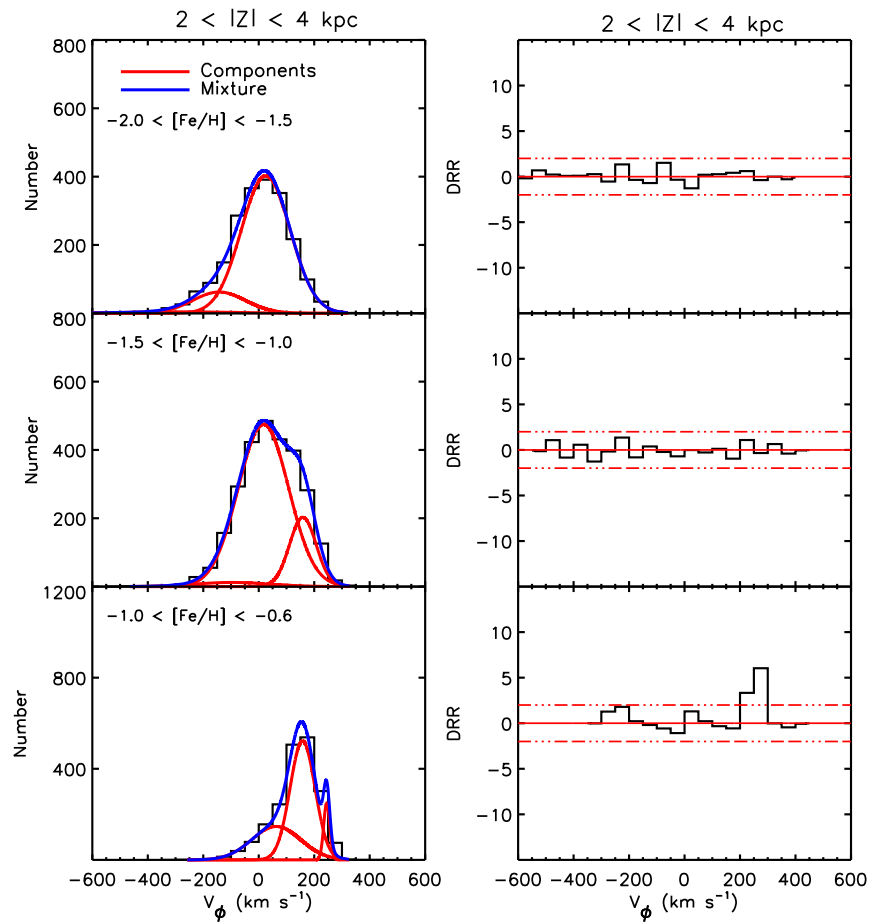
Carollo et al.

FIG. 15.— The same as Figure 14, but for stars located farther from the Galactic plane ($2 < |Z| < 4$ kpc). The apparent lack of fit for high velocity stars shown in the lower panel DRR plot is discussed in the text.
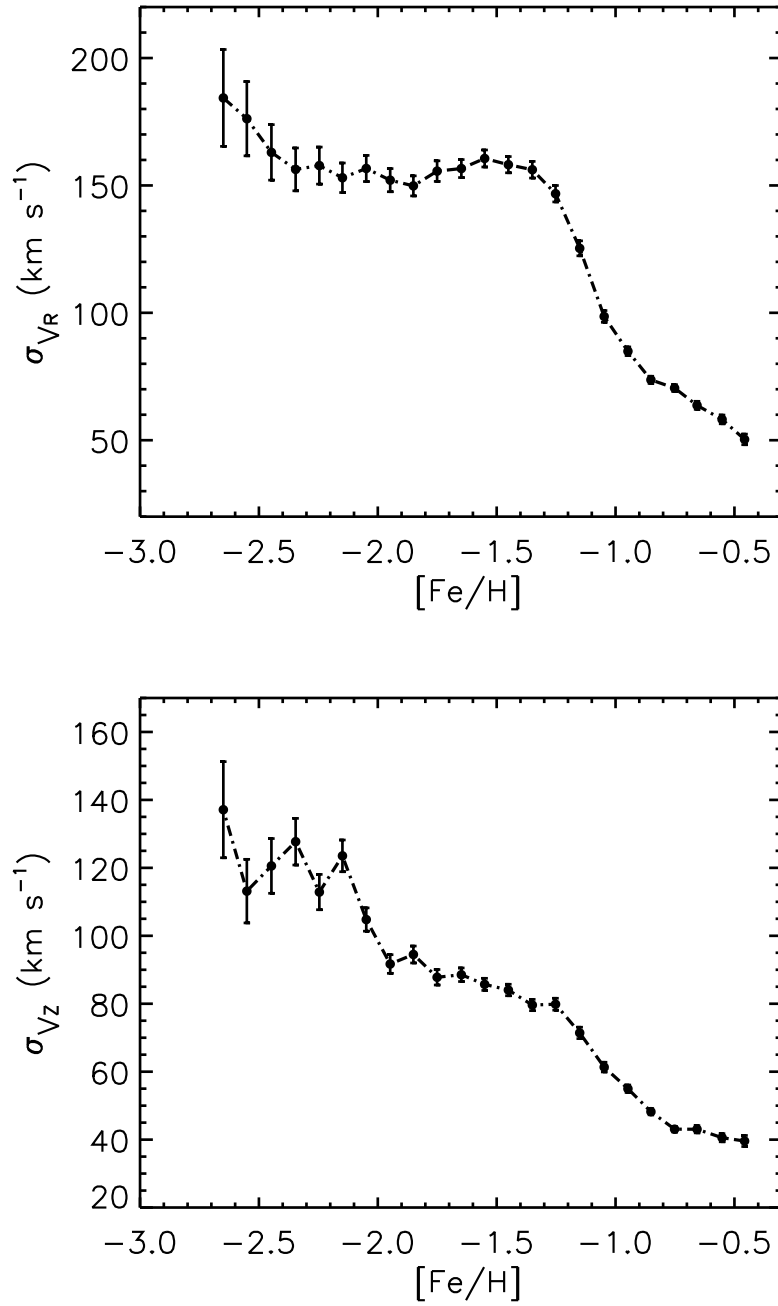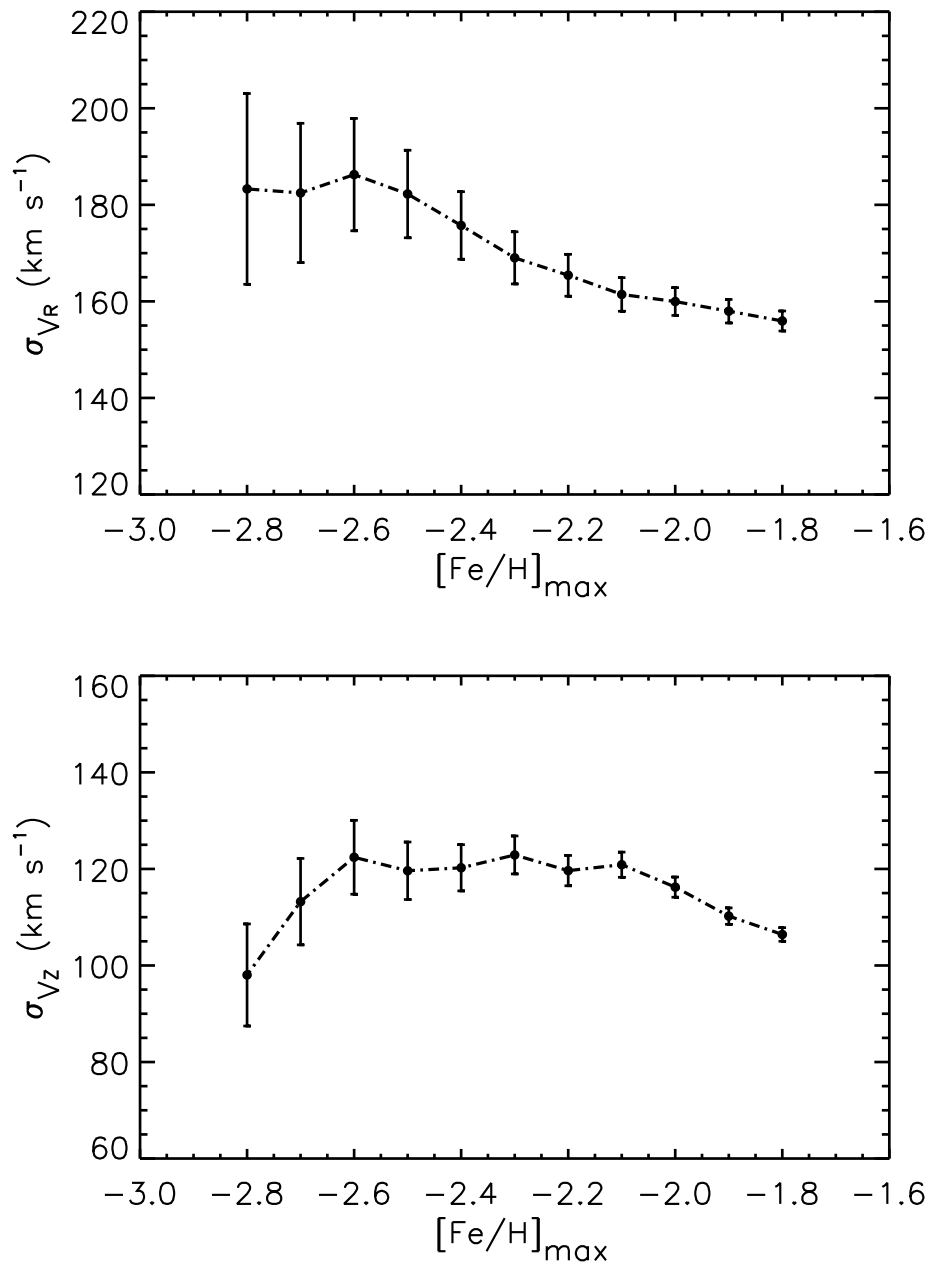
FIG. 16.— Velocity dispersions (corrected for observational errors) for the V_R (upper panel) and V_Z (lower panel) components, as a function of metallicity. The plot employs stars covering the full [Fe/H] of the local calibration-star sample. The bins represent a range of 0.1 dex in metallicity, and are non-overlapping.

Carollo et al.

FIG. 17.— Velocity dispersions (corrected for observational errors) for the V_R (upper panel) and V_Z (lower panel) components, as a function of metallicity, for metal-poor stars in the local sample. Each bin represents a sub-sample of stars with [Fe/H] < [Fe/H]$_{max}$.
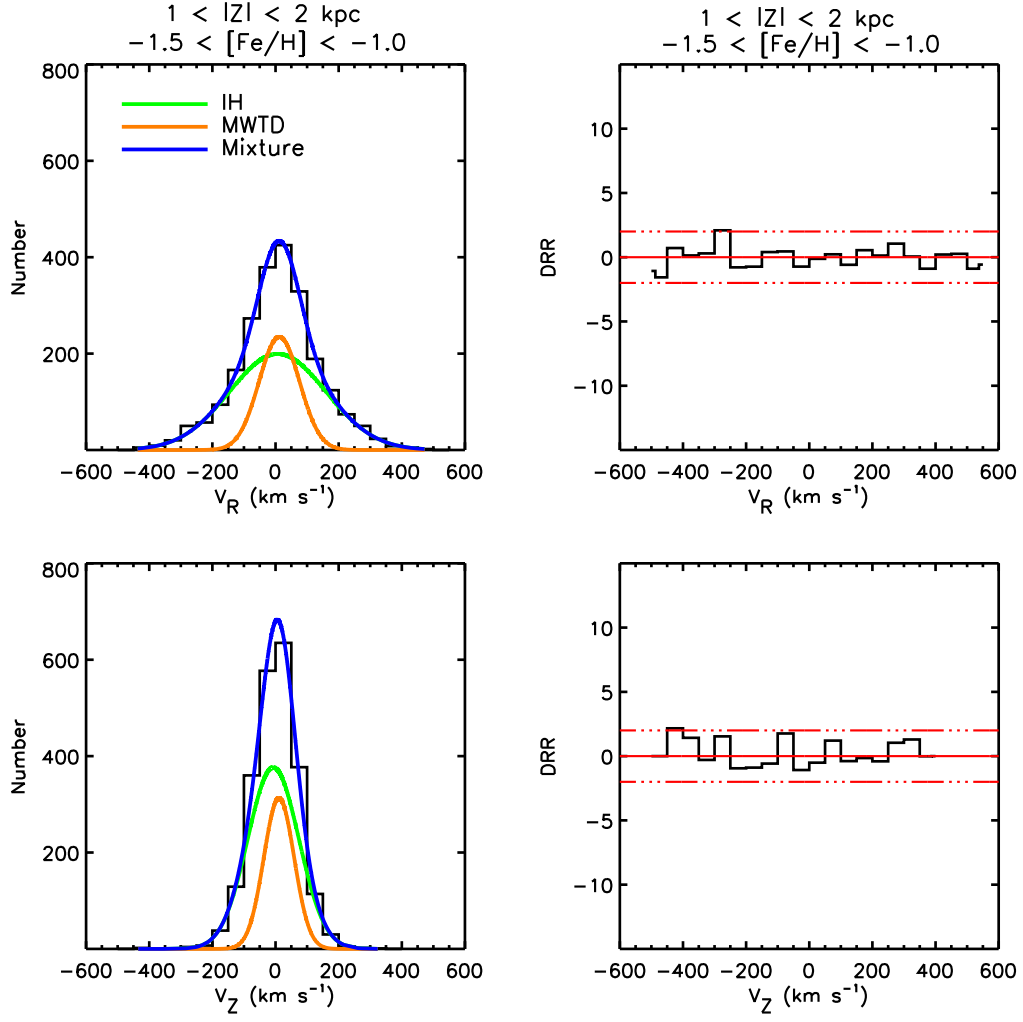
FIG. 18.— R-Mix results for the V_R (upper panel) and V_Z (lower panel) distributions. The selected range of metallicity is $-1.5 <$ [Fe/H] < -1.0, and the stars are located close to the Galactic plane ($1 < |Z| < 2$ kpc). The histograms represent the observed distribution of V_R and V_Z in each panel, respectively. The blue lines in each panel denote the proposed mixture model, while the orange and green lines are the individual Gaussians included in the model, representing the MWTD and the inner halo, respectively. The right-hand panels are the Double Root Residuals (DRRs) for these fits (see text for description). The dot-dashed lines at ± 2 indicate an approximate 95% significance level.
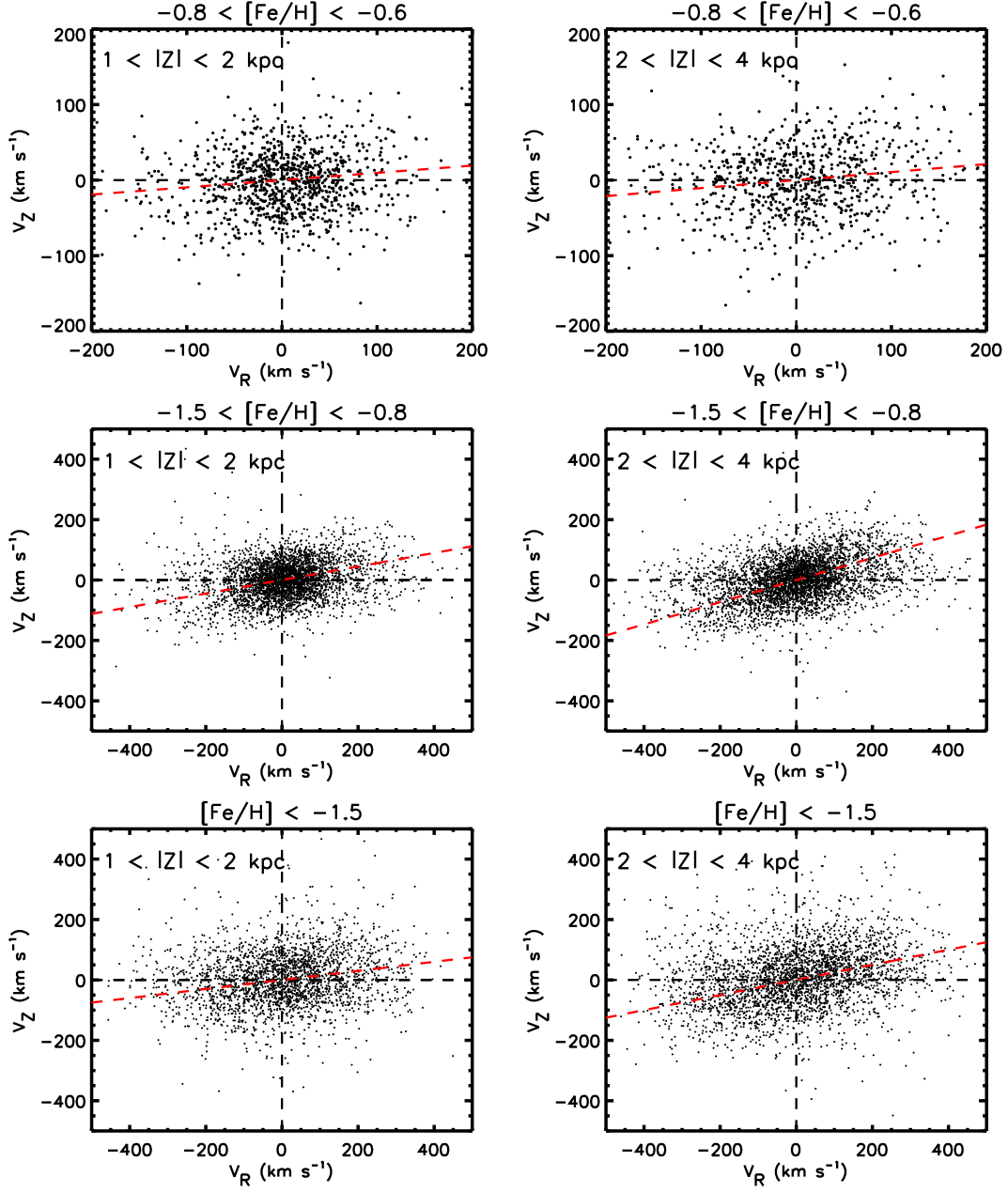
FIG. 19.— Observed tilt of the velocity ellipsoids in the (V$_R$,V$_Z$) plane for the metal-rich sub-sample with $-0.8 <$ [Fe/H] < -0.6 (top panels), the intermediate-metallicity sub-sample with $-1.5 <$ [Fe/H] < -0.8 (middle panels), and the low-metallicity sub-sample with [Fe/H] < -1.5 (lower panels). The left column shows these sub-samples close the Galactic plane, while the right column shows these sub-samples selected at higher |Z|. In each panel, the black dots are the distribution of the V$_R$ and V$_Z$ velocities , the black dashed lines indicates the principal axes of the (cylindrical coordinate) velocity ellipsoids in the meridional plane, and the red-dashed lines denote the derived inclinations of the ellipsoids.
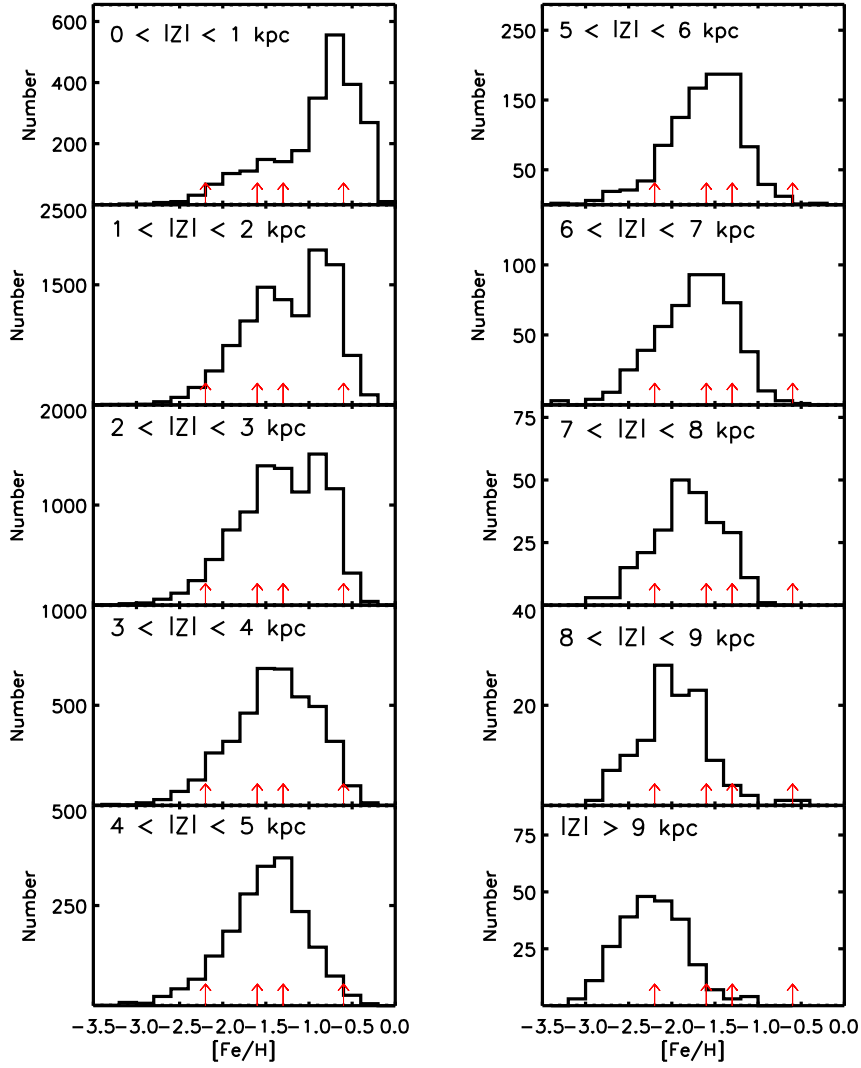
FIG. 20.— Observed metallicity distribution functions (MDFs) for the full sample of SDSS-SEGUE DR7 calibration stars as a function of vertical distance from the Galactic plane. The black histograms represent the MDFs obtained at different cuts of |Z|, while the red arrows denote the locations of the metallicity peaks of the MDF for the thick disk (−0.6), the MWTD ($\sim$ −1.3), the inner halo (−1.6), and the outer halo (−2.2), respectively.